Università
degli Studi
di Padova

A KEY TOOL TO PROBE EUCLID SPECTROSCOPY: SPECTRO-PHOTOMETRIC SIMULATIONS OF GALAXIES TO UNRAVEL NISP'S CAPABILITIES

By

LOUIS GABARRA

Supervisor: Giulia Rodighiero
Co-Supervisors: Chiara Mancini and Lucía Rodríguez-Muñoz

A thesis submitted in partial fulfillment of
the requirements for the degree of

MASTER DEGREE IN ASTRONOMY

UNIVERSITY OF PADUA
Department of Astronomy and Astrophysics
September, 2020

A KEY TOOL TO PROBE EUCLID SPECTROSCOPY: SPECTRO-PHOTOMETRIC SIMULATIONS OF GALAXIES TO UNRAVEL NISP'S CAPABILITIES

by Louis Gabarra

Supervisor: Giulia Rodighiero
Co-Supervisors: Chiara Mancini and Lucía Rodríguez-Muñoz

Abstract

We present in this master Thesis the construction of Spectral Energy Distribution (SED) of galaxies located at $0.3 \leq z \leq 2.5$. The constructed SEDs (also referred throughout the Thesis as "incident SED", or "incident spectra") will go through the Euclid Near Infrared Spectrometer and Photometer (NISP) simulator hosted in the Istituto di Astrofisica Spaziale e Fisica Cosmica (IASF; INAF) at Milan, aiming at reproducing spectra expected from the NISP mounted on the Euclid telescope. These simulations will enable evaluating the spectroscopic survey performances of the Euclid mission, and confirming that the telescope and its slitless NISP spectrometer will satisfy the required detection limits for nebular emission lines.

This project was conceived in synergy with the Euclid Legacy Science Working Groups (SWGs), as a "PILOT RUN" simulation test for spectroscopic data. The PILOT RUN includes a study of the capabilities expected from the Euclid Wide and Deep fields' configurations. The spectral libraries are created to offer a realistic and complete sample of representative galaxies in the range of redshifts and total stellar masses expected to be covered by the Euclid Mission. We create two spectral libraries, one for each of the Wide and Deep surveys, using publicly released multi-wavelength photometric and spectroscopic data.

For the Wide field survey we refer to the COSMOS2015 catalog (Laigle et al., 2016) covering the Cosmological Evolution Survey (COSMOS) field, while for the Deep field survey we refer to the BARRO2019 catalog (Barro et al., 2019) that covers the CANDELS Great Observatories Origins Deep Survey North (CANDELS/GOODS-N) field.

The construction of the incident SEDs consists in computing a continuum using the Bruzual & Charlot(2003) models, calling out best-fit SED parameters available in the catalogs. The nebular emission Balmer, [NII]$\lambda\lambda$6584,6549, [OII]$\lambda\lambda$3727,3729, [OIII]$\lambda\lambda$5007,4959, [SII]$\lambda\lambda$6731,6717, [SIII]$\lambda\lambda$9531,9069 and Paschen lines are added making use of calibrations available in literature. We refer to common tools and indicators for emission lines analysis such as the Star Formation Rate (SFR), the Baldwin-Phillips-Terlevich diagram (BTP), the Mass-Metallicity Relation (MZR) and photoionization models. The emission lines are then integrated to the continuum accounting for the calculated velocity dispersion of each galaxy. A photometric and spectroscopic comparison of the incident SEDs with observational data is presented in this Thesis. The incident SEDs then go through the Euclid NISP simulator that mimic the spectra expected from the NISP spectrometer, generating the simulated spectra.

The PILOT RUN simulations are still ongoing, only part of the simulated spectra have been constructed, limited to the galaxies from the CANDELS/GOODS-N catalog, corresponding to one out of the 5 pointings planned to reach the required Deep Survey configuration, in terms of exposure time. This pointing exactly matches the exposure time required for the Wide Survey configuration. Thus, we present in this Thesis a first analysis of the available simulated data, and provide a confirmation of the detection limit specifications for the continuum (i.e. H(AB) $\geq$ 19.5 mag) and emission lines (i.e. Flux $\geq 2 \times 10^{-16}$ erg cm^{-2} s^{-1} Å^{-1}) of the Euclid Wide Survey. The full set of the PILOT RUN simulations will extensively complete the first picture given by our preliminary analysis.

We also provide an estimate of the NISP spectral resolution and finally present an analysis stacking spectra located at $1.6 \leq z \leq 2.0$, attesting for the great potential of the method in confirming redshift determination, a crucial aspect for the Euclid mission.

ACKNOWLEDGMENT

I am particularly thankful to the Professor Alberto Franceschini who have raised my interest in cosmology and also for his trust when giving me the opportunity to do my master Thesis in his research group on such a fascinating project. I want to thank Giulia Rodighiero and Paolo Cassata for welcoming me warmly within the team and for giving me great advices to get up to speed with the spectroscopic analysis. I will be grateful for a lifetime to the team I had the honor to closely work with the past months. Starting from my supervisor Giulia Rodighiero for her amazing knowledge and leadership and for setting the best working environment. My greatest thanks also go to my co-supervisors Chiara Mancini and Lucía Rodríguez-Muñoz for their positive energy, for teaching me everything (and more) required to work efficiently on the Thesis and also for making this master Thesis manuscript as it looks today. I would also like to thank my wife for encouraging me even if my mind was sometimes over focused on working, even during the nights at the maternity! I hope that my new born *astro* doesn't doubt he is still the one illuminating my path. I am very grateful to the French international school of Addis Abeba and the Observatory of Paris for giving me the opportunity to step up in astronomy in optimal conditions when I was leading the school's club of astronomy. I also want to thank Abel Abebe, my dear friend, with whom I spent nights observing the beautiful and inspiring Ethiopian sky, seeding the will to deepen my knowledge in the field. Thanks to my parents for supporting me along my professional choices that are not always easy to understand. I would like to thank the Professor Enrico Corsini for giving me the possibility to enroll in the Master degree in Astronomy. This thesis has been made with the great support of the Euclid Consortium, in particular of the Legacy Science Working Group led by Margherita Talia who have made possible to integrate this work within the Euclid's research, and finally a special thanks to Marco Scodeggio and Luca Paganini for generating the NISP simulations and for the quality of our exchanges.

Contents

Page

APPENDIX

Chapter One

Introduction

In this master Thesis, we will go through the process of construction and analysis of simulated spectra for the Euclid mission. The Euclid mission will bring crucial contributions to astrophysics, being designed to be at the edge of this new era in which large surveys will take over, scanning the entire sky at different redshift range. Euclid will generate a huge amount of data from which we can expect key discoveries related to the Dark Universe and the evolution of galaxies. Euclid will probe the Universe since redshift ≈ 2 down to present time, therefore covering the period known as the cosmic noon (Madau, Pozzetti, and Dickinson, 1998; Madau and Dickinson, 2014) where galaxies have been particularly prolific in terms of star formation rate that has been declining ever since. Studying this range will therefore provide fundamental discoveries about the evolution of galaxies.

The Euclid consortium is actively working on preparing and optimizing the observation scheme of the project as well as the pipeline for the data reduction and analysis. In such a context, this study aims at providing a library of simulated spectra and provide an estimation of the slitless spectroscopic detection limit expected from the Euclid telescope and its NISP spectrometer.

The spectroscopic survey from the Euclid mission will be of crucial importance to understand the evolution of galaxies. Indeed, emission lines are widely correlated to physical properties of galaxies. For example, their measurement can provide information on the Star

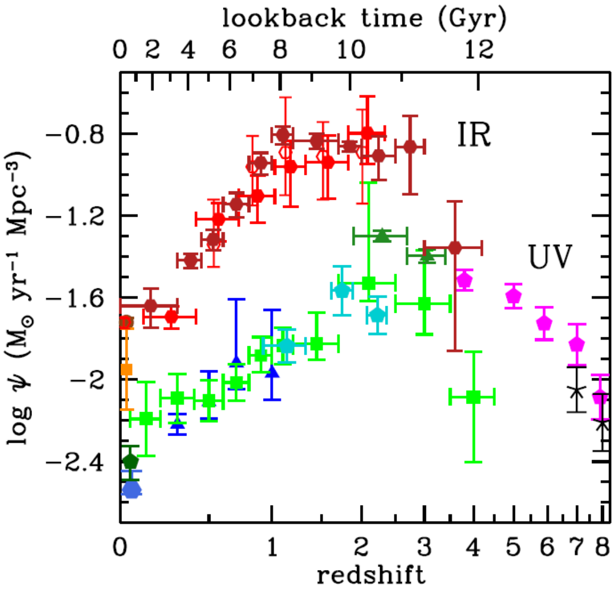

Figure 1.1 Plot illustrating the concept of the cosmic noon. SFR densities in the FUV (uncorrected for dust attenuation) and in the FIR [extracted from Madau and Dickinson, 2014]. We can that the SFR is clearly increasing from present days up to redshift ≈ 2. The situation at higher redshift still requires further studies.

Formation Rate (SFR) within the hosting galaxy and also be a great tracer to track the presence of an Active Galactic Nuclei (AGN).

The study of the NISP capabilities presented in this Thesis will be performed by creating and analyzing simulated spectra that mimic those expected from the NISP spectrometer (NISP-S). The methodology to create the simulated spectra is made of two phases. The first consists in the construction of a library of realistic Spectral Energy Distributions of galaxies[1] The incident spectra have been constructed to be representative of the galaxy populations that will be observed by the instrument. Second, these incident spectra are processed by a pipeline that will reproduce the expected output from observation by the NISP-S. This Thesis was conceived in synergy with the Euclid Legacy Science Working Groups (SWGs), as a PILOT RUN simulation test, in preparation of the so-called "FULL RUN" simulation for spectroscopic data. This will be of crucial importance to evaluate the expected spectroscopic survey performances of the Euclid mission, confirming that the telescope, and its slitless NISP-S spectrometer, match the required detection limits, for both the Wide and Deep

---

[1] Hereafter referred as the incident spectra. These incident spectra are built to go through the Euclid NISP-S simulator.

fields' configurations[2].

The PILOT RUN is therefore designed to provide one library of incident spectra to test the Wide field configuration and another one, presenting relatively fainter galaxies, to test the Deep field configuration.

The creation of the incident spectra includes the construction of the continuum and the calculation of the nebular emission lines (chapter 4) starting from two publicly released multi-wavelength photometric catalogs with sources available in our redshift range of interest. These catalogs are the COSMOS2015 (Laigle et al., 2016), covering the COSMOS field and the BARRRO2019 (Barro et al., 2019) covering the CANDELS/GOODS-N field and will be introduced in chapter 3. The COSMOS2015 catalog includes sources covering a wide range of luminosities and stellar masses, thus making it ideal to simulate the Wide field configuration. The BARRO2019 catalog, covering a smaller field, is used to simulate the Deep field configuration.

The stellar continuum is generated with SED-fitting parameters retrieved from the catalogs of real galaxies and using the Software GALAXEV (Bruzual and Charlot, 2003). The emission lines fluxes are calculated using recipes available in literature, and also referring to SED-fitting parameters from the catalogs.

The incident spectra will go through the NISP-S simulator. The simulation of all the incident spectra is still on-going. In this work, we present a first analysis of simulated spectra in the Wide field configuration. We perform in chapter 6 a finding and fitting procedure for the nebular emission lines Hα, Hβ, [NII]$\lambda\lambda$6584,6549, [OIII]$\lambda\lambda 4959, 5008$, and [OII]$\lambda\lambda$3727,3729. We retrieve from the Gaussian fit of the lines crucial information such as the total flux, the Full Width Half Maximun (FWHM) and Signal to Noise Ratio (SNR) that eventually enable us to provide a first confirmation of the detection spectroscopic capabilities

---

[2] The Wide field configuration consists in one exposure of 4 frames and the Deep field configuration consists in 5 exposures of 4 frames each. Each frame has an exposure time of 553.0 sec. The FoV covered by one exposure is ≈ 0.5 deg^2.

and spectral resolution of the NISP-S in the Wide field configuration.

When lines are too faint to be detected on individual spectrum, we will perform a stacking analysis to explore the potential of the approach in confirming redshift determination.

Chapter Two

The Euclid Mission

In this chapter we present the Euclid mission, starting with an overview in section 2.1 to describe the scientific context of the mission. The section 2.2 will go through the Euclid survey, describing the scientific contribution expected and the probes for which the mission has been designed for. We will make a special mention of the slitless spectroscopy survey that this Thesis is simulating. Finally, in section 2.3, we present the Payload Module and in particular the NISP, from which this thesis aims at preparing the detection capabilities preliminary study.

2.1 Overview

Euclid is part of the European Spatial Agency's (ESA) "Cosmic Vision" (2015–2025) scientific program and is referred as a medium-class ("M-class") mission. The launch date is predicted for the summer 2022 from the Europe's Spaceport in Kourou, French Guyana.

Euclid top priority objective is to map the geometry of the Universe to improve our understanding of the mysterious dark matter and dark energy. The mission is being designed to cover 15,000 deg^2, corresponding to 35% of the celestial sphere, up to redshift ≈ 2. The mission is organized around two primary cosmological probes, the Weak Lensing (WL) and Galaxy Clustering (GC).

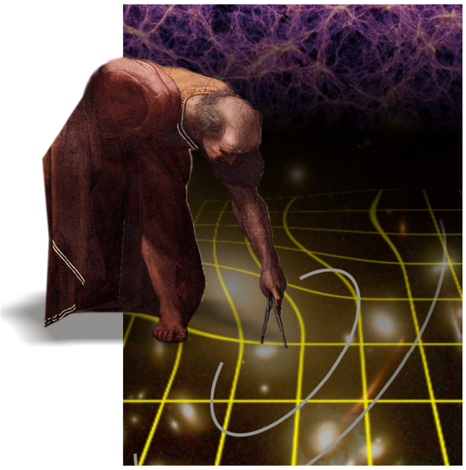

Figure 2.1 Composite of a fragment from Raphael's fresco "The School of Athens" in the Stanza della Segnatura of the Vatican Palace depicting the Greek mathematician Euclid of Alexandria, a simulation of the cosmic web by Springel et al, and an image of Abell 1689; the composition is made by Remy van Haarlem (ESA/ESTEC) [extracted from Laureijs et al., 2009].

One result among the others will be a 3-dimensional analog and complement to the map of the high-redshift Universe provided by the Cosmic Microwave Background (CMB) experiments. The denomination EUCLID, acronym for EUropean Cosmic aLl sky Investigator of the Dark Universe, has therefore been chosen in honor of the iconic Greek mathematician Euclid of Alexandria, known as the father of geometry.

The Euclid project was born in 2007 from the merging of two different projects, the Dark Universe Explorer (DUNE) mission intended to measure the effects of weak gravitational lensing and the Spectroscopic All Sky Cosmic Explorer (SPACE), aimed at measuring the Baryonic Acoustic Oscillations (BAO) and redshift-space distortion patterns in the Universe.

Combining these missions with its wide-field capability and high-precision design, Euclid will:

1. Investigate the properties of the dark energy by accurately measuring the acceleration as well as the variation of the acceleration at different ages of the Universe

2. Test the validity of general relativity on cosmological scales

3. Investigate the nature and properties of dark matter by mapping the 3-dimensional dark matter distribution in the Universe

4. Refine the initial conditions at the beginning of our Universe, which seed the formation

of the cosmic structures we see today.

The mission therefore requires to probe cosmic epochs when dark energy started to accelerate the expansion of the universe, corresponding to a redshift z $\approx$ 2 or equivalently to a look-back time of 10 billion years, all the way to the present. To complete its mission, Euclid and its 1.2m Korsch Telescope will be outfitted with a Visual Imager (VIS) for photometry in the optical (5,500Å to 9,000Å) and a Near Infrared Spectrometer and photometer (NISP) detector. The NISP is made of a photometric (NISP-P) channel that will cover the Near-Infrared (NIR) wavelength range from 9,000Å to 20,000Å and a spectroscopic channel (NISP-S) covering from 9,200Å to 18,770Å. At redshift 0.5 $\leq$ z $\leq$ 2, the strong optical emission lines are shifted to the Near-Infrared, Euclid spectroscopic survey has therefore been designed to be able to extensively cover this range, including the so-called *redshift desert* (fig.3 in Le Fèvre et al., 2015). This denomination refers to the redshift range $1.4 \leq z \leq 1.8$, where all strong spectral features in the optical at rest-frame, such as the Hα, [OIII]$\lambda\lambda$5007,4959, Hβ and [OII]$\lambda\lambda$3727,3729 lines are redshifted in the infrared, while the Lyman break remains too blue to enter into the range of traditional optical spectrographs. Euclid will therefore enable an unprecedented imaging and NIR survey, providing the community with a tremendous database with photometry for billions of galaxies and spectroscopy for more than 35 million galaxies.

2.2 The Euclid survey

2.2.1 The Euclid science

Over the last decades, a combination of observations has led to the emergence and confirmation of the concordance cosmological model. This includes the cosmological principles and the so-called ΛCDM model, where CDM stands for Cold Dark Matter and Λ is a cosmological constant associated to the Dark Energy.

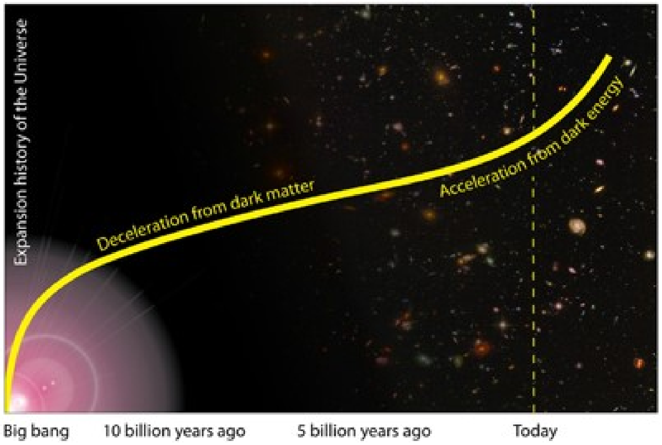

Figure 2.2 The Universe evolved from a homogeneous state after the Big Bang through cooling and expansion. The small initial quantum fluctuation have been brought to cosmological scales during the inflation and grow through gravity to produce large-scale structure observable today.

In this model, the Universe has evolved from a homogeneous state after the Big Bang, followed by the inflation that brought quantum fluctuations to cosmological scale anisotropies as observable in the CMB. The continuous expansion of the Universe goes together with a hierarchical assembly of galaxies, clusters and superclusters until our epoch. The energy density ruling this hierarchical assembly seems to be dominated by two mysterious components, the Dark Energy representing about 70% of the energy density and responsible for the expansion of the Universe and the Dark Matter, representing about 25% and responsible for the cosmological scale gravity. The Dark Energy, by its unknown nature, challenges our current knowledge in fundamental physics, either behaving like the Einstein's cosmological constant Λ either like a scalar field evolving in cosmic time. The Dark Matter, presenting possible candidates such as the axions, the Lightest Supersymmetric Particle (LSP) or the massive neutrinos, does not emit light but is noticeable by its gravitational effect on baryonic matter and by deflecting background light.

Euclid is a high-precision survey mission designed to answer these fundamental questions and challenge general relativity on cosmological scales. Euclid has been designed to map the large-scale structure of the Universe over the entire extra-galactic sky out to redshift $z \approx 2$, thus covering the period over which dark energy accelerated the Universe expansion.

Regarding the Dark Energy and Dark Matter, the primary science of the mission, the main questions in fundamental cosmology that Euclid will tackle are[1]:

1. Is the Dark Energy merely a cosmological constant, as introduced by Einstein, or is it a scalar field that evolves dynamically with the expansion of the Universe?
2. Alternatively, is the Dark Energy instead a manifestation of a breakdown of General Relativity on the largest scales?
3. What are the nature and properties of Dark Matter?
4. What are the initial conditions in the Early Universe, which seeded the formation of cosmic structure?

Beyond these breakthroughs in fundamental cosmology, the Euclid Legacy science will contribute to a wide range of astrophysics fields. A relevant Euclid Legacy science for this Thesis will be in the area of galaxy evolution and formation through the production of high quality morphologies, masses, and star-formation rates for billions of galaxies and particularly spectra of tens of millions of galaxies out to z $\approx$ 2, covering the *redshift desert*.

The Euclid Deep Survey will also probe the 'dark ages' of galaxy formation by observing thousands of galaxies together with quasars at z$\geq$6, of which about hundreds of galaxies could be detected at z$\geq$10, subsequently probing the era of reionization of the Universe. These high redshift galaxies and quasars will be critical targets for the James Webb Space Telescope (JWST) and European-Extremely Large Telescope (E-ELT). In the Milky Way, Euclid will also provide complementary information to the Gaia survey taking it several magnitudes deeper and will potentially detect earth-mass exoplanets through the microlensing technique.

We describe in the following the two primary cosmological probes that will be at the core of the Euclid mission. These two probes are the Weak Lensing (WL) and the Galaxy clustering (GC). They have been fundamental when designing the Euclid Payload Module to perform in optimal conditions for these probes up to redshift $\approx$ 2. We will make a special

---

[1] taken from Laureijs et al., 2009

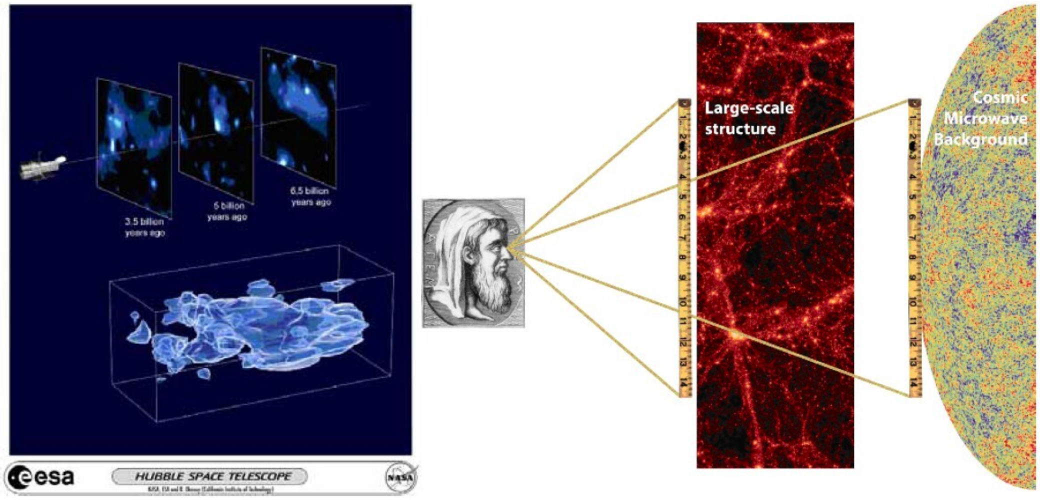

Figure 2.3 Illustration of the two primary cosmological probes of Euclid. Left: The distribution of dark matter measured from the HST COSMOS survey using. Right: Galaxy clustering as a probe of the geometry of the Universe. The same acoustic features (BAO) seen in the CMB can be observed in the distribution of galaxies, providing a standard cosmological ruler [extracted from Laureijs et al. (2009)].

mention of the Euclid spectroscopic channel (NISP-S), which is slitless and of particular interest for this study since we are here providing spectral libraries to simulate the spectra expected from the NISP-S.

2.2.2 The Euclid cosmological probes

Euclid will use a number of cosmological probes to measure the clustering properties but is optimised for two methods:

1. Weak Lensing (WL): measurement of the distortion of the galaxy shapes due to the gravitational lensing caused by the predominantly dark matter distribution between distant galaxies and the observer.

2. Galaxy Clustering (GC): Galaxy clustering enables the direct measurement of the cosmic expansion history, H(z), through the so-called Baryon Acoustic Oscillations (BAO).

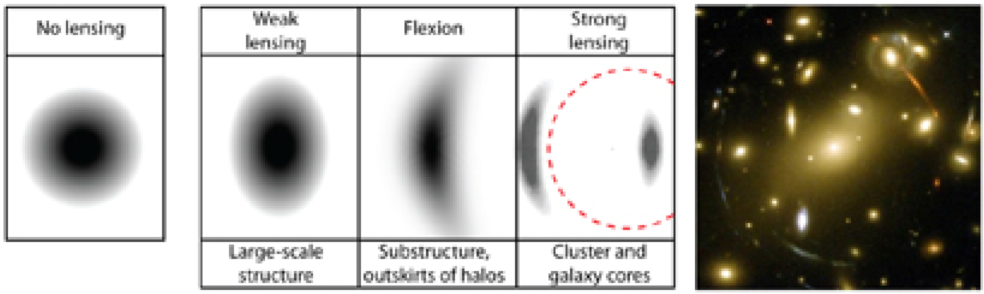

Figure 2.4 Left: Illustrations of the effect of a lensing mass on a circularly symmetric image. Weak lensing elliptically distorts the image, flexion provides an arc-ness and strong lensing creates large arcs and multiple images. Right: Galaxy cluster Abell 2218, strongly lensed arcs can be seen in around the cluster. Every background galaxy is weakly lensed. [Credit for Abell 2218: NASA, ESA, and Johan Richard (Caltech, USA)].

WL and GC can provide information of great importance to study the Dark Energy and Dark Matter. To do so, we require a high image quality for the shear measurements and a massive spectroscopic redshift survey for the GC through the BAO. For both probes, Euclid is designed to provide large statistics and tight control of systematic effects.

Weak lensing

Light is gravitationally deflected by the curvature of space-time around massive objects. Firstly suggested by Einstein in his theory of general relativity, it has been observed during the solar eclipse of May 29, 1919 by Arthur Eddington and Frank Watson Dyson. At that time we were observing the bending by our Sun of the light coming from a star inside our Milky Way, changing its apparent position in the sky. The following major step in the study of gravitational lensing has been the discovery of two "twin" quasars which happened to be two images of a single quasar (Walsh, Carswell, and Weymann, 1979). The effect of gravitational lensing can affect differently the shape of galaxies. The most subtle effect, weak lensing, will make an intrinsically circular galaxy appear as an ellipse. If the light encounters bigger halo of mass on the line-of-sight, the deflection is stronger and can show flexion patterns. Eventually in the most extreme situation the lensing effect can even give rise to multiple images and giant arcs from a single object, the so-called Einstein rings (refer

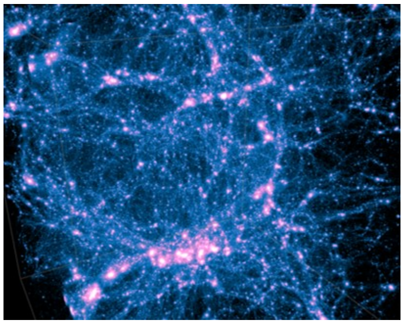

Figure 2.5 Example 3D prediction from ΛCDM cosmology to be confronted with results from the Euclid WL probe [Credit: Illustris Simulation].

to Schneider, Kochanek, and Wambsganss (2006) for further information).

We are particularly interested in the WL effect for its high probability to be found on the line-of-sight. WL can therefore provide an almost direct probe of Dark Matter distribution in the Universe, measuring small systematic distortions of galaxy images from mass inhomogeneities along the line-of-sight. The resulting galaxy shear can then be transformed into matter distribution. The baryonic matter, emitting light, happens to be insufficient to explain the distortions but can rather be explained by an additional matter component approximately six times more important, the so-called Dark Matter, which does not emit light but effectively bends light. The WL made over a large area including a large number of individual galaxies at different redshift is therefore a great tool for 3-D mapping of the Dark Matter, tracking the intervening mass distribution at different cosmic epochs. This can then lead to information on the shape and growth of the power spectrum of density fluctuations.

The WL requires a high-resolution imaging survey that will essentially be provided by the VIS mounted on the Euclid Telescope (see section 2.3.2). For this purpose, Euclid will measure the shape of over 2 billion galaxies with a density of 30-40 resolved galaxies per arcmin^2 in one broad visible R+I+Z band [5,500Å-9,200Å] down to AB magnitudes of 24.5 for the Wide survey and 26.5 for the Deep survey. The high-resolution images required for WL made necessary to design a dedicated space-based telescope.

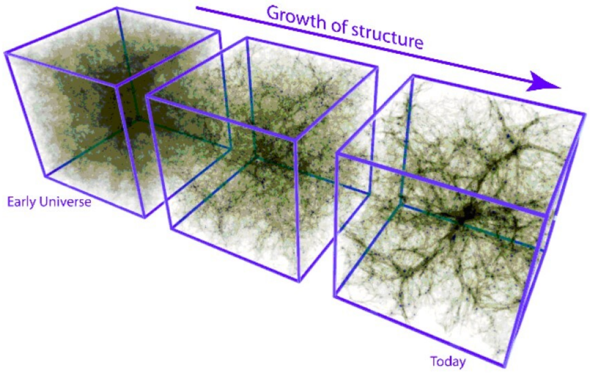

Figure 2.6 Growth of structure in a numerical simulation [Credit: V. Springel].

Galaxy Clustering probe: Baryonic Acoustic Oscillation and Redshift-Space Distortion

GC refers to the 3D distribution of galaxies, measured from the angular positions of galaxies in the sky, and the redshifts of the galaxies for their radial distribution. It enables the direct measurement of the cosmic expansion history, H(z), through the BAO, and the growth history of cosmic large scale structure, $f_g(z) = \Omega_m^\gamma$, through Redshift-Space Distortions (RSD) on large scales. The latter is a deviation of the Hubble's law and is a consequence of peculiar velocities resulting from the gravity that makes large structure to collapse towards each other.

BAOs are wiggle patterns imprinted in the clustering of galaxies and detectable in the power spectrum (see below) which provide a standard ruler to measure the Dark Energy and the expansion in the Universe. BAO is therefore of great interest to study the evolution of the space-time structure, giving direct key information relative to the evolution of the expansion of the Universe. This interest comes from the possibility to measure it at different cosmic time, back to recombination from the CMB radiation. At the time of recombination, the acoustic oscillations in the photon-baryon plasma became frozen imprinting their characteristic signatures on both the CMB through the acoustics peaks and on the matter distribution monitored by the galaxy power spectrum, which is possible to observe at different cosmic time.

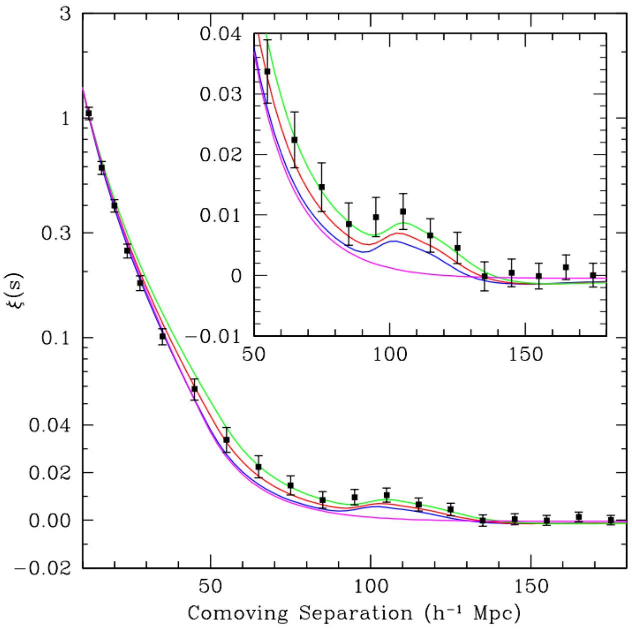

Figure 2.7 The two-point correlation function of SDSS “luminous red galaxies”, in which the BAO peak at 105 h-1 Mpc has been clearly detected (Eisenstein et al., 2005). This detection is a great success, enabling direct comparison with data from the CMB map and over different redshift, offering a powerful tool sometimes referred as a cosmological ruler. This strongly constraints the cosmological parameters and in particular the angular diameter distance.

Nevertheless, since baryons only account for a small fraction of the total matter, which is dominated by Dark Matter, the acoustic peaks of the BAO are out of phase and are much smaller in amplitude than the CMB acoustic peaks. This loss in amplitude doesn’t remove its great interest as a cosmological probe. Indeed, BAO has been observed in the galaxy power spectrum at $0.16 \leq z \leq 0.75$ from the SDSS and BOSS surveys (Einsenstein et al. (2005), Sánchez et al. (2016), and Grieb et al. (2017) and see respectively figure 2.7) with the characteristic scale in agreement with the comoving sound horizon at recombination of ≈ 125 Mpc which has been measured on the CMB maps first made by BOOMERANG (Bernardis et al., 2000), followed by space experiments, the WMAP (Hinshaw et al., 2003) and then using the most accurate made by Planck in the 2010s. Thus BAO has shown a unique potential as a cosmological standard ruler and can measure dark energy with relatively low systematic error comparing to other probes (Albrecht et al., 2009).

The power spectrum P(k) is obtained from the Fourier transformation of the two-point correlation function of the galaxy distribution. The two-point correlation function enables to reveal a preferred redshift separation of galaxies in the radial direction, dz, and in the angular separation of galaxies, $d\vartheta$. Comparing the observed BAO scales gives strong constraint on the evolution of the Dark Energy equation of state parameter $\mathrm{w(z)} = \mathrm{w}_0 + \mathrm{w}_a\mathrm{z}/(\mathrm{z}+1)$. Indeed, the two-point correlation function strongly constraints the Hubble parameter H(z) from the radial distribution and on the angular diameter distance DA(z) from the position on the celestial sphere.

The measurement of the BAO over the entire extra galactic sky out to $\mathrm{z} \approx 2$ requires an accurate determination of the redshift distribution of galaxies of million of galaxies. If we cannot measure the distances of galaxies directly, we can measure the redshift of galaxies using the relation $\lambda_{obs}=\lambda_{rest}(\mathrm{z}+1)$, which can then be converted into distances for a known cosmological model. Euclid mission will enable accurate redshift determination with and error $\sigma_z/(1+z) \leq 0.001$ from spectroscopic studies. An efficient and accurate redshift determination method accounting for the maximum amount of targets is the slitless spectroscopy. After a first estimation through photometry, the precise determination of the redshift required for 3D mapping will be obtained from spectroscopy, tracking nebular emission lines. We mention here that this Euclid characteristic requirement is of particular interest for the study we are presenting. Indeed, the work we present is part of the group of research in charge of simulating spectroscopic observations expected from Euclid. We describe below the concept behind slitless spectroscopy.

2.2.3 The Euclid spectroscopic Legacy survey

Euclid's spectroscopy will enable to collect an unprecedented amount of spectra at a redshift crucial in the Star Formation History study, including the so-called cosmic noon. Indeed, Euclid will collect more than 35 million spectra of galaxies located at $1\leq \mathrm{z} \leq 2$ offering great perspectives for the Euclid Legacy science. It will provide the community with a tremendous amount of data to be studied for the next decades and will therefore significantly increase our understanding of the evolution of galaxies from the cosmic noon to our epoch.

Spectroscopy is of crucial interest when doing astrophysical science. Indeed, an optical

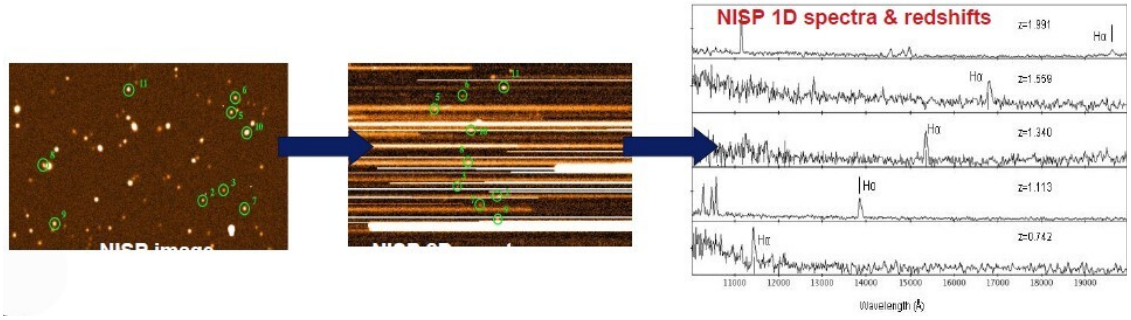

Figure 2.8 Illustration of the strategy to combine imaging and slitless spectroscopy to obtain 1D spectra [Extracted from Moresco (2020)].

rest-frame spectrum alone can tell us the chemical abundance, the amount of dust, the electron density, the age of the stellar population, the pressure of the interstellar medium, and the rate of star formation (see section 4.2) becoming a great tool to study the evolution of galaxies' properties as a function of the environment. Another crucial interest, in particular for the Euclid primary science aiming at studying the Dark Matter using the BAO (see section 2.2.2), is the possibility to infer the redshift from the spectrum using the relation λ_{obs}=λ_{rest}(z+1), with a precision $\sigma_z/(1+z) \leq 0.001$, to be converted in luminosity distance for a chosen cosmology.

Spectroscopy has been done historically using a slit to tightly select the light of the target, avoiding contamination from other sources, and dispersing its light using a grism or prism taking advantage of the wavelength dependent dispersion's law. This requires to clearly define the target before observation and is quite observation time demanding, therefore limiting the amount of possible target to be explored. The advent of multi-object spectrographs gave place to a consequent step forward in the possibility of large spectroscopic surveys, enabling to scope several objects at the same time using a system combining a mask and optic fibers for each aperture of the mask. Results from this multi-object spectroscopy enabled to increase significantly the amount of data available (e.g. VIMOS Le Fèvre et al., 2003, FMOS Kimura et al., 2010), while still controlling the noise from other sources. The Fibre Multi-Object Spectrograph (FMOS) of the Subaru Telescope and its 400 targets

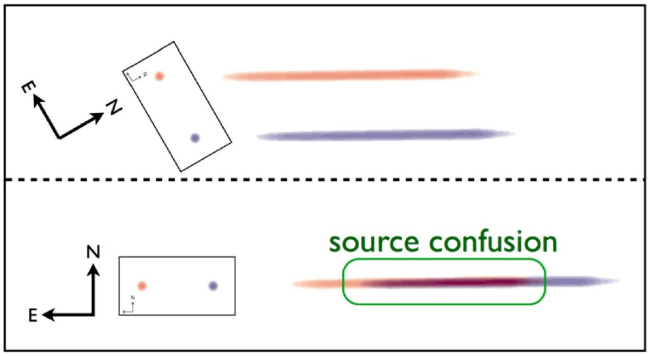

Figure 2.9 Illustrative example of spectral confusion in the case of two Gaussian fixed sources. We see that the overlapping can occur in a specific orientation (bottom) while being removed in another orientation (top) (extracted from Ryan, Casertano, and Pirzkal, 2018).

observed simultaneously in a [9,000Å-18000Å] wavelength range will be extensively cited in this study, covering a similar wavelength range than the NISP spectrometer.

The 3D mapping of Dark Matter together with the study of the equation of state parameter of the Dark Energy require a precise redshift for a significant fraction of the celestial sphere up to a redshift ≈ 2. This will require the use of an accurate and Wide spectroscopic survey. To answer this particular need, the slitless spectroscopy has been chosen, particularly convenient to answer Euclid mission's requirement taking advantage of the Space conditions.

Slitless spectroscopy and data reduction

Slitless spectroscopic consists in removing any form of mask or slit, leaving the entire Field-of-View (FoV) going through the spectrometer. Euclid Slitless spectroscopy will be made with a grism. The grism is a dispersive and transmissive element in a collimated beam to produce a dispersed image of the sky. Firstly implemented on the *HST*, Euclid will benefit from significant advances in the field with previous studies on data reduction from slitless spectroscopy (Pasquali et al., 2006b; Kümmel et al., 2009; Walsh, Kummel, and Kuntschner, 2010; Ryan, Casertano, and Pirzkal, 2018), and has therefore been retained as the best option to fulfill the Euclid requirements. Slitless spectroscopy is particularly enhanced from space thanks to the significantly reduced background emission, getting rid of the emission lines from the atmosphere. Nevertheless, several features still present some difficult aspects to consider while reducing data from slitless spectroscopy survey. Without any physical aperture (slit) to restrict the spatial extension of the incoming light, the 2D spectra unveiled can be thought as a convolution of the source and its spatial profile. This particular feature, enabling spectroscopic study over all the FoV is also responsible for potential overlaps of spectra from the different dispersion orders from the grism, interacting with spectrum from different sources and also creates some spectral resolution dependence on object size, each pixel potentially receiving radiation of any wavelength. A review of some of the main issues encountered while doing slitless spectroscopy has been presented by Pasquali et al. (2006b). Here we highlight some of the main ones:

1. The extension of a source along the dispersion axis is given by the spatial profile of the object and affects the achievable spectral resolution (see figure 2.10). We present in section 6.4.2 a review of this effect on the simulated spectra from the NISP simulator.

2. The zero point of the grism wavelength calibration is defined by the position of the object in the direct image. When no direct image of the source is available, the position of the zeroth order can also be used, although in a less accurate way.

3. The spectroscopic flat field is field and wavelength dependent.

4. Each pixel in a grism spectrum receives a contribution from the background emission that is integrated over the entire spectral range of the grism.

5. Depending on the luminosity of a source, grism orders higher than 1 (at higher X-coordinates in the grism image) and grism negative orders (at lower X-coordinates) can be identified. No filter can be used to suppress higher and negative orders.

6. Depending on the position of the object in the direct image, the source spectrum can be truncated in the grism image. Objects outside the FoV can still produce spectra in the grism image (see figure 2.8).

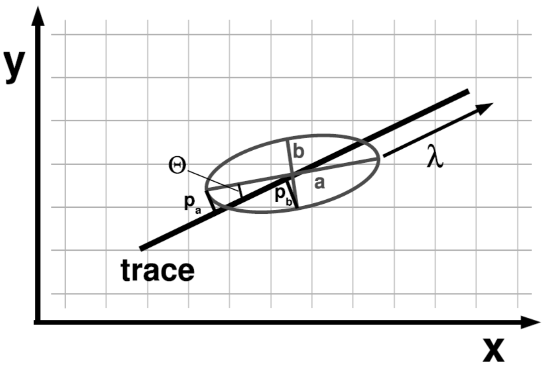

Figure 2.10 An illustration of the parameters for defining the extraction geometry. The object morphology is described as a 2D Gaussian with major and minor half axes a and b and the angle Θ, here defined with respect to the dispersion or trace direction. The quantities pa and pb are the projection of the major and minor half axis onto a plane perpendicular to the trace [extracted from Kümmel et al., 2009].

7. The extension of grism spectra and the number of their orders can create overlap and contamination among spectra of adjacent objects.

All this together requires a direct image taken concurrently with the dispersed imaging to help identify individual sources. Moreover, a specific software is required to cope with the challenging task of data reduction from a slitless mode to obtain a 1D spectra enabling to do science and perform the redshift measurement. We mention here that the latter can be done either manually, either using a tool for automatic redshift measurement such as EZ (Garilli et al., 2010). We now present two Software designed for slitless spectroscopic survey data reduction. For example, the instrument independent reduction package aXe, originally developed for the *HST* Advanced Camera for Surveys (ACS) grism and prism spectroscopy has been developed (Kümmel et al., 2009). It has also been successfully applied to Near-Infrared Camera and Multi-Object Spectrometer (NICMOS) slitless data (Freudling et al., 2008) mounted on the *HST*.

Another Software has been proposed by Ryan, Casertano, and Pirzkal (2018), initially designed for the Wide Field Camera 3 (WFC3) of the *HST* to deal with a collection of slitless spectroscopic images, ideally taken at a variety of orientations, dispersion directions, or dither positions, able to extract 1D spectra in crowded fields of galaxies, such as expected from the Euclid Spectroscopic survey. Indeed, Euclid will perform a self-consistent method consisting in observing with two grisms, with a modifiable dispersion angle, facilitating the

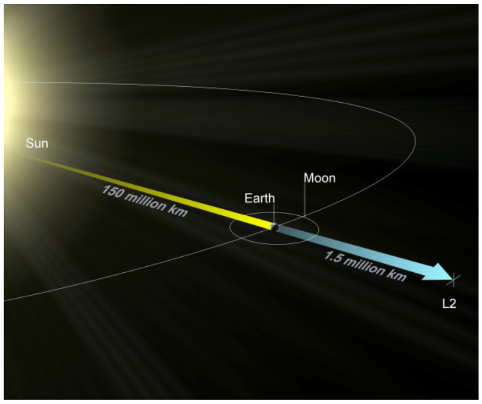

Figure 2.11 The second Sun-Earth Lagrange point (L2) is situated some 1.5 million km from the Earth on the line defined by the Sun and Earth [extracted from https://sci.esa.int/s/WXJQGXA*].*

identification of the objects with their corresponding spectra (see section 2.3.3).

2.2.4 Observation Scheme of the Euclid Mission

Observation from the Sun-Earth system's Lagrangian point L2

To achieve the cosmological probes presented above, measurements of the shapes and redshifts of galaxies need to be obtained over very large volumes and with very high precision, as required to perform the WL and BAO. Some characteristics have therefore to be defined to design optimal observations conditions to fulfill Euclid's requirement, in particular the mission has been planned to observe from Space, at the Sun-Earth system Lagrangian point L2 (see figure 2.11). We present here a review of the main aspects that made necessary to design a space telescope instead of a ground based telescope.

1. The Point Spread Function (PSF) which is of particular interest for the WL analysis will be diffraction limited, getting rid of the variability and statistical subsequent errors while significantly increasing the resolution offering a constant diffraction limited PSF (i.e. λ/D), where D is the diameter of the telescope and λ the wavelength, avoiding atmospheric seeing and airmass.
2. The night sky, as seen from Earth, presents emission lines that would highly interfere with the spectrum of galaxies, adding some background complicating the already very

complex slitless set-up described above. Moreover, observing in the NIR (8,000Å to 20,000Å), as required to catch optical rest-frame lines up to z $\approx$ 2, Euclid would face an absorption of about 30% from the atmosphere, critically affecting the S/N ratio. Observing from space is a great alternatives to cope with these sources of systematic effects.

3. The earth glow (i.e. thermal emission from earth) is critical when observing in the NIR. L2 is a first choice of area to limit the Earth glow interfering with the light coming from the targets. Indeed, with its 1.5 million kilometers away from Earth, its location is ideal to avoid either thermal or magnetic contamination coming from the Earth-Moon system.
4. The Euclid wide survey can be performed completely without occultation or illumination of the payload by Sun, Earth or Moon, which is advantageous for obtaining a homogeneous survey.

1/2/3/ are sources of small statistical and systematic errors and make necessary the stable observing conditions in space free of atmospheric effects and 4/5/ make the choice of the L2 the best option for the telescope position in space.

All this together, it has been decided to place the Euclid telescope around the Sun-Earth second Lagrangian point (L2) at 1.5 million kilometers away from Earth. It will ensure stable thermal and observing conditions. This orbit has the great advantage that there are no disturbances by the Earth magnetic field or Moon, no thermal perturbations and variation, and no gravity gradient as it is the case for Earth bound orbits.

The Euclid Wide and Deep Fields

The Euclid will explore the darkest sky, the sky free of contamination by light from our Galaxy and our Solar System. That is the extragalactic sky, defined by the regions with galactic longitude |b|>30 degrees and also avoiding the ecliptic plane (see figure 2.12). The

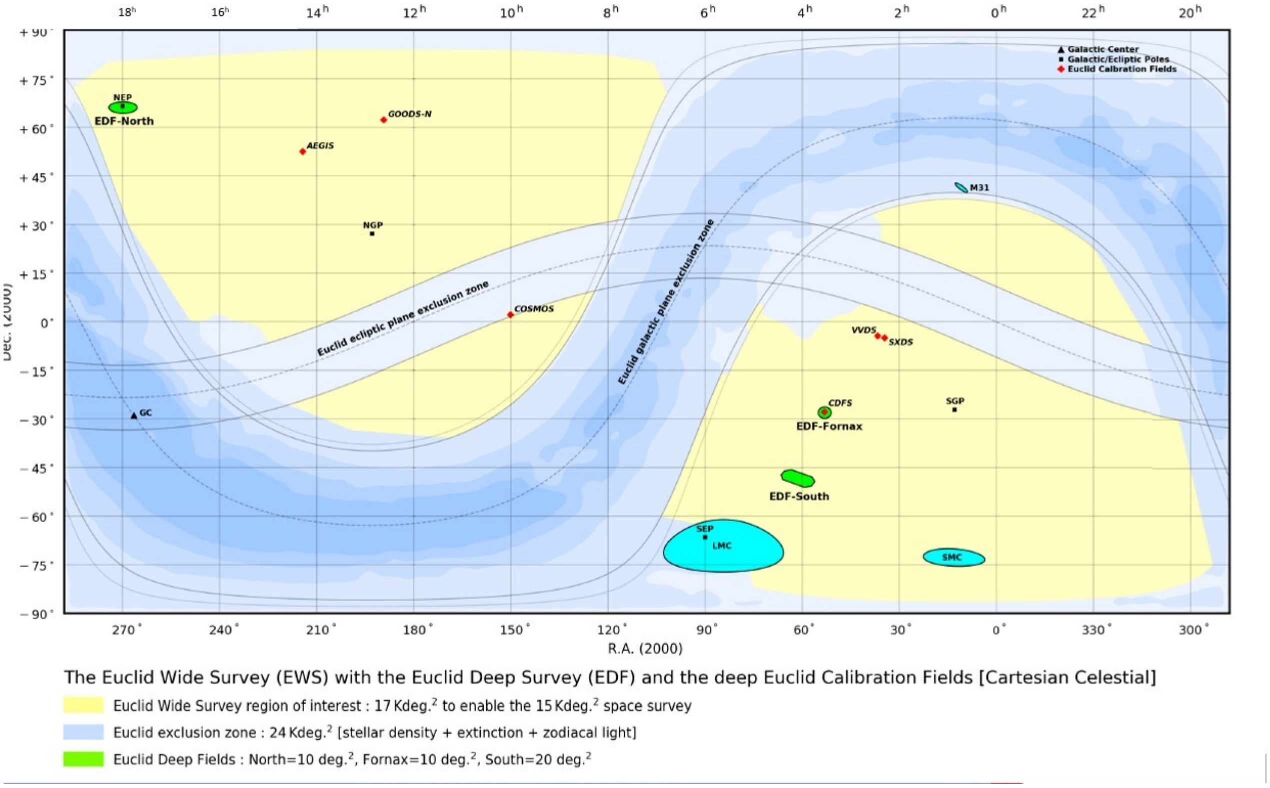

Figure 2.12 Map extracted from Tereno (2020) and made by J.C. Cuillandre and the Euclid Survey Working Group.

mission is oganized around a Wide field survey, aiming at exploring roughly one third of the extragalatic sky, and a Deep field survey to explore deeper some specific areas.

On a daily basis, Euclid will observe strips ≈ 20 degrees long, which corresponds on a monthly basis to ≈ 400 deg^2 and ≈ 15,000 deg^2 over the 6 years of observations (considering all the idle time between exposures). The wide survey is the core of the study of the Dark Universe, where the WL, BAO and RSD signals will be measured.

The Euclid program includes observations of three "Euclid Deep Fields" covering around 40 deg^2 in total, aiming at calibrating the Wide field and to extend the scientific scope of the mission to the high-redshift Universe, observing faint galaxies, quasars and AGNs. Deep field patches of at least 10 deg^2 which are 2 mag (=6.3 times) deeper than the wide survey (see table 2.1). Since the Deep field employs the same observing mode as the Wide survey, the data acquisition rates are similar, thus no additional requirements for the dataflow will

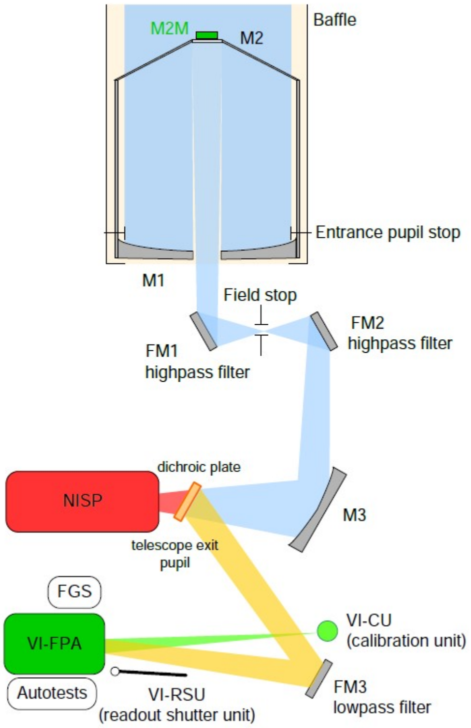

Figure 2.13 Overview of the PLM subsystems made by Airbus Defence and Space and retrieved from https://www.euclid-ec.org/?page_id=2639.

be required. The Deep field data will be obtained by combining exposures made in the Wide field configuration.

2.3 The Euclid Payload Module (PLM)

The Euclid's Payload Module is composed of a telescope, a thermal control system, a fine guidance system, a Visible Imager (VIS) and a Near Infrared Spectrometer and Photometer (NISP) instrument. In the scope of this Thesis we are particularly interested in the NISP detector and for completeness we will also briefly present the telescope and the VIS detector. Indeed, the slitless spectroscopy survey will be performed combining data from the photometers, i.e. the VIS and NISP-P, to infer the continuum and a first redshift approximation. The NISP-S will then provide a more accurate redshift determination together with the fluxes of the nebular emission lines.

Euclid will then be equipped with a telescope made by Airbus (Defence and Space) feeding

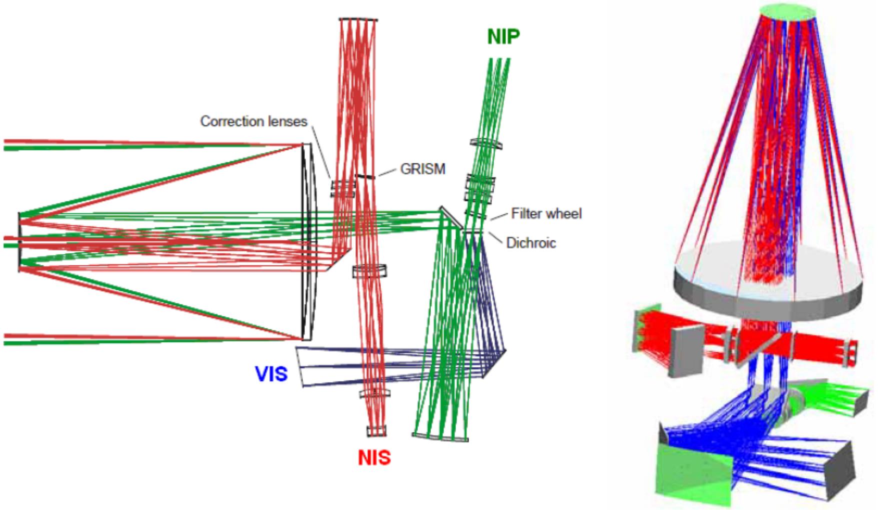

Figure 2.14 Euclid optical design (blue-VIS, green-NISP-P, red-NISP-S) [extracted from Laureijs et al. (2009)].

2 instruments, the VIS and NISP. The VIS is a high quality panoramic visible image. The NISP consists in a near infrared 3-filter (Y, J and H) photometer (NISP-P) and a slitless spectrograph (NISP-S). The alliance between spectroscopy and photometry will enable to efficiently measure the WL and the BAO, crucial tracers of the Dark Universe and to improve our understanding of the evolution of the Universe structure going from the Cosmological Microwave background (CMB) to the local clusters of galaxies. The visual imager (VIS) will perform in the optical frame while the NISP will cover the NIR. The VIS will provide high quality images to carry out the WL galaxy shear measurements and the NISP will perform imaging photometry for photometric redshifts measurement, while also performing slitless spectroscopy to obtain spectroscopic redshifts and lines' flux measurement.

To accomplish the Euclid mission ESA has selected Thales Alenia Space for the construction of the satellite and its service module and Airbus (Defence and Space) for the Payload Module (PLM). The PLM is under the responsibility of Airbus (Defence and Space). It comprises the telescope, the PLM thermal control system, the Fine Guidance Sensor (FGS), the VIS and NISP instruments (delivered to Airbus Defence and Space division by the Euclid Consortium) and the detectors (delivered by ESA).

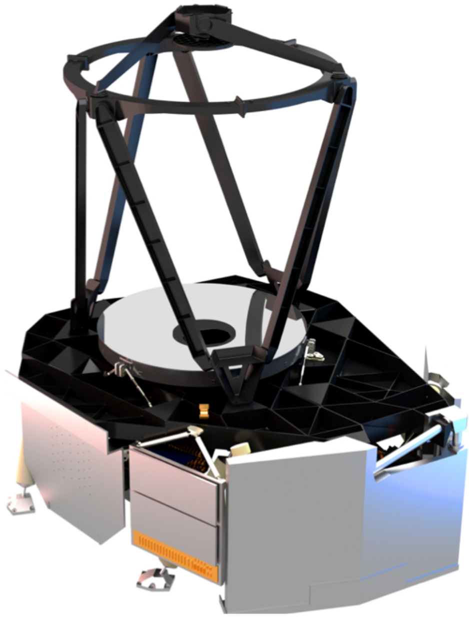

Figure 2.15 The Euclid telescope The Euclid, a 1.2-m-diameter Korsch telescope. The primary (M1) mirror has a diameter of 1.2 m; the secondary mirror (M2) has a diameter of 0.35 m (Source: https://sci.esa.int/s/wK5nNP8).

2.3.1 The telescope

The Euclid Payload Module is equipped with a Korsch telescope and its primary mirror of 1.2 m diameter. Korsh telescopes, also known as three-mirror anastigmat telescopes, provide a configuration that enables to limit the coma, astigmatism, spherical aberrations (particularly important for the Euclid's wide FoV) and stray light, and to obtain a flat image on the detector.

The telescope is an on axis 3-mirror Korsch cold telescope providing a wide FoV of 1.25 x 0.727 deg^2. The mirrors and structures are all made in Silicon Carbide, a material with excellent thermo-elasticity and stifness and very resistant to radiations, characteristics mandatory when observing from Space at L2 and to ensure optimal performances for the high quality image required for the Euclid mission. The telescope design comprises a 3 degree-of-freedom mechanism on the secondary mirror to focus and for tilt correction.

2.3.2 The Visual imager (VIS)

The visible (VIS) instrument is under the responsibility of the Euclid Consortium. VIS aims at imaging in the optical band all galaxies of the Euclid survey with very high image quality.

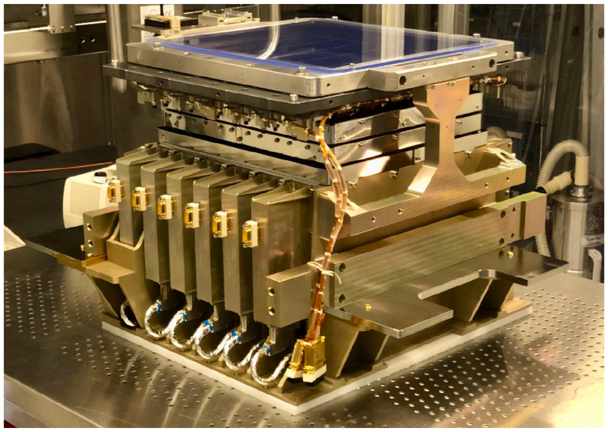

Figure 2.16 VIS, the visual imager of the Euclid mission.

It will be used to measure the shapes of galaxies and derive the gravitational lensing effects induced by large scale structures of the Universe on distant background galaxies. It will therefore probe how the dark matter is distributed and how its distribution changed over the last 10 billion years.

The VIS focal plane is composed of a matrix of 36 full frame types 4k4k pixels. CCDs (Charge Coupled Devices). The VIS focal plane covers a FoV of 0.57 deg^2 with 0.1 arc-second covered by each pixel.

VIS will be equipped with one single broad band filter, covering the wavelength range from 5,500Å to 9,200Å. VIS will be able to get a signal-to-noise ratio of at least 10 for 1.5 billion galaxies down to magnitude 24.5 in 4000 seconds.

2.3.3 The Near Infrared Spectrometer and Photometer (NISP)

The Near Infrared Spectrometer and Photometer (NISP) (we refer the reader to Maciaszek et al., 2016 for further information) instrument consists in a photometric channel (NISP-P) and in a spectroscpic channel (NISP-S). The NISP focal plane is composed of a matrix of 16 2k2k 18-micron pixel Teledyne TIS detectors covering a FoV of 0.53 deg2 shared with VIS, with 0.3 arc-second pixels. An overview of the NISP subsystems is shown on the figure 2.17. The overall throughput of the NISP instrument will enable scientists to measure photometric and spectroscopic redshifts of galaxies with sufficient accuracy. The NISP photometer is expected to get a signal-to-noise ratio of at least 5 down to magnitude 24.0 in about 100 seconds per filter. The NISP spectrograph will provide redshift of about 30 million galaxies over the redshift range 0.5 to 2.0.

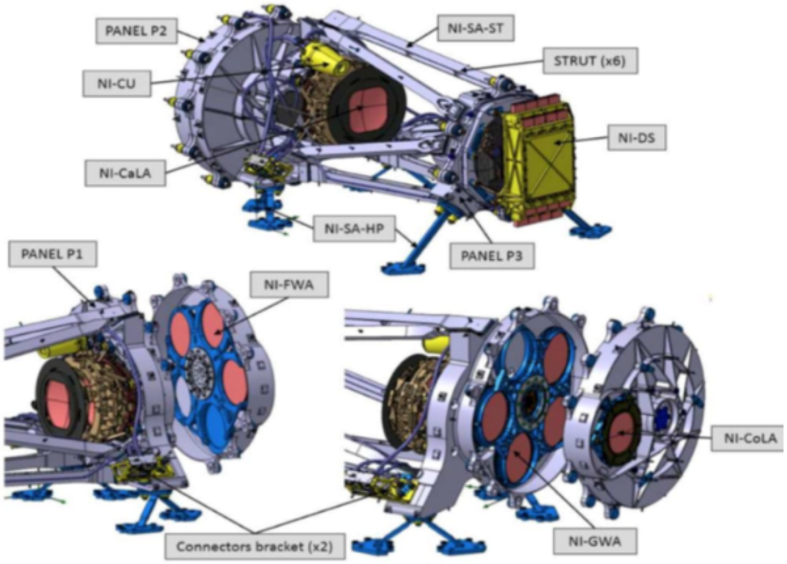

Figure 2.17 Overview of the subsystems composing the NISP instrument. The top panel shows the elements of the NISP Opto-Mechanical Assembly and Detector Assembly: NISP Calibration Unit (NI-CU), NISP Camera Lens Assembly (NI-CaLA), NISP Structure Assembly (NI-SA-ST and NI-SA-HP as for Structure and HexaPodes, respectively), NISP Corrector Lens Assembly (NI-CoLA) and the NISP Detector System (NI-DS). NI-FWA and NI-GWA are the NISP Filter Wheel Assembly and the Grism Wheel Assembly, respectively.

In combination with the VIS, the NISP-Photometer aims at providing near infrared (from 9,000Å to 20,000Å) photometry of all galaxies observed. The near infrared photometry will be combined with VIS data to derive photometric redshifts and rough estimates of distances of galaxies seen by VIS. The photometric channel will be equipped with 3 broad band filters, Y, J and H covering respectively the wavelength ranges [9,000Å-11,920Å], [11,920Å-15,440Å] and [15,440Å-20,000Å].

The NISP-S mounted on the Euclid telescope will enable to track the strong spectral features in the optical rest-frame. The near infrared spectra will be used to derive accurate redshifts. The NISP-S will detect predominantly Hα emission lines of the galaxies. It will

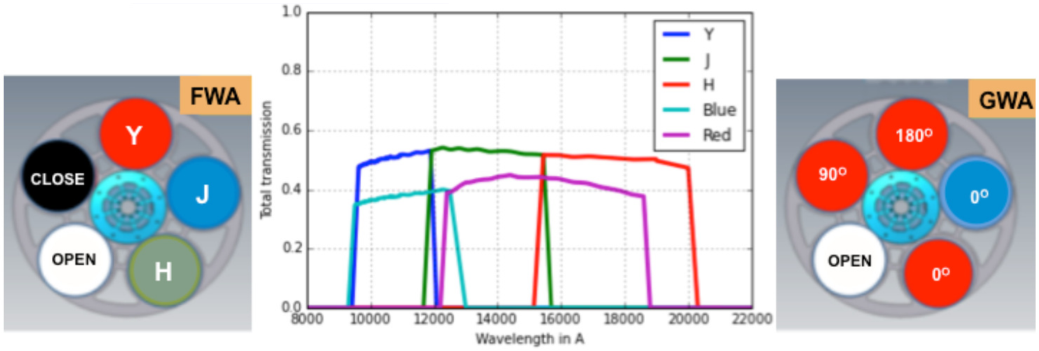

Figure 2.18 The bottom panel shows the filter positions (left), grism positions (right) and the transmission curves of the Y, J and H filters and the blue and red grims (Extracted from https://www.euclid-ec.org and made by the Euclid Consortium/NISP team).

contribute to the Euclid primary cosmological probe by making possible a redshift determination with an accuracy of $\sigma_z/(1+z) \leq 0.001$ for more than 35 million galaxies, as required for the BAO study (see section 2.2.2). The limiting line flux level for the Euclid Wide field survey is predicted to be 2×10^{-16} erg s^{-1} cm^{-2} (as presented for example in Valentino et al., 2017).

The spectroscopic channel will be equipped with 3 different low resolution near infrared grisms (R=380 for a 0.5 arc-second diameter source), 2 “red” [12,220Å–18,770Å] and 1 “blue” [9,200Å–12,500Å], but no slit (i.e. slitless spectroscopy). The two red grisms will cover the same wavelength range but will provide spectra with three different orientations (0, and 180 ± 4) in order to decontaminate each slitless spectrum from possible overlapping spectra of other sources in the field. The ± 4will be possible to realize by tilting the 2 grisms, this is the so-called "K configuration".

The NISP instrument has one additional blue grism covering the wavelength range [9,200Å-13000Å]. This extra grism is suited for the investigation of the high redshift Universe with the prospect of detecting luminous Lyman-alpha emitting galaxies at a redshift z $\geq$ 6.5 and Active Galactic Nuclei (AGNs) over a broader redshift range.

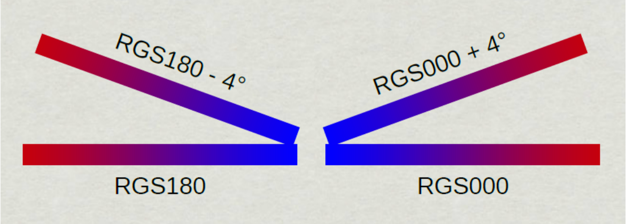

Figure 2.19 Tilted grism observing sequence with the possibility to tilt the grisms RGS000 and RGS180 of respectively -4° and +4°, known as the 'K' sequence [extracted from Haussel, 2020].

	Wide Survey	Deep Survey
AREA (deg^2)	15,000	40
IMAGING (VIS-NISP-P)	VIS H(AB)$\leq$24.5 NISP-P H(AB)$\leq$24	H(AB)$\leq$26.5 NISP H(AB)$\leq$26
SPECTRO (NISP-S)	Red grism - Flux(line)$\geq 2 \times 10^{-16}$ CGS H(AB)$\leq$19.5	Red grism Blue grism Flux(line)$\geq 6 \times 10^{-17}$ CGS H(AB)$\leq$21.5

Table 2.1 Recap of the VIS and NISP specifications (source: Racca et al. (2016) and Moresco (2020)). The VIS filter covers the wavelength range [5,500Å-9,200Å]. The NISP-P filters (Y, J, H) respectively cover [9,000Å-11,920Å], [11,920Å-15,440Å] and [15,440Å-20,000Å]. The red and blue grisms covers [12,220Å–18,770Å] and [9,200Å–12,500Å].

Chapter Three

Data, sample selection and characterization

In this chapter, we first present the publicly released catalogs used to construct the incident spectra (see section 3.1) and we then present the characterization of the sources selected for our study, according to their redshift and luminosity (see section 3.2).

3.1 The Photometric and Spectroscopic Deep Surveys as a starting point

Our study uses observation data released by the Cosmic Assembly Near-infrared Deep Extragalactic Legacy Survey (CANDELS) (Grogin et al., 2011; Koekemoer et al., 2011) and from the COSMOS survey (Scoville et al., 2007). These surveys provide a combination of multiwavelength data that has been of crucial importance in the past years, using data from several telescopes both from ground-based observatories, such as VLT, KPNO 4m, LBT, GTC, Subaru, and CFHT and from space-based ones, such as *HST*, *Spitzer* and Herschel. CANDELS used 5 widely separated fields including the Great Observatories Origins Deep Survey-North (GOODS-N) and a strip of the Cosmic Evolution Survey (COSMOS) fields to which we will refer extensively in this Thesis. We mention here that all the fields covered by CANDELS will also be probed by the Euclid Deep survey. The spectroscopic sensitivity of the most important observational campaigns in CANDELS and COSMOS is approximately

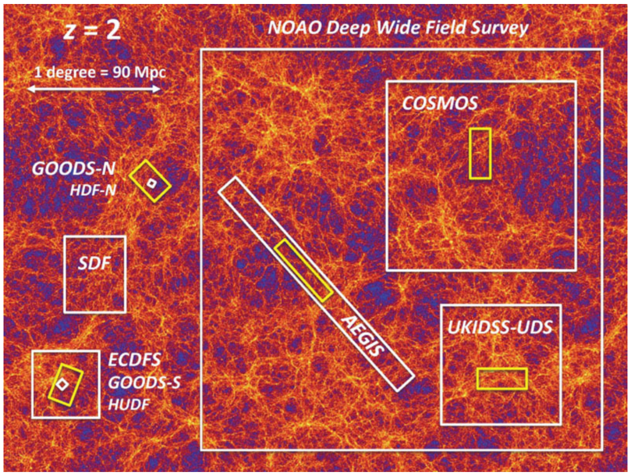

Figure 3.1 Relative sizes of different fields observed in several important surveys of the distant Universe. In particular we can see the Great Observatories Origins Deep Survey North (GOODS-N) and the COSMOS fields. The yellow boxes indicate the five fields from the Cosmic Assembly Near-Infrared Deep Extragalactic Legacy Survey (CANDELS) [extracted from Madau and Dickinson, 2014].

one order-of-magnitude deeper than the expectations from the Euclid Wide survey, offering a great database as a starting point to push the Euclid simulated spectra towards the lower detection limit exploiting a fairly large sample of galaxies with multi-wavelength spectroscopic and photometric data. Sampling different region of the celestial sphere enables reducing the cosmic variance while offering statistically robust and complete sample of galaxies, such that using widely separated fields is a good strategy when sampling the celestial sphere.

In this work, we build two different catalogs, as well as the relative set of incident spectra, aiming at exploring separately the Euclid performance expected for the Deep, and Wide field configurations (see chapter 6.1 for further information on the Deep and Wide fields configurations). To prepare a representative target sample, we make use of two different catalogs of real galaxies. For the Deep field, we refer to the CANDELS/GOODSN field using the extensive catalog BARRO2019 (Barro et al., 2019, hereafter B19), that we have complemented with the morphological parameters derived by Van Der Wel et al. (2012) and by Dimauro et al. (2018). For the Wide field, we refer to the COSMOS field using the catalog COSMOS2015 (Laigle et al., 2016, hereafter L16). This choice is motivated by the fact that the brightest galaxies are those expected to be detected in the Euclid Wide survey, while the Deep survey will also detect emission lines from intermediate-mass galaxies, making the L16 and B19 catalogs appropriate for the Wide and Deep surveys respectively (see section

3.1.1 and 3.1.2 for a description of the samples).

the GOODS-N field covers ≈ 160 arcmin^2 near the iconic Hubble Deep Field North (HDF-N) (Williams et al., 1996) while the COSMOS field covers a larger area of 1.7 deg^2 (see figure 2.12). Hence, the L16 catalog includes a larger percentage of those rare, very massive and bright galaxies at intermediate, and high redshift, compared to the GOODS-N field, which is instead mostly targeting galaxies of intermediate stellar mass.

In both cases (i.e. for the catalogs L16 and B19), we use the publicly released photometric catalogs, complemented with photometric and spectroscopic redshifts, and SED-fitting parameters, to build the spectral continuum, and to predict emission line properties for each galaxy, as detailed below. In particular, beyond the primary information on the redshift, we use the Star Formation History (SFH), Stellar Mass (M_*), stellar age, and the reddening parameter due to dust extinction ($\mathrm{A_V}$). These parameters are presented in the catalogsB19, and L16 an retrieved with LePhare SED-fitting Software, Arnouts and Ilbert, 2011) to associate to each galaxy the corresponding best-fit high-resolution spectral continuum, from Bruzual and Charlot, 2003 population synthesis model. Then we derive expected emission line properties mostly based on the galaxy M_*, SFR, and $\mathrm{A_V}$.

3.1.1 The Euclid Wide Survey starting from the COSMOS2015 catalog

We rely on the L16 catalog to build our Euclid Wide Survey-like simulated spectra[1]. This catalog contains an updated version of the photometry and photometric redshifts, together with estimates of parameters such as the stellar mass, dust extinction, and SFR obtained from SED-fitting. It covers the entire COSMOS field with more than half a million sources over the 1.7 deg^2 COSMOS field.

The data have been retrieved using the YJHK images from the UltraVISTA-DR2 survey, the Y-band of the Subaru/Hyper-Suprime-Cam and infrared data from Spitzer Large Area

---

[1] The Wide field configuration includes 4 frames while the Deep field includes 20 frames. See chapter 6.1 for further details on the Wide and Deep field configurations

Survey with Hyper-Suprime-Cam (SPLASH). The COSMOS survey also includes several spectroscopic surveys such as the 3D-HST (Momcheva et al., 2015), FMOS (Kashino et al., 2019), and LEGA-C (Wel et al., 2016), detecting some of the emission lines of interest in this study. We will therefore be able to compare our calculated emission lines' fluxes with observations.

We select sources with $17 \leq \mathrm{H(AB)} \leq 24$ and with redshift between 0.3 and 2.5. This selection criteria provides us with 24,259 sources. We present in table 3.1 a qualitative description of this sample.

3.1.2 The Euclid Deep Survey starting from the BARRO2019 catalog

For the Deep field simulation, we refer to the GOODS-N field and the catalog B19, that we complemented with results of Sérsic profile fits from CANDELS imaging mosaics (Van Der Wel et al., 2012), and the Bulge/Disc decomposition from Dimauro et al., 2018. This sample includes, on average, fainter galaxies compared to the L16 catalog mentioned above. As detailed below, the catalog B19 provides all the required data to build the incident spectra to be fed to the NISP-S simulator. As a value-added catalog, B19 also includes spectroscopic redshifts, and emission line fluxes from the HST/WFC3 grisms G102, and G141, that we use as term of comparison for our emission line predictions. The analysis of the simulations will be presented in the chapter 6.

The catalog contains 35,445 sources. The multi-wavelength photometry has been performed in the U band with the KPNO and LBC, in the optical using the HST/ACS, in the NIR using the HST/WFC3, the SUBARU/MOIRCS Ks, the CFHT/Megacam and *Spitzer*/IRAC and in the far IR using the *Spitzer*/MIPS, the HERSCHEL/PACS and SPIRE. The catalog also includes optical medium-band data in 25 consecutive bands from the SHARDS, and spectroscopic observation from the HST/WFC3, which we will refer to as term of comparison for the continuum (see section 5.3), and emission lines' fluxes calculated (see section 5.1), respectively. Sérsic model fits for these objects are produced with `GALFIT` (Peng et al., 2010) in all available near-infrared filters (H_{F160W}, J_{F125W} and Y_{F105W}).

We select sources with $17 \leq H(AB) \leq 26$ and, as previously done for the L16 catalog, with redshift between 0.3 and 2.5. This selection criteria provides us with 16,938 out of the 35,445 sources contained in the B19 catalog. A qualitative description of this sample, including the ranges covered in H-band magnitudes, stellar mass, and SFR in different redshift bins is presented in table 3.1.

3.2 Characterization of the sample

After selecting the sources of interest in the two catalogs L16 and B19, we present in the following the characterization of the sample. For better clarity and consistency with literature we perform the sample analysis on 5 different redshift bins [0.3;0.5], [0.5;1], [1;1.5], [1.5;2.0], [2.0;2.5]. We mention here that the creation of the incident spectra from the catalogs L16 and B19 throughout this work have been brought to completion, the simulations are still on-going and up to now they have been performed only for the incident spectra based on the B19 catalog and in the Wide field configuration. We recall that the B19 catalog was initially created for the Deep field configuration. Thus, since the study presented in this Thesis has been brought further using the B19 catalog, we will describe in the following the GOODS-N sample whose simulated spectra will be analyzed in chapter 6. The characterization of the COSMOS sample will be presented in appendix and their corresponding simulated spectra will be created in the next future.

3.2.1 Passive and active galaxies identification: The UVJ-diagram

In this work, and in particular when calculating the predicted fluxes for the emission lines of interest, we refer to calibrations established for Star Forming Galaxies (SFG). In order to evaluate our sample and discriminate SFGs from passive galaxies we refer to the passive iden-

Sources selected from the COSMOS2015 catalog covering the COSMOS field

Redshift bins	# sources (# with morph)	H(AB)	log($M_\star/M_\odot$)	log(SFR)	Av	log(Age/yr)	R$_e$[arcs]	n	log(tau/yr)
$0.3\leq z \leq0.5$	7,356 (7,240)	17-23.5	8.0-11.7	-19.91-2.28	0-3.2	8.0-10.0	0.01-14.3	0.2-9.0	8.0-10.0
$0.5< z \leq1.0$	14,603 (13,932)	17.3-24	8.6-11.7	-19.49-2.83	0-3.2	8.0-9.9	0.02-13.4	0.2-9.0	8.0-10.0
$1.0< z \leq1.5$	1,830 (1,389)	18.7-23.6	8.8-11.8	-10.35-2.95	0-3.2	8.0-9.7	0.03-6.3	0.2-9.0	8.0-10.0
$1.5< z \leq2.0$	362 (271)	19.8-23.8	9.4-11.5	-9.58-2.98	0-3.2	8.0-9.6	0.0-12.8	0.2-6.4	8.0-10.0
$2.0< z \leq2.5$	108 (76)	20.5-23.5	9.4-11.5	-3.01-2.71	0-2.4	8.0-9.4	0.1-14.2	0.3-8.7	8.0-10.0

Sources selected from the BARRO2019 catalog covering the CANDELS/GOODS-N field

Redshift bins	# sources (# with morph)	H(AB)	log($M_\star/M_\odot$)	log(SFR)	Av	log(Age/yr)	R$_e$[arcs]	n	log(tau/yr)
$0.3\leq z \leq0.5$	1,625 (1,569)	17.3-26	7.0-11.2	-8.6-2.23	0.0-4.0	7.6-10.0	0.02-14.2	0.2-8.0	8.5-10.1
$0.5< z \leq1.0$	5,800 (5,601)	17.0-26	8.0-11.6	-10.36-2.69	0.0-4.0	7.6-9.9	0.02-14.6	0.2-8.0	8.5-10.1
$1.0< z \leq1.5$	3,976 (3,829)	19.2-26	8.5-11.5	-14.05-3.0	0.0-3.9	7.6-10.1	0.02-14.7	0.2-8.0	8.5-10.1
$1.5< z \leq2.0$	3,404 (3,247)	19.7-26	8.0-11.7	-12.35-3.05	0.0-3.7	7.6-9.7	0.02-14.3	0.2-8.0	8.5-10.1
$2.0< z \leq2.5$	2,133 (2,068)	18.5-26	8.9-12.0	-7.61-3.46	0.0-3.4	7.6-9.5	0.02-12.8	0.2-8.0	8.5-10.1

Table 3.1 Top: Description of the SED-fitting parameters of the 24,259 sources selected out of the ≈300,000 sources in the L16 catalog. Bottom: Description of the SED-fitting parameters of the 16,938 sources selected out of the 35,445 sources contained the B19 catalog sampling the CANDELS/GOODS-N field. H(AB) is the H band magnitude in the AB system. The SFR is in $M_\odot yr^{-1}$. R$_e$[arcs] is the half-light semi-major axis of the galaxy and n is the Sérsic index. We indicate in parenthesis (# with morph) the amount of sources with morphology available (i.e. either the Sérsic index, either the R$_e$). The SFH is exponentially declining as exp(-t/tau).

.

tification criteria as proposed by Williams et al. (2009) using the color-color UVJ-diagram (see figure 3.2), as follows:

$$\begin{cases} (U-V) > 0.88(V-J) + 0.69 \ \text{if} \ z \in [0.3; 0.5] \\ (U-V) > 0.88(V-J) + 0.59 \ \text{if} \ z \in [0.5; 1.00] \\ (U-V) > 0.88(V-J) + 0.49 \ \text{if} \ z \in [1.0; 2.0] \ \text{(extended up to z=2.5)} \\ U-V > 1.3 \quad \text{for all redshift bins} \end{cases} \tag{3.1}$$

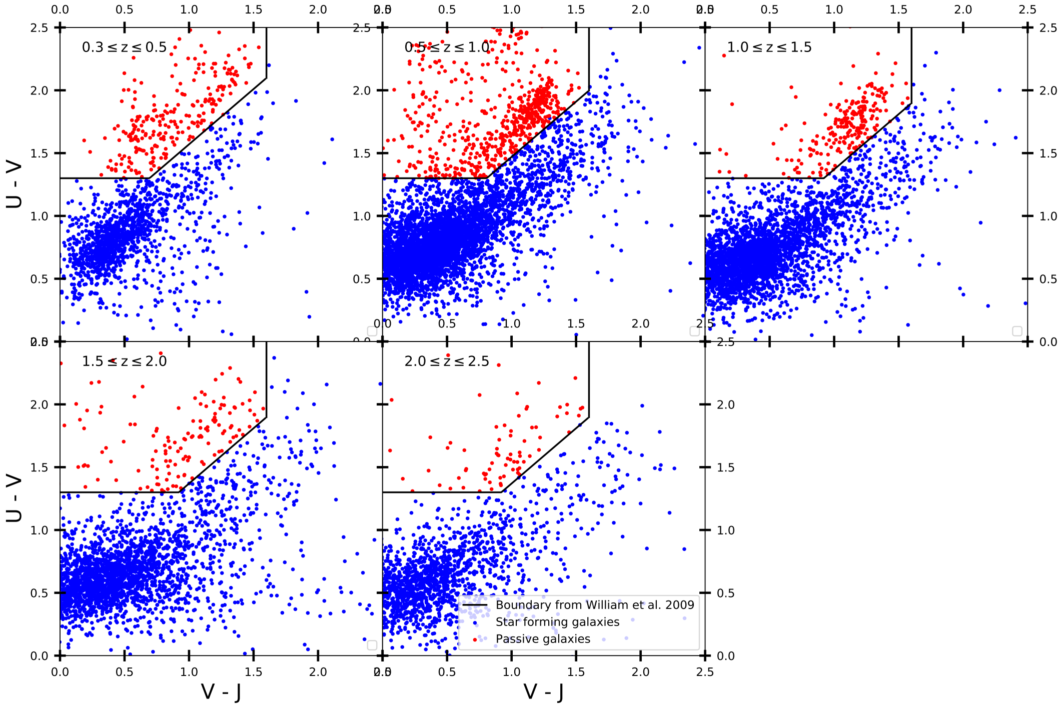

Figure 3.2 UVJ-diagram of the Deep field sample (GOODSN) with the boundaries to separate SFGs (blue dots) from passive galaxies (red dots) as proposed by Williams et al. (2009)

3.2.2 The ***Main sequence***

It is interesting to characterize our sample in terms of Star Formation Rate. It is well known that SFGs lie on a tight sequence in the $M_\star$-SFR plane, referred as the Main Sequence (MS) (Noeske et al., 2007; Daddi et al., 2007; Wuyts et al., 2011; Rodighiero et al., 2011, 2014, and many others). It has been shown that the normalization of the MS is shifted towards higher SFR with increasing redshift reaching a peak between redshifts $z = 1.5$ and $z = 3$, and steadily declining (Madau, Pozzetti, and Dickinson, 1998; Madau and Dickinson, 2014). We use here the normalization of the MS derived by Rodighiero et al. (2011) for z≈2 SFGs,

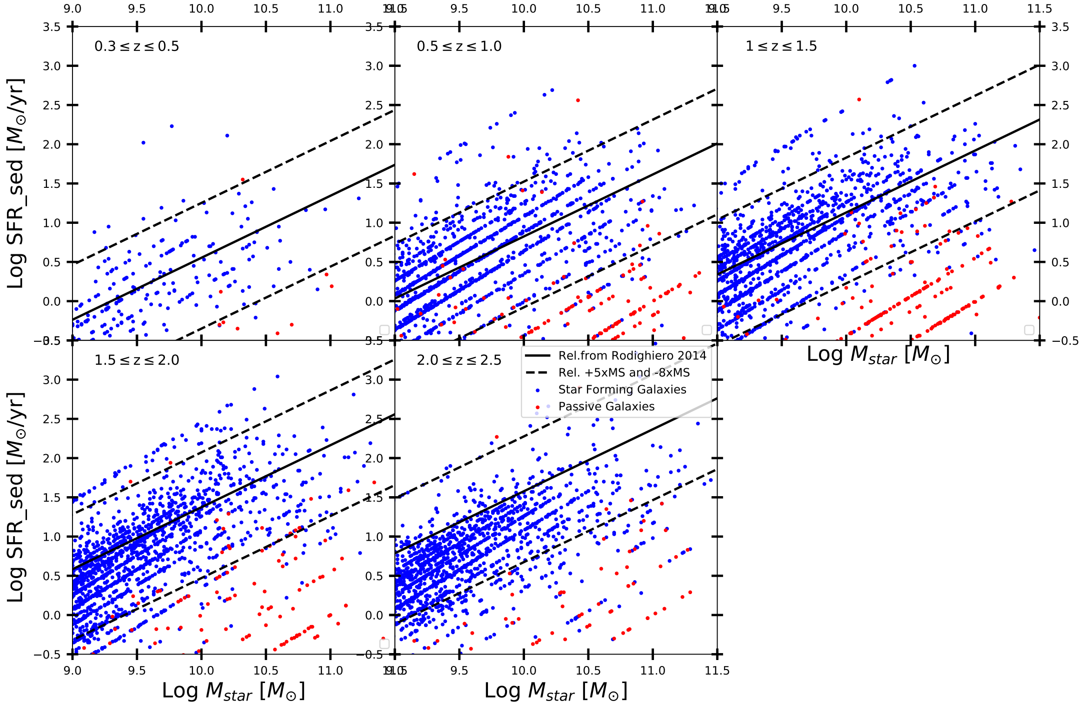

Figure 3.3 The SFR versus total mass diagram. The black line is the normalization of the Main Sequence from Rodighiero et al. (2011) and the dashed line indicated a limit with a SFR 8x lower than the normalization, indicating potential Passive galaxies. The SFR(SED) indicated in this plot has been retrieved from SED-fitting. The sources are all extracted from the B19 catalog.

as follows :

$$log\left(\frac{SFR}{M_\odot/yr^{\text{-}1}}\right) = -6.42 + 0.79 * log10\left(\frac{M_\star}{M_\odot}\right) \tag{3.2}$$

We then make use of the redshift dependence of the specific Star Formation Rate (sSFR) scaling like:

$$sSFR(z) = sSFR(z=0) * (1+z)^{2.8} \tag{3.3}$$

where sSFR(z=0) is the sSFR at z=0 (Sargent et al., 2014). We obtain a redshift dependent relation as follows:

$$log(SFR(z_{bin})) = log(SFR(z=2)) - 2.8 * log(1+2) + 2.8 * log(1+z_{bin}) \tag{3.4}$$

On the figure 3.3, the black line is the normalization and the dashed line identifies the galaxies with a Star Formation Rate (SFR) 8 times lower than the normalization of the MS from Rodighiero et al. (2011).

We also present in figure 3.4 further characterization of the sample. At the top on the figure, the Mass-size relation when the size (Re) is the galaxy semi-major axis and the solid black lines are the fit derived by Van Der Wel et al. (2014) for the whole CANDELS sample. At the bottom, we present the reddening versus the mass. We identify on both plots the Passive and Active galaxies following the UVJ-diagam identification (Williams et al., 2009). All the sources are extracted from the B19 catalog. As previously mentioned, we separate the sources in redshift bins, for readability and comparison with literature.

3.3 Morphological parameters for the GOODS-N field

Morphological parameters are required by the Euclid spectroscopic simulator to produce a simulated image of each galaxy with a realistic surface brightness distribution, used to reproduce the euclidized 2D spectrum. In particular the required morphological input parameters are: 1) the bulge-to-total mass fraction (Bulge$_{\text{frac}}$), 2) the bulge half-light semi-major axis

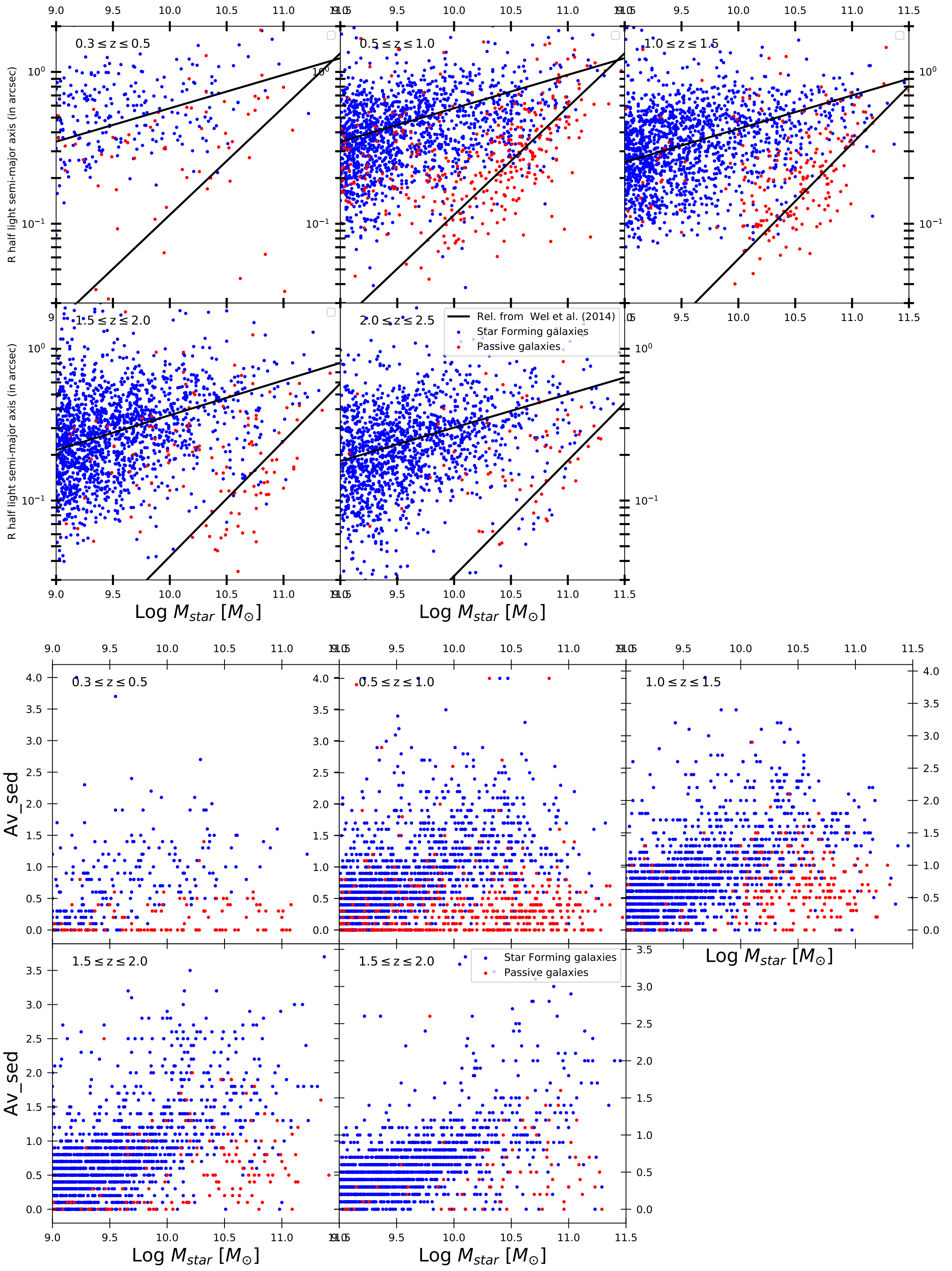

Figure 3.4 Top: the Mass-size relation where the size (Re) is the galaxy semi-major axis and the solid black lines are the fit derived by Van Der Wel et al. (2014). Bottom: The plots of the reddening versus the mass. We identify on both plots the Passive and Active galaxies following the UVJ-diagam identification (Williams et al., 2009). We separate the sources in redshift bins, for readability and comparison with literature. All the sources are extracted from the B19 catalog.

($\mathrm{Bulge}_{\mathrm{length}}$), 3) the disk scale length[2] ($\mathrm{Disk}_{\mathrm{length}}$), 4) the disk semi-minor to semi-major axis ratio (q), and 5) the disk position angle (PA). All these parameters have been derived by Dimauro et al. (2018) for the sources in the GOODS-N field.

---

[2] We recall here that the relation between the scale length, R_h, and the half-light semi-major axis, R_e, for an exponential disk is is R_h=$\mathrm{R}_e/1.678$.

Chapter Four

Construction of the incident spectra: an observational approach

We present in this chapter the procedure we apply to construct the incident Spectral Energy Distribution (SED) to be fed to the Euclid NISP-S simulator. The construction of the SEDs includes the generation of the continuum, starting from the broad-band photometric data of real galaxies (see section 4.1), as well as the addition of the nebular emission lines expected to be observed by the NISP spectrometer (see section 4.2).

Section 4.3 details the procedure used to add the emission lines to the spectral continuum, and to account for the galaxy velocity dispersion, which has the effect of broadening the spectra.

In this study, we assume a ΛCDM cosmology with Ω_{m}=0.3, Ω_{Λ}=0.7, and H_0=70 km s^{-1} Mpc^{-1}. Except if stated otherwise, we adopt all over this work the extinction curve from Calzetti (1994; 2000) and the parametrization of the Initial Mass Function (IMF) by Chabrier (2003). All magnitudes are expressed in the AB system.

4.1 Spectral continuum

4.1.1 Rest-frame continuum from observational data

The starting point in the construction of the simulated SED is to derive the continuum for each galaxy making use of available observed data. In this section we present the procedure to generate synthetic continuum using the synthesis code (GALAXEV) by Bruzual and Charlot (2003). This code enables us to compute the spectral evolution of stellar populations, in wide ranges of ages and metallicities, and to derive synthetic spectra with both low and high resolution (lr, and hr) across the whole wavelength range from 91Å to 160μm. Among those available, we use the high-resolution templates from the STELIB spectroscopic stellar library (LeBorgne et al., 2003), consisting in an homogeneous library of 249 stellar spectra in the visible range (3,200Å to 9,500Å).

We describe below the different adjustable inputs that we are considering. We make use of the physical parameters of galaxies retrieved from the available data derived and presented in the two catalogs mentioned above B19 and L16, see table 3). From both catalogs, we take the parameters calculated using the LePhare SED-fitting software (Arnouts et al., 2002; Arnouts and Ilbert, 2011). These parameters are the SFR, H$_{AB}$, $M_\star$, SFR, AV, Age and SFH. We assume a solar metallicity (m62), and the following parametrization by Chabrier (2003) for the IMF (because this was used to derive the SED fitting results in the adopted catalogs):

$$\phi(log\ \ m) \propto \begin{cases} exp\left[-\frac{(log\ \ m - log\ \ m_c)^2}{2\sigma^2}\right], & if \quad m \leq 1M_\odot \\ m^{-1.3} \quad , & if \quad m > 1M_\odot \end{cases} \tag{4.1}$$

Where $m_c = 0.08M_\odot$ and $\sigma = 0.69$

These templates are provided in the rest-frame and in the air with a spectral resolution

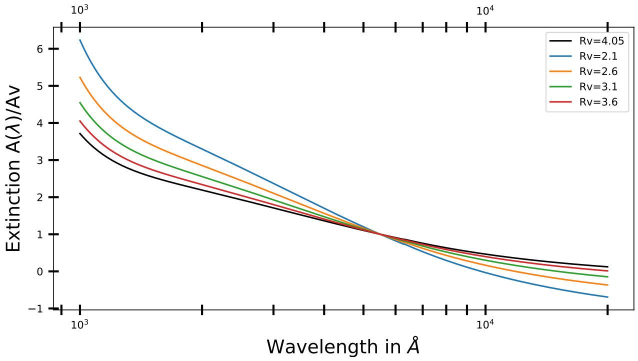

Figure 4.1 The wavelength dependent curve of the extinction coefficient using the law provided by Calzetti et al., 2000. We show the resulting curve with different values for the ratio of total to selective extinction $R_V = A_V/E(B-V)$.

(FWHM) of 3Å.

4.1.2 Transformation to the observed frame

We present in this section the procedure that we apply to transform the templates from the rest- to the observed frame, and the wavelengths from air to vacuum.

We need to redshift the wavelength and fluxes, and eventually correct fluxes for reddening. Wavelengths are redshifted using the well-known relation:

$$\lambda_{obs} = \lambda_{rest} * (z + 1) \tag{4.2}$$

Where the redshift *z* is provided in the catalogs presented in section 3.

We then convert the wavelengths from air to vacuum using the following recipe, proposed by Morton (2000) and applied in the Python package *airvacuum.py*:

by defining:

$$s = \frac{1e4}{\lambda_{air}}, \tag{4.3}$$

$$n = 1 + 0.00008336624212083 + \frac{0.02408926869968}{130.1065924522 - s^2} + \frac{0.0001599740894897}{38.92568793293 - s^2} \tag{4.4}$$

$$\lambda_{vacuum} = \lambda_{air} * n \tag{4.5}$$

The Software GALAXEV provides templates in units of total luminosity per unit of total Mass (in solar masses $M_\odot$). To obtain the flux in erg cm^{-2} s^{-1} Å^{-1}, we multiply by the total Mass, and convert the luminosity into flux using the luminosity distance (d_L) derived from the redshift using the Python *luminosity.distance* function, which is part of the *astropy.cosmology package*.

$$F_\lambda^{\ int}[erg\ s^{-1}cm^{-2}\text{Å}^{-1}] = \frac{L_\lambda * M_\star}{(4 * \pi * d_L^2)}.\frac{1}{(1+z)} \tag{4.6}$$

The total Mass, $M_\star$, and the redshift (z) in Equation 4.6 are those provided in observational catalogs extensively described above. The (1+z) term at the denominator accounts for the fact that the flux and luminosity are not bolometric but densities per unit wavelength (Hogg et al., 2002).

4.1.3 Extinction correction

We finally apply the Calzetti et al. (2000) extinction law to convert the intrinsic flux ($F_\lambda^{\ int}$) derived in Equation 4.6 into the observed, extinction-corrected flux ($F_\lambda^{\ corr}$), as follows:

$$F_\lambda^{\ corr}[erg\ s^{-1}cm^{-2}\text{Å}^{-1}] = F_\lambda^{\ int} * 10^{-0.4.A_\lambda} \tag{4.7}$$

where the dust extinction is taken into account with:

$$A_\lambda = k_\lambda.E_{star}(B-V) \tag{4.8}$$

Here $E_{star}(B-V)$ is the color excess taken from the catalogs B19 and L16, and k_λ is the wavelength dependent 2000 extinction curve, with a normalization factor of R_V=4.05 (see figure 4.1), that we retrieve using the Python function *extinction.calzetti00*. We now have built models of SEDs for galaxies in the observation frame at a redshift between 0.3 and 2.5. The next section will go through the calculation of the emission lines to be added to these models.

	Emission lines	Wavelength [Å]
Balmer lines	Hα	6,564.61
	Hβ	4,862.69
	Hγ	4,341.69
	Hδ	4,102.92
	Hϵ	3,971.19
	H8	3,890.15
	H9	3,836.48
	H10	3,798.98
	H11	3,771.70
	H12	3,751.22
Paschen Lines	Pβ	12,821.59
	Pγ	10,941.09
	Pδ	10,052.13
	P8	9,548.59
	P9	9,231.55
	P10	9,017.39
[NII]	[NII]λ6584	6,585.23
	[NII]λ6549	6,549.84
[OIII]	[OIII]λ5008	5,008.24
	[OIII]λ4959	4,960.30
[OII]	[OII]$\lambda\lambda$3727,3729	3728.49
[SII]	[SII]λ6731	6,732.71
	[SII]λ6717	6,718.32
[SIII]	[SIII]λ9531	9,533.20
	[SIII]λ9069	9,071.10

Table 4.1 List of the emission lines in vacuum to be added to the continuum. We will calculate predicted fluxes for all these emission lines.

4.2 Calculation of fluxes for nebular emission lines

We present in this section the procedures we apply to predict the fluxes of the photoionized allowed lines Hα, Hβ, Hγ, Hδ, Hϵ, H8, H9, H10, H11, H12 (Balmer lines), Pβ, Pγ, Pδ, P8, P9, P10 (Paschen lines), and of the collision excited forbidden lines [NII]λ6584, [NII]λ6549, [OIII]λ5008, [OIII]λ4959, [OII]$\lambda\lambda$3727,3729, [SII]λ6731, [SII]λ6717, [SIII]λ9531, [SIII]λ9069. We start from the broad-band SED fitting results of the samples presented above, then using empirical relations based, and calibrated, on observational results from the literature. We will proceed in a step by step building process, where some of the values calculated are used in the following calculations. We present the prediction for the different line fluxes following this approach, starting from Hα until the determination of the [SIII] doublet fluxes.

The collisionally excited forbidden emission-lines provide key diagnostics of the gas-phase chemical abundance, the ionization state of the gas, the dust extinction, and the ionizing power source in the galaxy so having been of great interest for several studies over the past decades. This has led astronomers to establish and calibrate several relations between the above mentioned physical properties of the galaxies and their observed emission lines. In the following, we present the results for some of these calibrations, which enable us to predict fluxes for emission lines of our interest.

We will also use spectroscopic observational data to evaluate and potentially calibrate our results. Indeed, for the samples presented above, from the GOODS-N and COSMOS fields, spectroscopic data are available in the literature for some of the nebular lines calculated in this work. This allows a useful comparison and fine-tuning of our calculated fluxes, based on the observed emission line fluxes for the same galaxies. This comparison is a key aspect in our choice to construct templates starting from catalogs of real galaxies.

4.2.1 Hα and [OII]$\lambda\lambda$3727,3729 fluxes from the Star Formation Rate

The Star Formation Rate

The study of the Star Formation Rate (SFR) is of particular interest in astrophysics. It enables us to trace the Star Formation History (SFH), giving vital clues of the physical nature of the Hubble sequence and evolutionary histories of galaxies. The SFR has therefore been largely studied in the literature (Roberts, 1969; Larson and Tinsley, 1977; Kennicutt, 1998; Daddi et al., 2004, 2007; Rodighiero et al., 2011, 2014).

A way to study the SFR is to look for young stars. The young and massive O- and B-type stars are significant indicators when trying to reveal the presence of young stars, due to both their high luminosity and short lifetime enabling a relatively accurate age determination. Nevertheless, except in the closest galaxies, individual O- and B- stars are unresolved even with the advent of high resolution space telescopes such as the *HST*. We will therefore evaluate the stellar activity studying the effects of their presence using indirect methods.

The O- and B- stars, indicators of the SFR, can be traced in different ways as reviewed by Kennicutt (1998) and well presented in Madau and Dickinson (2014). For example it can be retrieved by integrated light measurement in the Ultraviolet (UV) and far-infrared (FIR), SED-fitting method or by tracking and measuring nebular recombination lines' fluxes.

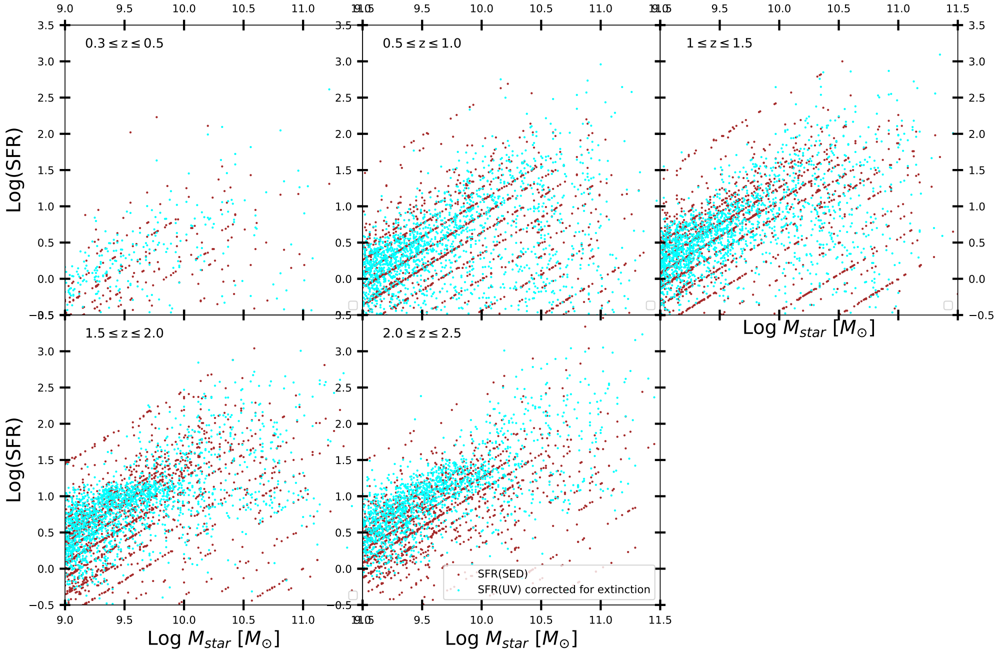

Figure 4.2 Comparison of the Main Sequence obtained using the SFR obtained form the UV photometric measurement (SFR(UV)) with the SFR obtained form SED-fitting (SFR(SED)). We found a good agreement between the two SFRs, and therefore we choose to work with the SFR(SED) for consistency with the construction of the continuum. This data has been extracted from B19, sampling the GOODS-N field.

Indeed, O- and B- stars will leave some specific signatures in the SED. It can be from their photosphere direct contribution to the UV emission (see Donas and Deharveng, 1984), or indirect contributions, such as the one in the IR resulting from the energy that dust absorbs from the UV and re-radiates at MIR and FIR wavelengths (see Rieke and Lobofsky, 1979).

Another indirect contribution comes from the nebular emission lines. Excited and ionized gas by energetic photon coming from the O- and B- stars in HII regions will present emission lines resulting from the following recombination (Madau and Dickinson, 2014). Indeed, only massive young stars (i.e. $M_\star \geq 10M_\odot$ and Age≤20My) contribute significantly to the integrated ionizing flux, such that the photoionized emission lines (in particular Hα) provide a nearly instantaneous measure of the SFR, independently of the star formation history (Kennicutt, 1998).

The possibility to link the SFR to different measurable quantities makes it a powerful and robust indicator, enabling definition of well-established calibrations. SFRs obtained applying different calibrations and at different redshift bins are showing consistent results. For example Daddi et al. (2007) have shown, using multi-wavelength data from the GOODS-N field, a good agreement between SFRs calculated from radio, far-IR, mid-IR and even UV (corrected for the extinction by dust). More recently, this consistency has been presented by Sanders et al. (2019) comparing the SFR from [OII] (SFR(OII)) and Hα (SFR(Hα) nebular lines, and by Kashino et al. (2013) comparing the SFR(UV) with SFR(Hα).

In this study, in particular, we will make use of this proved agreement, using the SFR obtained from the SED-fitting method (SFR(SED)), retrieved from the LePhare SED-fitting software (Arnouts et al., 2002; Arnouts and Ilbert, 2011), to predict the Hα fluxes. Indeed, after verifying the agreement with the SFR derived from the UV photometric measurement (SFR(UV)) (see figure 4.2), we choose to work with the SFR(SED), for consistency with the other SED-fitting parameters used to construct the spectral continuum (see section 4.1).

Calculated intrinsic Hα fluxes

Historically, Hα has been one of the favorite emission lines for astronomers, particularly for redshift determination. The abundance of Hydrogen in the Universe and the relative strength of the line made Hα an ideal indicator to study galaxies' physical properties and for redshift determination. In particular, Hα has been recognized to be the most reliable of the easily accessible nebular SFR tracers even in the highly obscured star-forming galaxies (Kennicutt, 1998; Moustakas, Kennicutt, and Tremonti, 2006).

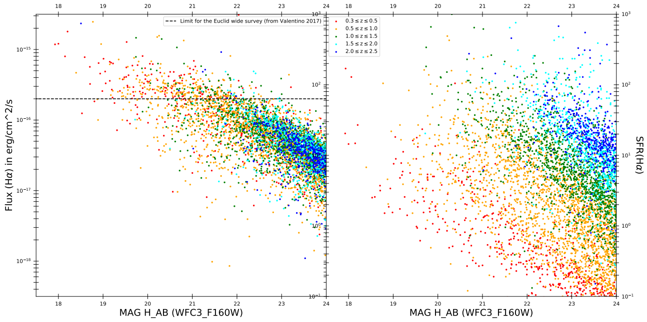

Figure 4.3 The magnitude H in the AB system and the H_alpha *flux calculated as a function of mass. The sources have been extracted from the B19 catalog.*

Referring to previous studies (Kennicut, Tamblyn, and Congdon, 1994; Madau, Pozzetti, and Dickinson, 1998), Kennicutt(1998) presented a calibration between the intrinsic Hα luminosity (L(Hα) from which we will start our flux calculations.

Kennicutt used a Salpeter (1955) IMF. We applied a "correction" dividing by a factor 1.7 to transform the calibration for the use of Chabrier (2003) IMF as presented by Kashino et al. (2019).

We then obtain the relation:

$$L(H\alpha)[erg\ s^{\text{-1}}] = \frac{SFR[M_\odot\ yr^{\text{-1}}]}{4.6.10^{\text{-42}}} \tag{4.9}$$

Where $SFR[M_\odot\ yr^{\text{-1}}]$ takes the value retrieved from the SED-fitting and presented in the catalogs of real galaxies.

We convert the luminosity obtained from the equation 4.9 into the intrinsic calculated flux for Hα, $F^{\,int}_{\,calc}(H\alpha)$, using the *distance.luminosity* function ($\mathrm{d_L(z)}$) as follow :

$$F^{\,int}_{\,calc}(H\alpha)[erg\ s^{\text{-1}}cm^{\text{-2}}] = \frac{L(H\alpha)}{4\pi d_{\mathrm{L}}(z)^2} \tag{4.10}$$

The well-established calibration of the SFR with Hα led us to choose this relation to start determining the emission lines, and is therefore a key aspect of our study, leading by a step-by-step procedure described below to the calculation of Hβ, [NII], [OIII], [SII] and [SIII] fluxes. This approach may face some uncertainties and limitations, but the amount of well-established data available to challenge and calibrate our final results (see section 5.1)

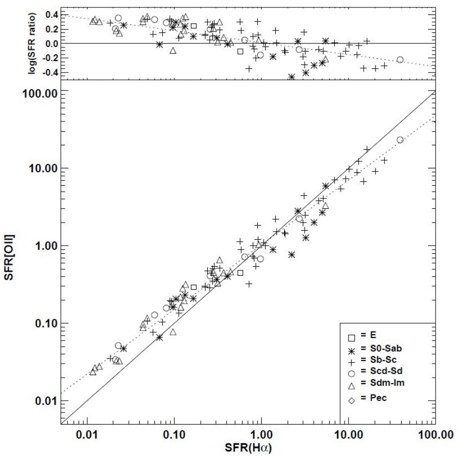

Figure 4.4 A comparison between the Hα and [OII] SFRs made by Kewley, Geller, and Jansen (2004) and based on Kennicutt (1998) calibrations.

presents a quite promising perspective in order to draw and cover a realistic and complete sample of galaxies' spectra to be simulated.

Calculated intrinsic [OII]$\lambda\lambda$3727,3729 fluxes

The strongest emission feature in the blue is the [OII]$\lambda\lambda$3727,3729 forbidden-line doublet and is extremely useful for lookback studies of distant galaxies, because [OII] can be observed in the visible out to redshifts $z \approx 1.6$. The luminosities of forbidden lines are not directly coupled to the ionizing luminosity, and their excitation is sensitive to abundance and ionization state of the gas. However, the excitation of [OII] is sufficiently well behaved that it can be calibrated empirically as a quantitative SFR tracer (Kewley, Geller, and Jansen, 2004). We present in figure 4.4, a comparison between the Hα and [OII] SFRs made by Kewley, Geller, and Jansen (2004) and based on Kennicutt (1998) calibrations.

In a similar way as for the Hα line, the strong emission line [OII]$\lambda\lambda$3727,3729 has also been used as an SFR tracer (Kennicutt, 1998; Kewley, Geller, and Jansen, 2004). Even if this calibration suffers from a dependence on secondary parameters such as the metal abundance, it remains in first approximation a reliable tracer of the current SFR (Kewley, Geller, and Jansen, 2004). We use the calibration presented in the Equation 4 of Kewley, Geller, and Jansen (2004), that has been derived from two samples of galaxies located at high-redshift, e.g., one at $0.8 \leq z \leq 1.6$, from the NICMOS Hα survey, and the other at $0.5 \leq z \leq 1.1$, from the Canada-France Redshift Survey. The calibration is presented as follows:

$$SFR([OII])[M_{\odot}\ yr^{-1}] = 6.58 \times 10^{-42} L([OII])[erg\ s^{-1}] \tag{4.11}$$

Where SFR([OII]) is in agreement with the SFR obtained from Hα (Kewley, Geller, and Jansen, 2004, eq.5). We therefore use the same SFR that we have used to calculate L(Hα), which is the SFR obtained from the SED-fitting (see section 4.2.1).

4.2.2 Hβ, the Balmer and Paschen lines fluxes

We calculate the Hβ, the other Balmer lines and the Paschen lines assuming ratios between their respective intrinsic fluxes, using as a starting reference the Hα calculated in section 4.2.1. We make use of the ratio presented by Hummer and Storey (1987) and Osterbrock (1989). We indicate these ratios in the table 4.2. These lines theoretically also directly trace the SFR but being relatively faint, they are rather difficult to be detected compared to Hα, and other forbidden lines (e.g. [OII], [OIII]). They can still be powerful to validate redshift determination.

Calculation of the predicted $F^{int}_{calc}(H\beta)$ ***flux from*** $F^{int}_{calc}(H\alpha)$

The hydrogen Balmer decrement – Hα/Hβ - is frequently used to determine the amount of dust extinction for the low-density gas, by comparing the observed Hα/Hβ with the expected intrinsic ratio. An intrinsic value of 2.86 is generally adopted assuming typical HII region gas conditions, where the electron density Ne=10^{2}cm^{-3}, the electron temperature Te = 10^{4}K, and assuming case B recombination (see Osterbrock, 1989). We then obtain:

$$F^{int}_{calc}(H\beta)[erg\ s^{-1}cm^{-2}] = \frac{F^{int}_{calc}(H\alpha)[erg\ s^{-1}cm^{-2}]}{2.86} \tag{4.12}$$

Where F^{calc}_{int}(Hβ) is the intrinsic flux calculated for the Hβ line.

	Line	Ratio $F_{line}/F_{(H\beta)}$
Balmer lines	Hα	2.86
	Hβ	1
	Hγ	$4.68e^{-1}$
	Hδ	$2.59e^{-1}$
	Hϵ	$1.59e^{-1}$
	H8	$1.05e^{-1}$
	H9	$7.31e^{-2}$
	H10	$5.30e^{-2}$
	H11	$3.97e^{-2}$
	H12	$3.05e^{-2}$
Paschen Lines	Pβ	1.63e^{-1}
	Pγ	$9.04e^{-2}$
	Pδ	$5.55e^{-2}$
	P8	$3.66e^{-2}$
	P9	$2.54e^{-2}$
	P10	$1.84e^{-2}$

Table 4.2 Ratios extracted from Hummer and Storey (1987) between the fluxes of the lines of interest (Balmer and Paschen lines) and the flux of the Hβ line.

Calculation of Balmer and Paschen lines fluxes from F$^{int}_{calc}$(Hβ)

From the F$^{calc}_{int}$(Hβ) and referring to the table 4.2, we calculate the intrinsic fluxes for all the other Balmer and the Paschen lines. These lines are namely the Hγ, Hδ, Hϵ, H8, H9, H10, H11, H12 (Balmer), Pβ, Pγ, Pδ, P8, P9, P10 (Paschen) lines.

4.2.3 Correction for reddening of the intrinsic flux

All the calculated fluxes until now are intrinsic fluxes. We now have to account for the reddening as we did for the continuum in section 4.1. However, the extinction of nebular lines requires the introduction of a fudge factor, the so-called *f-factor*. Since the procedure to account for the extinction by dust is the same for all the lines, we here present the calculation for the Hα flux only.

$$F^{corr}_{calc}(H\alpha) = F^{int}_{calc}(H\alpha).10^{-0.4*A_{H\alpha}} \tag{4.13}$$

Where F$^{corr}_{calc}$(Hα) is the corrected calculated flux. The dust extinction is taken into account with:

$$A_{H\alpha} = k_{H\alpha}\frac{E_{star}(B-V)}{f} \tag{4.14}$$

With $\mathrm{E_{star}}$(B-V) is taken from the catalogs of real galaxies presented in section 3. We obtain the factor $\mathrm{k_{H\alpha}}$ using the wavelength dependent extinction law provided by Calzetti et al. (2000,4.05).

We are also calling out the *f-factor* to account for the difference between the $E_{\rm star}(B-V)$ of the stellar component and the $E_{\rm neb}(B-V)$ of the line-emitting nebular region. The *f-factor* is defined by $f = E_{\rm star}(B-V)/E_{\rm neb}(B-V)$.

The physical meaning of the *f-factor* is still a subject of debate. Puglisi et al., 2016 have suggested that the *f-factor* is a function of the mass and SFR of the galaxy. Moreover, the determination of the *f-factor* value is still quite complicated. Different values have been inferred ranging from 0.44 for local galaxies (Calzetti et al., 2000) to ≈ 1 in other studies (Kashino et al., 2013; Puglisi et al., 2016), and some of these differences are to be ascribed to different galaxy samples analyzed (e.g., normal SFGs vs heavily obscured starburst galaxies, etc.). In our study we use the *f-factor* = 0.58 [1] derived by Calzetti et al. (2000) for local galaxies, but proved to be a fair estimate also for high-redshift galaxies (e.g. Fõrster Schreiber et al., 2009).

4.2.4 [NII]$\lambda\lambda$6584,6549 fluxes from the Mass-Metallicity relation

The strongest line of the [NII] doublet, N[II]λ6585, can be very useful in increasing the confidence in redshift determination (Silverman et al., 2015), in estimating the gas-phase metallicity and even in yielding insight on the kinematics from the FWHM of the line.

The N[II]λ6585 line has been studied by measuring observed ratio log(F(N[II]λ6585/Hα)),

---

[1] Note that the value 0.58 is obtained when applying the Calzetti reddening curve for both the nebular and continuum extinction, while 0.44 is obtained when using the Fitzpatrick reddening curve for the continuum (cf., Puglisi et al. (2016)). In our case we apply the Calzetti reddening curve for both the continuum and nebular continuum. We thus chose 0.58 for the *f-factor*

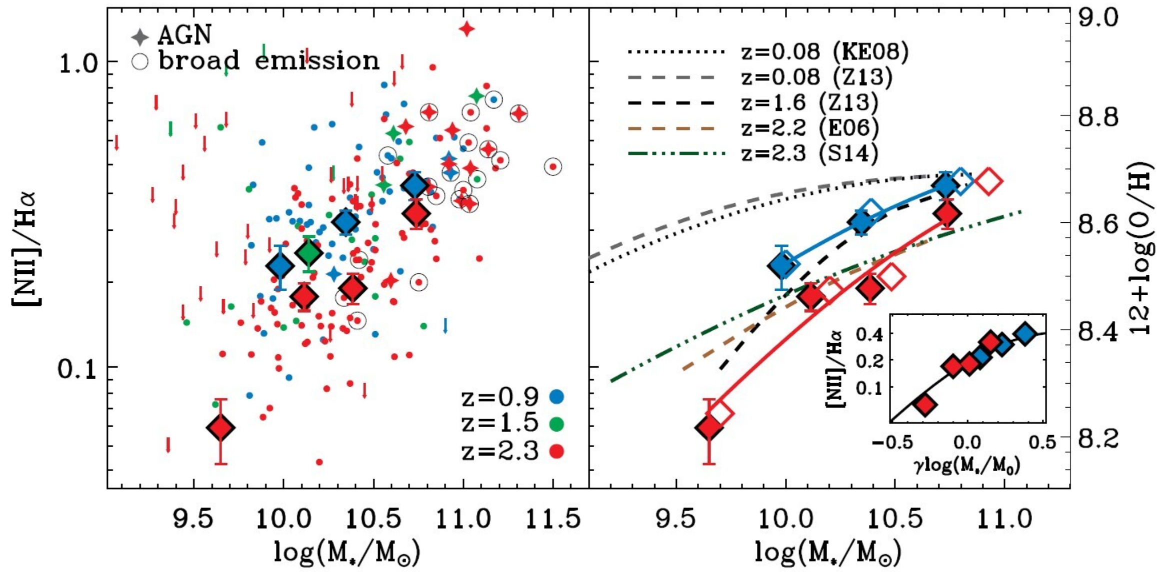

Figure 4.5 The MZR and its evolution with redshift as presented by Wuyts et al. (2014).

often mentioned in literature as N_2. The N_2 ratio is highly sensitive to the metallicity which is measured by the oxygen abundance (O/H) (Denicolo, Terlevich, and Terlevich, 2002). This relation is the result of a tendency for the ionization to increase as the (O/H) decreases below the solar ratio and the subsequently decreasing of the ratio F([NII])/F(N[III]) together with the (N/O) (Henry, Edmunds, and Koppen, 2001). The metallicity studies at high redshift, and mostly in the previously mentioned *redshift desert*, have been particularly critical due to small samples and difficulties related to the NIR spectroscopy (e.g., strong atmospheric absorption from the ground). However a certain number of studies have been performed even across the *redshift desert*, in particular where the emission lines of interest such as Hα, [NII], Hβ or [OIII] fall in the near-IR atmospheric windows, enabling ground-based spectroscopy. So far, it has been possible to study Hα and [NII] in thousands of galaxies all the way to $z \approx 2.5$ (reaching the K band limit) such that the N_2 index offers a great way to determine metallicity, and study its evolution with redshift (Steidel et al., 2014; Pettini and Pagel, 2004). It will be of particular interest to extend the study of metallicity to the huge sample of bright star-forming galaxies using the forthcoming Euclid data.

We present in this section, the recipe derived from the mass-metallicity relation (MZR) that we apply to determine the flux of the [NII] doublet lines. We use the empirical relation proposed by Wuyts et al. (2014), based on the observations of a sample of 222 galaxies at $0.8 \leq z \leq 2.6$ and $\log(M_\star/M_\odot)$ in the range [9.0 - 11.5]. They observed the Hα and [NII] emission lines with a combination of different near-IR spectrographs: the multi-object LUCI spectrograph at the Large Binocular Telescope (LBT), in Arizona, and the SINFONI, and the KMOS integral field Units (IFU) at the Very Large Telescope (VLT), in Chile. Galaxies in their sample are located in the COSMOS, GOODS-South North-deep, UDS deep or in the Q2343 field (see Wuyts et al., 2014 for further details). Based on the parametrization originally proposed by Zahid et al. (2014), Wuyts et al. (2014) fit a redshift dependent mass-metallicity relation (MZR) over an extended redshift range ($0.8 \leq z \leq 2.6$), that we will apply to our whole studied redshift range (0.3-2.5). Wuyts et al. (2014) also showed that their MZR parametrization is in good agreement with that obtained by Zahid et al. (2014) at $0 \leq z \leq 1.6$, as well as with results for other high-z samples at z≈2.2-2.3 (Erb et al., 2006 and Steidel et al., 2014). The relation we refer to is the following:

$$12 + log(O/H) = Z_0 + log\left[1 - exp\left(- \left[\frac{M_\star}{M_0}\right]^\gamma \right)\right] \tag{4.15}$$

where Z_0=8.69± 0.01 is the asymptotic metallicity, and $\gamma = 0.40 \pm 0.01$ is the power-law slope at stellar masses $\ll M_0$. While both Z_0 and γ are found to be constant with redshift (within the errors), the characteristic turnover mass M_0 (where the relation begins to flatten) is redshift dependent. Indeed, it seems that M_0 is the only parameters significantly evolving with redshift in the MZR. The proposed interpretation of this finding is that it follows from the more fundamental universal relation between metallicity and stellar-to-gas mass ratio (Zahid et al., 2014; Wuyts et al., 2014). M_0 is then evolving with redshift as follows:

$$log(M_0/M_\odot) = (8.86 \pm 0.05) + (2.92 \pm 0.16) * log(1 + z) \tag{4.16}$$

We now need to transform the oxygen abundance 12+log(O/H) from eq.4.5 and 4.16 into a value for the ratio N_2. For this purpose, we make use of the linear metallicity calibration proposed by Pettini and Pagel (2004) based on 137 extragalactic HII regions with well determined values of (O/H) and N_2 . The calibration, S-shaped in the all sample, happens to be linear when $8.2 \leq 12 + \log(O/H) \leq 8.66$, where 8.66 refers to the solar oxygen abundance (Asplund et al., 2004). The linear calibration is then presented as follows:

$$12 + log(O/H) = 8.90 + 0.57 * N_2 \tag{4.17}$$

The scatter of this relation for local galaxies is sigma=0.18 dex. However, to reproduce a plausible distribution of higher redshift galaxies in the N_2-$M_\star$ plane, in this work we use the intrinsic scatter on N_2 inferred by Kashino et al. (2019) on the FMOS-COSMOS survey sample, at $1.43 \leq z \leq 1.74$, which has been shown to be very consistent with that derived for a sample of SDSS local galaxies. The intrinsic scatter $\sigma_{int}(N_2)$, is derived as a function of $N_2(M_\star)$ (i.e., the best-fit $M_\star$–[N II]/Hα relation at a given $M_\star$) as defined by the eq. 20 of their paper:

$$\sigma_{int}(N_2) = 0.299 + 0.807 * N_2(M_\star) + 0.856 * N_2(M_\star)^2 \tag{4.18}$$

This sigma is applied calling out the Gaussian distribution provided by the Python function *numpy-random-normal*. Unless stated otherwise, this Python function will always be used in this work to apply a normally distributed scatter on our calculated values.

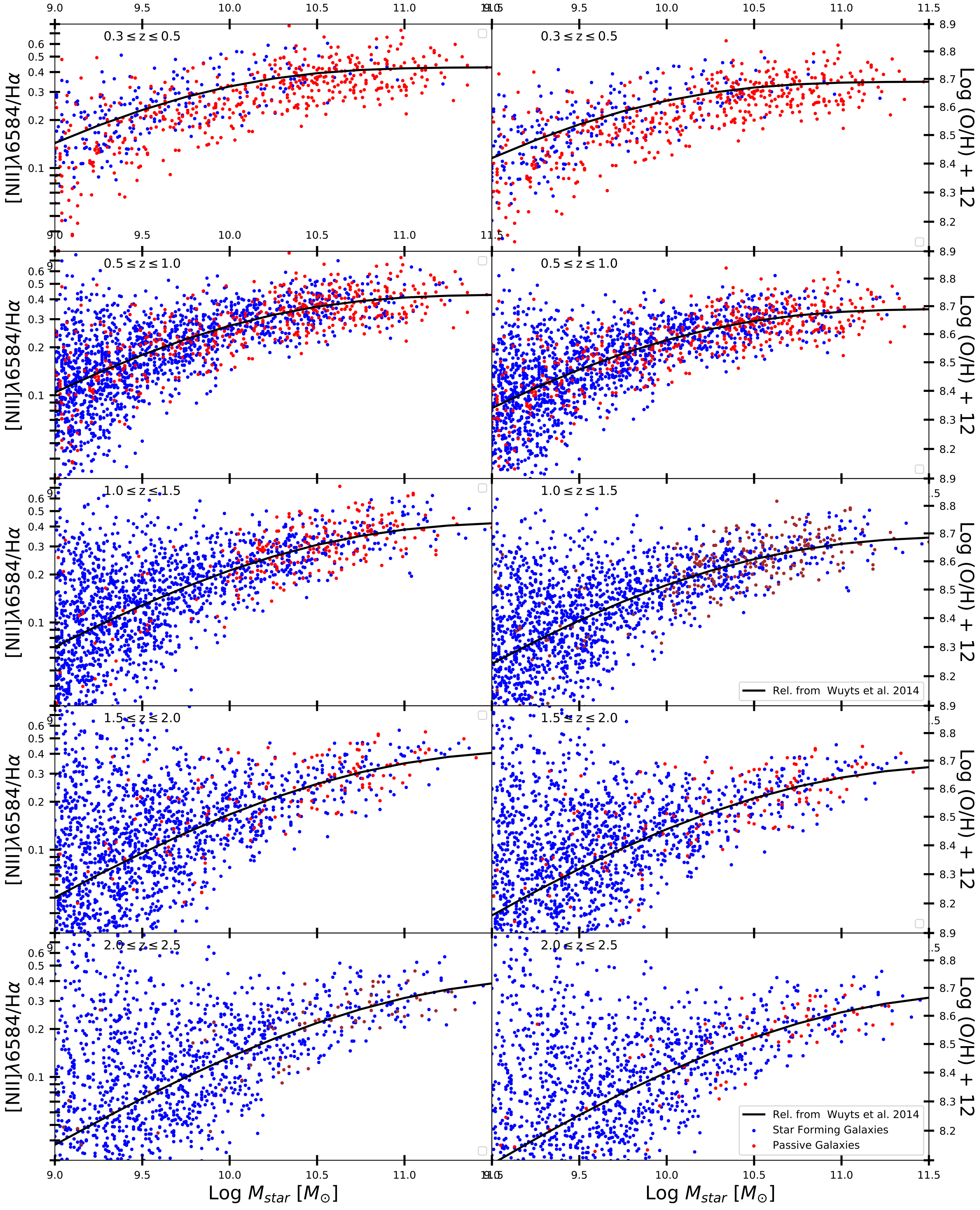

Figure 4.6 Calculated mass-metallicity relation for galaxies extracted from the B19 catalog following the calibrations provided by Wuyts et al. (2014) and adding a normally distributed scatter as detailed in the text. The red and blue points respectively refer to galaxies identified as Passive and Active galaxies from the UVJ-diagram discrimination rules presented by Williams et al. (2009).

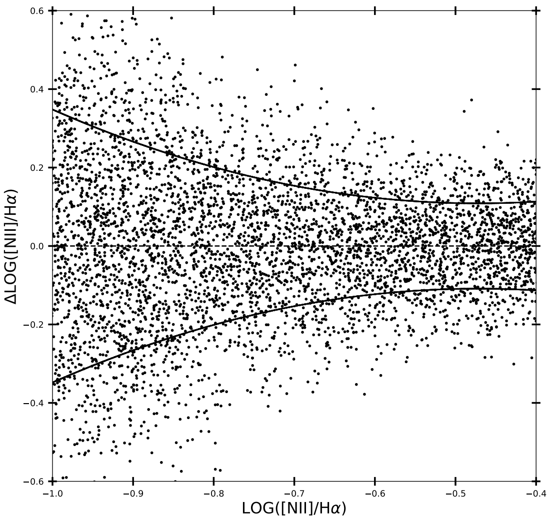

Figure 4.7 Scatter of the ratio N_2 for galaxies from the B19 catalog using the relation derived by Kashino and Inoue (2018)

From this scattered calculated ratio N_2 (see figure 4.7), we infer for each galaxy in our sample the flux for the emission line [NII]λ6584, knowing the (previously calculated) flux of the Hα line. We recall here that the two lines suffer from the same extinction from dust, such that we can use the value obtained for the corrected value for the Hα flux to obtain the corrected calculated flux for the [NII]λ6584 lines such that:

$$F^{corr}_{calc}([NII]\lambda6584) = 10^{N_2} * F^{corr}_{calc}(H\alpha) \tag{4.19}$$

The MZR and the derived N_2 ratio for our B19 sample galaxies are shown in figure 4.6.

We calculated the flux of the other line of the [NII] doublet, namely [NII]λ6549, using the F([NII]λ6584)/F([NII]λ6549) ratio presented by Acker et al. (1989) such that:

$$F^{corr}_{calc}([NII]\lambda6549) = \frac{F^{corr}_{calc}([NII]\lambda6584)}{2.95} \tag{4.20}$$

4.2.5 [OIII]$\lambda\lambda 4959, 5008$ and [SII]$\lambda\lambda$6717,6731 fluxes from the BPT diagram

The BPT diagram

The Baldwin-Phillips-Terlevich (BPT) diagram, introduced by Baldwin, Phillips, and Terlevich (1981), is a powerful tool to infer physical properties of emission-line galaxies. It consists in comparing ratios of emission lines' fluxes. These ratios are chosen considering few aspects described by Veilleux and Osterbrock (1987) as follows:

1. one of the line should be strong and accessible from common spectroscopic survey
2. badly blended lines should be avoided, to limit uncertainty coming from the deblending procedure
3. the wavelength separation between the two lines should be small enough to mitigate variation of reddening and flux calibration
4. a preference is given to ratio involving Hydrogen Balmer lines, known to be abundance-sensitive.

For example, the ratios N_2 and O_3 [2] both satisfy all of these conditions and have therefore been subject of interest in several studies over the last decades (Veilleux and Osterbrock, 1987; Kewley et al., 2013b).

The BPT diagram of N_2 versus O_3 ratios (Referred as the N_2-BPT diagram) happens to be a particular efficient tool in discriminating the dominant excitation mechanism of nebular emission in galaxies, providing a clear visual separation of galaxies whose spectra are dominated by ionization induced by young stars' UV radiation field from those essentially ionized by AGN. This interesting feature led astronomers to extensively study this BPT diagram for AGN classification schemes based on observation and photoionization model, stellar population synthesis and shock modelling (Osterbrock and Podge, 1985; Veilleux and

---

[2] O_3 hereafter refers to $\log(\mathrm{F}([\mathrm{OIII}]\lambda 5008/\mathrm{H}\beta))$

Osterbrock, 1987; Kewley et al., 2001; Kewley et al., 2013b). Indeed, star-forming galaxies form a tight sequence in the N_2-O_3 plane.

The physical explanation for this differentiation comes from the extreme ultra-violet (EUV) "hard" radiation field from the accretion disk of an AGN which ionizes the [OIII] and [NII] lines, producing larger [OIII]/Hβ and [NII]/Hα line ratios than usually seen in star-forming galaxies (Kewley et al., 2013b).

Derivation of the [OIII]$\lambda\lambda$5008,4959 fluxes

The study of the emission line [OIII]λ5008 is crucial to determine the oxygen enrichment of the Interstellar Medium (ISM) (Zahid et al., 2014) as well as to identify the presence of an AGN in the host galaxy (Kewley et al., 2013a,b; Kartaltepe et al., 2015).

During the last decades, the [OIIIλ5008] emission line study has been made through the observation of the ratio O_3 calling out the so called BPT diagram.

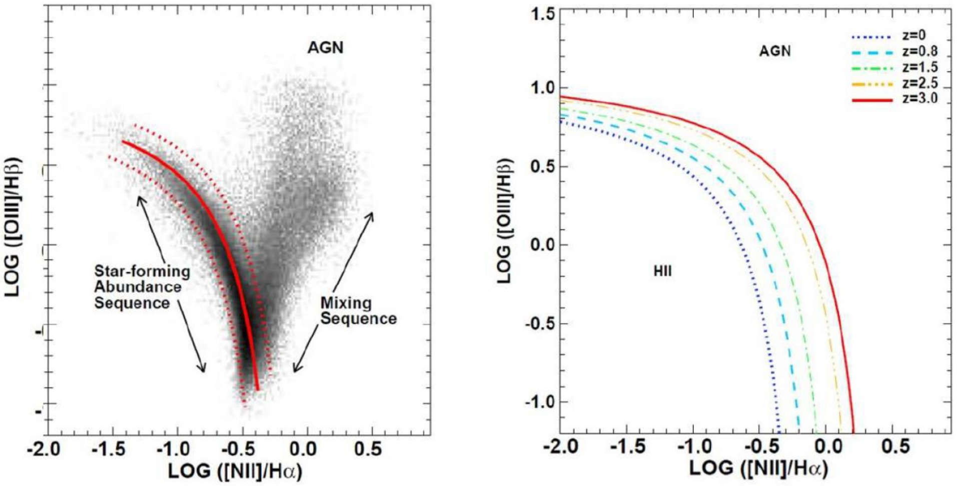

Figure 4.8 Left: The red solid curve shows the mean star-forming sequence for local galaxies. The shape of the red solid curve is defined by theoretical photoionization models, and the position is defined by the best-fit to the SDSS galaxies(Kewley et al., 2013b), with 91% of the galaxies contained with the $\pm 0.1 dex$ *dashed red curves. Right: An illustration of the effect of varying different galaxy parameters on the star-forming galaxy abundance sequence in the* N_2*-BPT diagram (extracted from Kewley et al. (2013b)].*

In our study, we assume our sample to be exclusively composed of normal star-forming galaxies, e.g. without AGN. Making this assumption enables us to make use of the calibration established for the so-called "star-forming galaxy abundance sequence" on the BPT diagram (Kewley et al., 2013b). Thus, by fixing N_2 (as calculated in section 4.15), we can predict the O_3 ratio. The calibration provided by Kewley et al. (2013b) for galaxies located at $0 \leq z \leq 3$, started from a previous study of local SDSS galaxies (Kewley et al., 2006) and was then extended towards higher redshift using the chemical evolution predictions of cosmological hydrodynamic simulations with theoretical stellar population synthesis, photoionization and shock models (see figure 4.8).

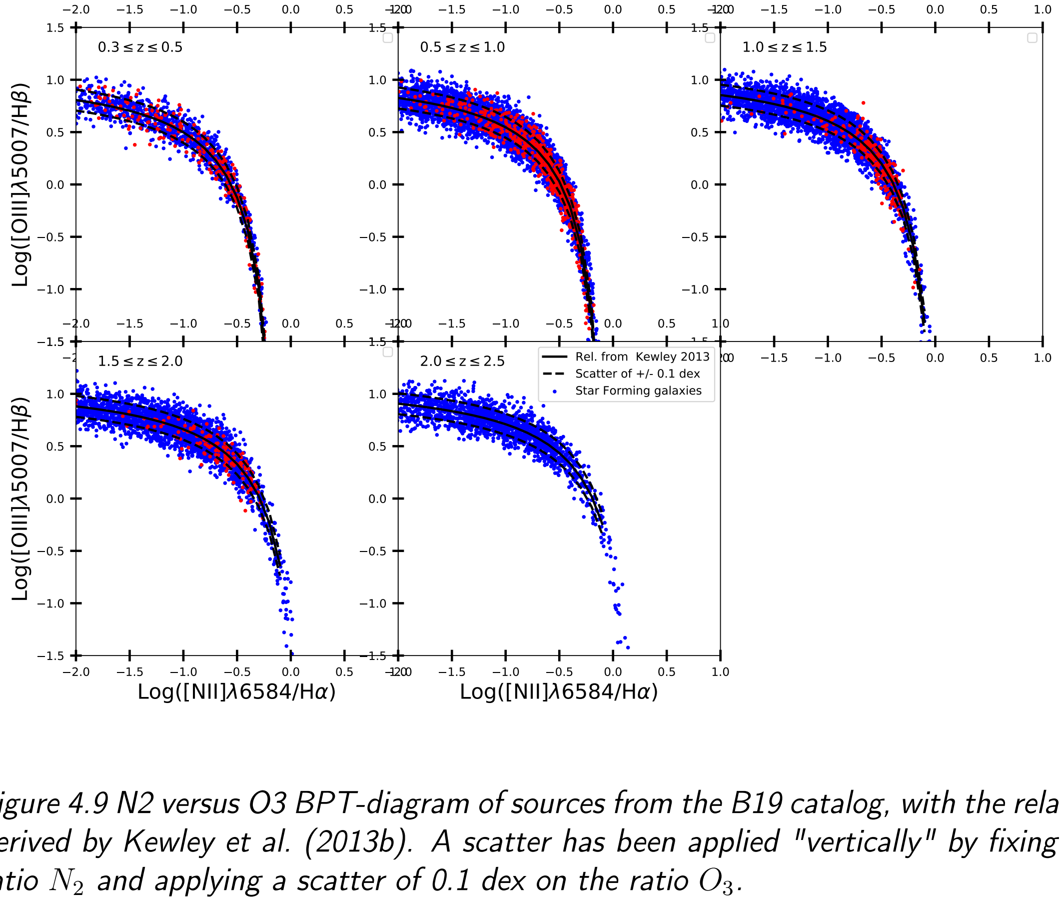

Figure 4.9 N2 versus O3 BPT-diagram of sources from the B19 catalog, with the relation derived by Kewley et al. (2013b). A scatter has been applied "vertically" by fixing the ratio N_2 and applying a scatter of 0.1 dex on the ratio O_3.

The calibration of the star-forming galaxy abundance sequence in the N_2 versus O_3 BPT diagram proposed by Kewley et al. (2013b) is presented as follows:

$$O_3 = 1.2 + 0.03 * z + \frac{0.61}{N_2 - 0.02 - 0.1833 * z} \tag{4.21}$$

This calibration is scattered on both X and Y axis by 0.1 dex as presented in figure 4.8. For our purpose, we fix the value of N_2, since a realistic scatter on N2 was already introduced by the scatter on the MZR, and therefore only keep the vertical 0.1 dex scatter that we distribute normally. We present the BPT diagram obtained with the above described method for galaxies from the B19 catalog in figure 4.9.

Then, we retrieve the other line of the [OIII] doublet, [OIII]λ4959 using the ratio presented by Dimitrijević et al. (2006) equal to 2.98 such that:

$$F\overset{corr}{\underset{calc}{}}([OIII]\lambda 4959) = \frac{F^{corr}_{calc}([OIII]\lambda 5008)}{2.98} \tag{4.22}$$

Derivation of the [SII]$\lambda\lambda$6717,6731 fluxes

An alternative BPT diagram compares the line ratios [SII]$\lambda\lambda$6717,6731/Hα and [OIII]λ5008/Hα. This BPT diagram can also be used to separate the star forming population from the AGNs (Veilleux and Osterbrock, 1987; Dopita et al., 2016; Kashino et al., 2017) even if the separation is not as clear as for the N_2-BPT diagram presented above.

We make use of the calibration for the SFGs introduced for local sources by Dopita et al. (2016) and confirmed at high-redshift by Kashino et al. (2017) (see figure 4.10), on a sample consisting of 701 star-forming galaxies with stellar masses $10^{9.6} \leq$ M$\star/M\odot\leq$ $10^{11.6}$, at 1.4 $\leq z \leq$ 1.7 (the above mentioned FMOS-COSMOS survey). The calibration is presented as follows:

$$12 + log(O/H) = 8.77 + N_2S_2 + 0.264 * N_2, \tag{4.23}$$

where N_2S_2 = log(F([NII]λ6584)/F([SII]$\lambda\lambda$6717, 6731)) and log(O/H) refers to the oxygen

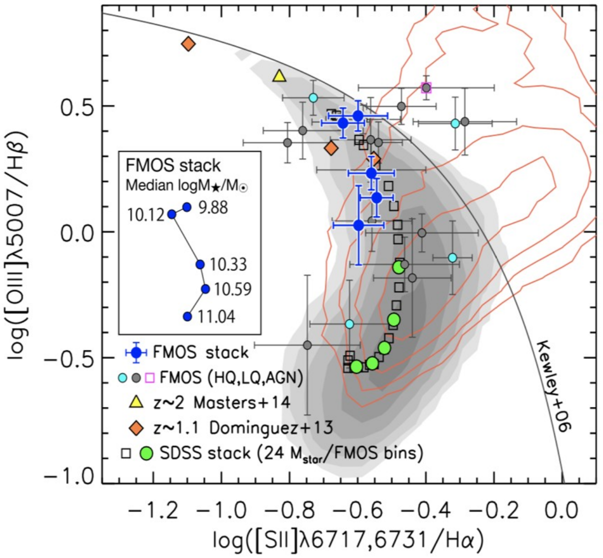

Figure 4.10 The [SII]-BPT diagram as presented by Kashino et al., 2017 for galaxies at 1.4 $\leq z \leq$ 1.7 from a sample consisting of 701 galaxies at 1.4 $\leq z \leq$ 1.7 obtained with the FMOS-COSMOS survey, representing the star-forming population over the stellar mass range $10^{9.6} \leq M\star[M\odot] \leq 10^{11.6}$.

abundance. We applied a sigma normally distributed of 0.1 dex on the value N_2S_2 calculated from equation 4.23. Resolving 4.23 we obtain the sum of the fluxes of the [SII] doublet as:

$$F_{calc}^{corr}([SII]\lambda\lambda 6717, 6731) = F_{calc}^{corr}([NII]\lambda 6584) * 10^{12+log(O/H)-8.77-0.264*N_2} \tag{4.24}$$

Nevertheless, in that case the calculation using our previous results is not so straight forward. Indeed, the relation just presented in equation 4.23 has been derived using another calibration for the transformation of N_2 into the oxygen abundance. While we used the linear calibration proposed by Pettini and Pagel (2004), Kashino et al. (2017) made use of the calibration proposed by Tremonti et al. (2004), making necessary to make some considerations before using this calibration. We describe these considerations below.

For completeness we present two methods to convert our N_2-to-(O/H) linear calibration into the one used by Kashino et al. (2017). We eventually choose one of the two methods depending on the correlation with measured fluxes obtained from observations (see section 5.1.1 for the choice of the method).

The first method consists in starting from the value of the line ratio N_2 that we have inferred in section 4.2.4 and directly convert in an oxygen abundance (O/H) as it would be obtained from the calibration made by Tremonti et al. (2004). We here make use of the eq.7 in Kashino et al. (2017) initially presented by Maiolino et al. (2008) that enabled to link the (O/H) to N_2 and presented as follows:

$$N_2 = -0.7732 + 1.2357x - 0.2811x^2 - 0.7201x^3 - 0.333x^4 \tag{4.25}$$

where x = 12 + log(O H)-8.69. This relation is nearly linear over our range of metallicity of $8 \leq 12 + \log(\mathrm{O\ H}) \leq 9$.

We make use of a grid of values to substantially cover our range of interest and subsequently obtain for each of our N_2 calculated a corresponding value for the oxygen abundance (O/H). The equation 4.24 can then be applied.

The second method consists in referring to Kewley and Ellison (2008) (eq.1 and table 3) where is presented a way to convert metallicity relations into any other calibration scheme and is formulated for our purpose as follows:

$$y = -1661.9380 + 585.17650x + -68.471750x^2 + 2.6766690x^3 \tag{4.26}$$

where y is the metallicity in 12+log(O/H) units as calibrated by Tremonti et al. (2004), and x is the original metallicity (Pettini and Pagel, 2004) to be converted, also in 12+log(O/H) units. The equation 4.24 can then be applied.

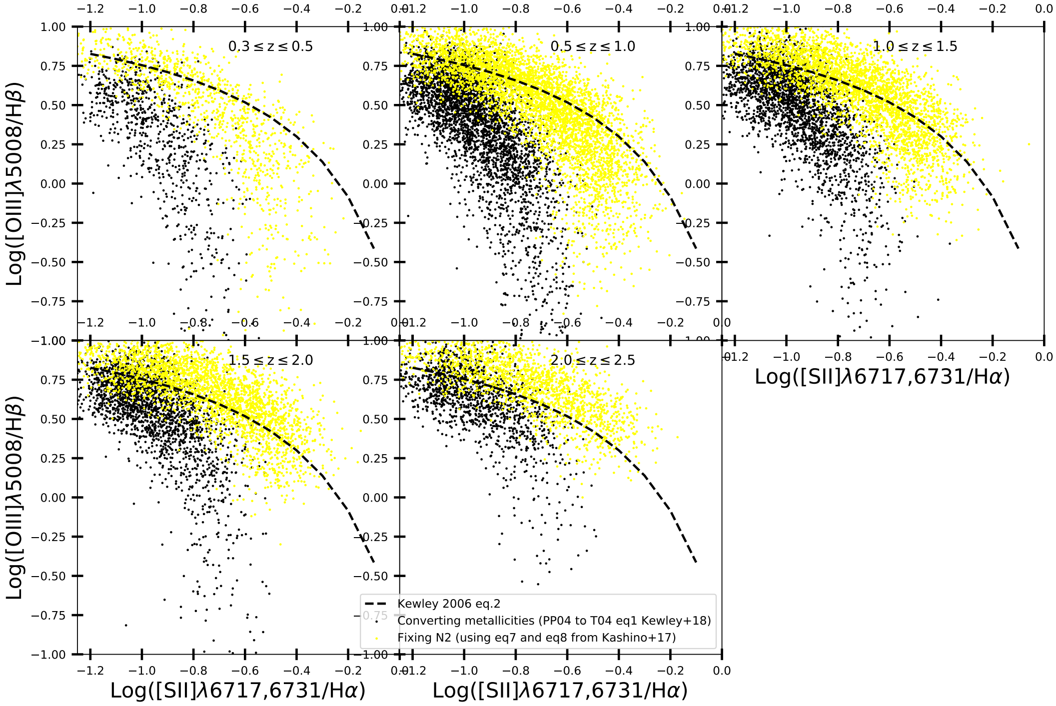

Figure 4.11 The [SII]-BPT diagram of sources from the B19 catalog, following the diagnostic presented by Kashino et al., 2017. The black points refer to the method 2 and the yellow points to results obtained with the method 1.

We will now review the procedure we applied for the determination of the ratio between the lines of the doublet [SII]$\lambda\lambda 6717, 6731$.

We will now present the ratio determination of the fluxes of the doublet [SII]$\lambda\lambda 6717, 6731$. The electron density ($n_e$) is a function of the ratio of our two forbidden lines of interest. Indeed, for a pair of lines with nearly the same excitation state, as can be an ion excited in two different states in a medium with typical low density such as in a HII region, and if both excitation states are metastable, a relation can be established between the electron density and the ratio of the lines. A relation has been derived by Proxauf, Öttl, and Kimeswenger (2014) following previous research made by Osterbrock and Ferland (2006) and is presented by Iani et al. (2019) as follows:

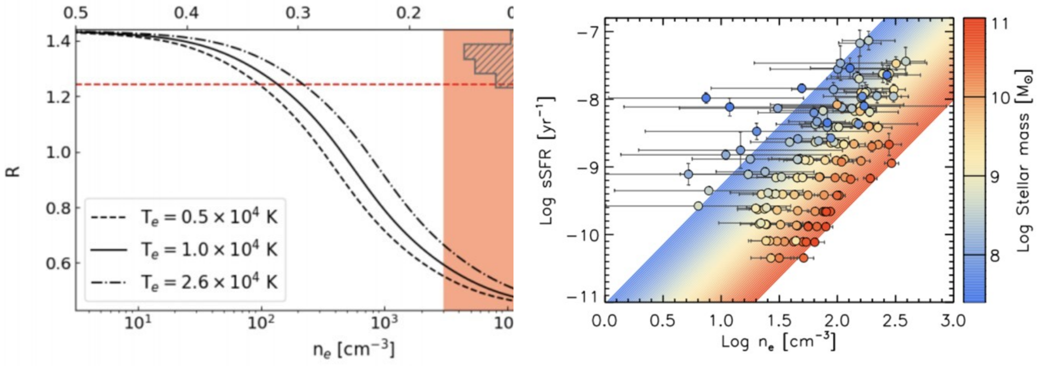

Figure 4.12 Left: The ratio R between the fluxes of the lines of the doublet [SII]$\lambda\lambda 6717, 6731$ as a function of the electron density n_e as presented by Iani et al., 2019 following a previous study by Proxauf, Öttl, and Kimeswenger, 2014. Right: The specific SFR as a function of n_e, color coded by $M_\star$ [Extracted from Kashino and Inoue (2018)].

$$\begin{aligned} log(n_e) =& 0.0543 tan(-3.0553R + 2.8506) + 6.98 - 10.6905R \\ &+ 9.9186R^2 - 3.5442R^3 + 0.5 log\left[-\frac{T_e(K)}{10^4}\right] \end{aligned} \tag{4.27}$$

Where R=F([SII]λ6716)/F([SII]λ6731). We assume a constant electron temperature - T_e - of 10^4K, a value widely adopted in literature (e.g. Iani et al. (2019)).

To obtain n_e, we refer to a relation between n_e and the specific SFR (sSFR, defined as the ratio $SFR[M_\odot\ yr^{-1}]/M_\star[M_\odot]$) proposed by Kashino and Inoue (2018) (see figure 4.12). They defined a set of equations and, in particular, the following to which we refer to:

$$log(sSFR) = -12.661 - 0.627 * log(M_\star - 10) + 1.753 * log(n_e) \tag{4.28}$$

Kashino and Inoue (2018) obtain this relation for a sample of galaxies located at 0.027 $\leq z \leq$ 0.25, extracted from the SDSS Data Release 7 (Abazajian et al., 2009). They estimated n_e from the ratio F([SII]λ6717)/F([SII]λ6731), assuming the electron temperature $T_e(S_+ = T_e(O_+)$ where $T_e(O_+)$ is estimated from F([OII]$\lambda\lambda$3726,3729)/F([OII]$\lambda\lambda$7320,7330) (Kashino and Inoue, 2018). We then obtain:

$$log n_e = \frac{(log(sSFR) + 12.661 + 0.627 * log(M_\star - 10)}{1.753} \tag{4.29}$$

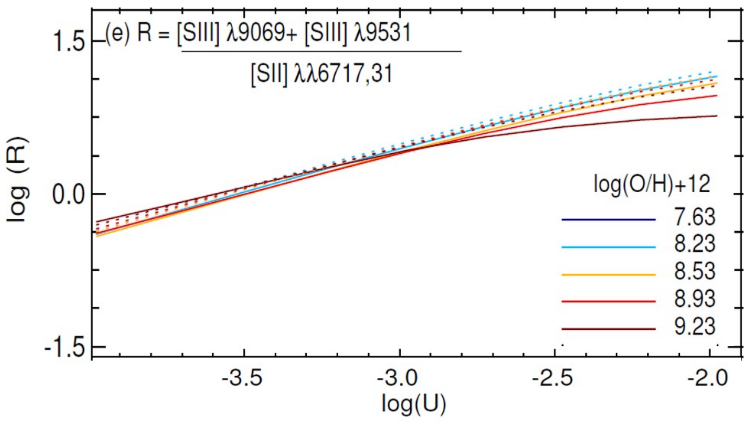

Figure 4.13 Ionization parameter diagnostic line ratios as a function of metallicity. We define $R = F^{corr}_{calc}([SIII]\lambda 9069) + F^{corr}_{calc}([SIII]\lambda 9531)/F^{corr}_{calc}([SII]\lambda\lambda 6717,6731)$. *We can see on the plot that the S32 ratio is almost insensitive to metallicity [Source: Kewley, Nicholls, and Sutherland (2019)].*

4.2.6 [SIII]$\lambda\lambda$9069,9531 fluxes from empirical calibrations

The doublet ([SIII]$\lambda\lambda$9069,9531) has been challenging to study due to its relatively long wavelengths, lying at the edge of classical optical spectrometer even for nearby galaxies. The red grism of Euclid will enable to catch the doublet lines up to a redshift $z \approx 0.9$. [SIII]$\lambda\lambda$9069,9531 is generally studied through the strong-line ionization parameter diagnostics S32 based on the ratio (F([SIII]λ9069) + F([SIII]λ9531))/F([SII]$\lambda\lambda$6717,6731). This ratio has been introduced by Kewley and Dopita (2002) for ionization parameter and abundance diagnostics and more recently studied by Morisset et al. (2016), Sanders et al. (2019), and Kewley, Nicholls, and Sutherland (2019).

In this study, we refer to a relation revealed by models presented in Kewley, Nicholls, and Sutherland (2019). They have shown that the S32 ratio is very sensitive to the ionization parameter (U), with a relatively small variation lower than 0.3 dex in our range of metallicity (see figure 4.13). This calibration still suffers from a complex temperature structures that can make the photoionization models underestimate the [SII] line strength (Levesque, Kewley, and Larson, 2010; Kewley, Nicholls, and Sutherland, 2019) that should therefore be considered with caution. We calculate the log(U) using the relation proposed by Kashino and Inoue (2018), for consistency with our previously calculated electron density n_e in section ?? that we also calculated using their relation. The relation is presented as follows:

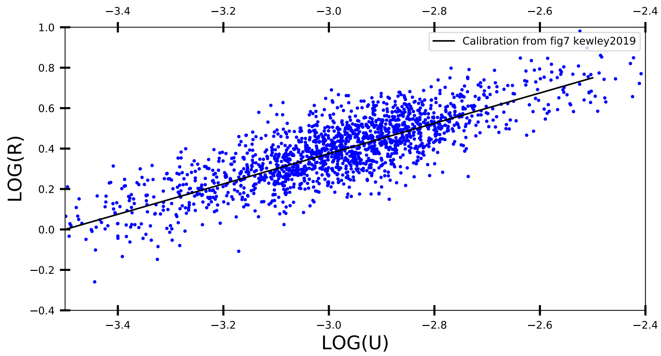

Figure 4.14 Ionization parameter diagnostic line ratios as a function of metallicity for sources from the B19 catalog (GOODS-N field). The black line represents the calibration presented in the figure 7 in Kewley, Nicholls, and Sutherland, 2019.

$$log(U) = -2.316 - 0.360log(O/H+4) - 0.292log(n_e) + 0.428[log(sSFR)+9] \tag{4.30}$$

Where the n_e and sSFR have been calculated in section ?? and we obtain log(O/H) using the eq.11 of the same paper such that:

$$12 + log(O/H) = 9.238 + 0.228[log(M_\star) - 10] - 0.401log(n_e) \tag{4.31}$$

We infer a best linear fit to the results presented by Kewley, Nicholls, and Sutherland (2019) as follows:

$$R = 0.75log(U) + 2.625 \tag{4.32}$$

Where:

$$R = \frac{F^{corr}_{calc}([SIII]\lambda 9069) + F^{corr}_{calc}([SIII]\lambda 9531)}{F^{corr}_{calc}([SII]\lambda\lambda 6717, 6731)}$$

We then obtain the value of the sum of the fluxes of the two lines of the doublet [SIII]$\lambda\lambda$9069,9531 such that:

$$F^{corr}_{calc}([SIII]\lambda 9069) + F^{corr}_{calc}([SIII]\lambda 9531) = 10^R * F^{corr}_{calc}([SII]\lambda\lambda 6717, 6731) \tag{4.33}$$

Finally, we inferred the flux of the individual lines of the doublet using the value for the theoretical ratio of 2.5 presented in Sanders et al. (2019) such that:

$$F^{corr}_{calc}([SIII]\lambda 9069) = \frac{F^{corr}_{calc}([SIII]\lambda 9531}{2.5} \tag{4.34}$$

4.3 Integration of the emission lines to the continuum

We have up to now presented the construction of the continuum, transformed it in vacuum and then shifted it to the observation frame considering the attenuation for reddening.

The emission lines fluxes in the observed frame previously calculated are also corrected by reddening. It remains to shift their relative wavelengths in the observed frame and to transform the integrated flux into a normally distributed flux around the central wavelength.

4.3.1 Conversion of the total fluxes calculated into Gaussian lines

In this section we present the procedure we apply for the Hα lines. The same procedure is applied for all the emission line fluxes calculated.

The predicted fluxes will be transformed into Gaussian Lines applying a sigma in the rest-frame of 3Å as provided by the models generated through GALAXEV (see section 4.1). We therefore redshift the sigma by applying the usual factor (z+1) such that $\sigma_{obs} = \sigma_{rest} * (1+z)$. In the same way, the mean wavelength ($\lambda_{H\alpha}$) of the Gaussian is derived by redshifting the wavelength of the line from the rest-frame to the observation frame. The amplitude ($A_{H\alpha}$) of the Gaussian is then defined as follows:

$$A_{H\alpha} = \frac{F^{corr}_{calc}(H\alpha)}{\sqrt{2\pi} * \sigma_{obs}} \tag{4.35}$$

We generate the Gaussian function, defined on a wavelength array ($Wave_{Unif}$) of the line as follows:

$$Gaussian_{H\alpha} = A_{H\alpha} * \exp \frac{-(Wave_{Unif} - \lambda_{H\alpha})^2}{2 * \sigma^2_{obs}} \tag{4.36}$$

Where $Wave_{Unif}$ is an array spanning a range from 4,000Å to 30,000Å with a step of 1Å. This array has been defined in order to standardize the array of the wavelengths. We mention here that the wavelengths of the model of the continuum are resampled with this same array $Wave_{Unif}$. We are therefore able to sum pixel per pixel the continuum and the Gaussian of the emission lines.

4.3.2 Broadening due to velocity dispersion

Previously, we accounted for the sigma of the templates (3Å) that we considered to broaden the emission lines. In this section, we describe the recipes to derive the velocity dispersion of the ionized gas. We refer to the relation inferred by Bezanson et al. (2018), observing about 1000 massive galaxies with the VLT/VIMOS in the LEAG-C survey, who have shown a dependence between the velocity dispersion of the ionized gas (σ_{gas}) and the total mass (M_{gas}) of the galaxy as follows:

$$log(\sigma_{gas}[kms_{\text{-}1}]) = -1.34 + 0.33 * log\left(\frac{M_\star}{M_\odot}\right) \tag{4.37}$$

This relation has a scatter of 0.17 dex and has been derived for galaxies located at redshift $0.6 \leq z \leq 1.0$. The relation has been confirmed for higher redshift $z \approx 2$ using data from the SINS/zC-SINF survey by Fõrster Schreiber et al. (2018). We then convert the σ_{gas} from km $s_{\text{-}1}$ into the FWHM in Å using the conversion relation as follows:

$$FWHM_{gas} = 2.3548 * \frac{\sigma_{gas}}{c[kms_{\text{-}1}] * \lambda} \tag{4.38}$$

Where $c[kms_{\text{-}1}]$ is the speed of light in vacuum in km $_{\text{-}1}$ and λ takes all the values of the wavelength vector $Wave_{Unif}$. We then obtain a FWHM$_{gas}$ evolving with the wavelength. We mention here that when the resulting value calculated for the FWHM$_{gas}$ is inferior to the FWHM due to the resolution of the continuum (3Å), we take the value of the resolution as a lower limit.

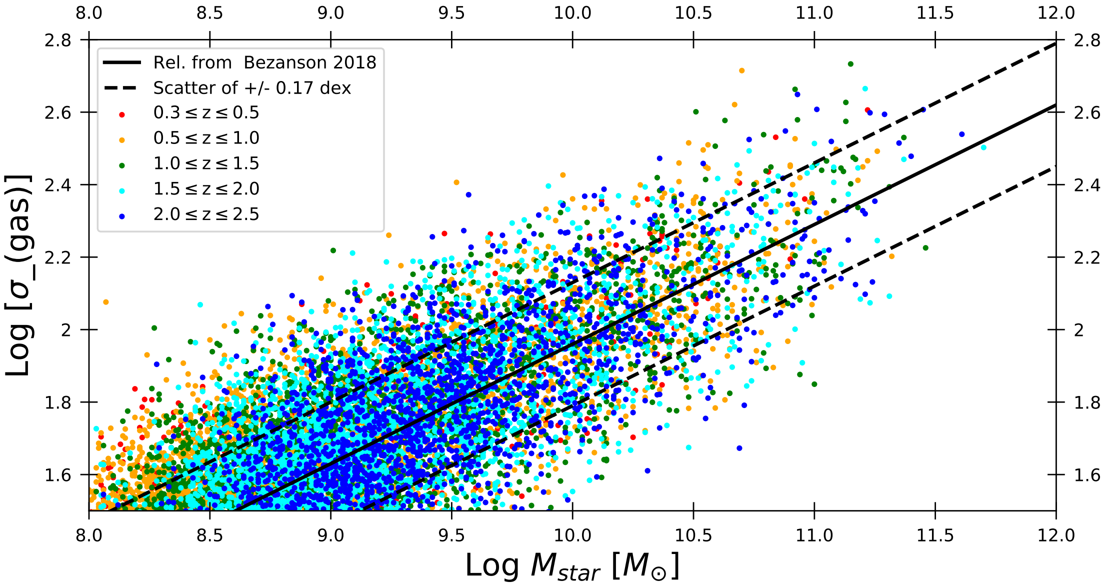

Figure 4.15 The velocity dispersion in km s_{-1} *calculated using the relation from Bezanson et al., 2018 for sources from the B19 catalog(GOODS-N field).*

Once the FWHM_{gas} is determined, we broaden the spectra (i.e. continuum+lines) accordingly by generating a Kernel Gaussian curve to be convolved to the spectra. To cope with the dependence on the wavelength, we make use of the function *ppxf/util.gaussian/filter1d* from the Python package *pPXF.py*, referring to the Penalized Pixel-Fitting method proposed by Cappellari (2017) which enable to convolve with a non-constant Kernel.

Chapter Five

Evaluation of the incident spectra

In this chapter we present the comparison and calibration of our emission line fluxes, calculated in chapter 4, with those available for the same galaxies in public spectroscopic surveys (section 5.1). In section 5.2 we describe the selection process applied, starting from the parent B19 CANDELS/GOODS-N sample, to build a subsample suitable for the PILOT RUN simulation, which required a limited number of galaxies (e.g., 1248), so to avoid mutual contamination among the spectra (see chapter 6.1). Finally, section 5.3 shows a photometric comparison of our incident spectra with publicly released photometric data.

5.1 Calibration of the calculated emission lines fluxes

5.1.1 GOODS-N field: comparison with 3D-HST

We compare our emission line calculated fluxes for the galaxies presented in the B19 catalog, with data obtained from the 3D-HST survey. 3D-HST is a near infrared slitless spectroscopy survey, covering the whole CANDELS field, using both the WFC3/G102 grism (wavelength range from 8,000Å to 11,500Å) and the WFC3/G141 grism (from 11,000Å to 16,000Å). The use of the two grisms yields to the detection of Hα-[NII]$\lambda\lambda$6584,6549, Hβ, [OII]$\lambda\lambda$3727,3729, [OIII]$\lambda\lambda 4959, 5008$, [SII]$\lambda\lambda$6717,6731 and [SIII]$\lambda\lambda$9069,9531 lines for a sample of ≈7000 galaxies at $1 \leq z \leq 3.5$ (Brammer et al., 2012).

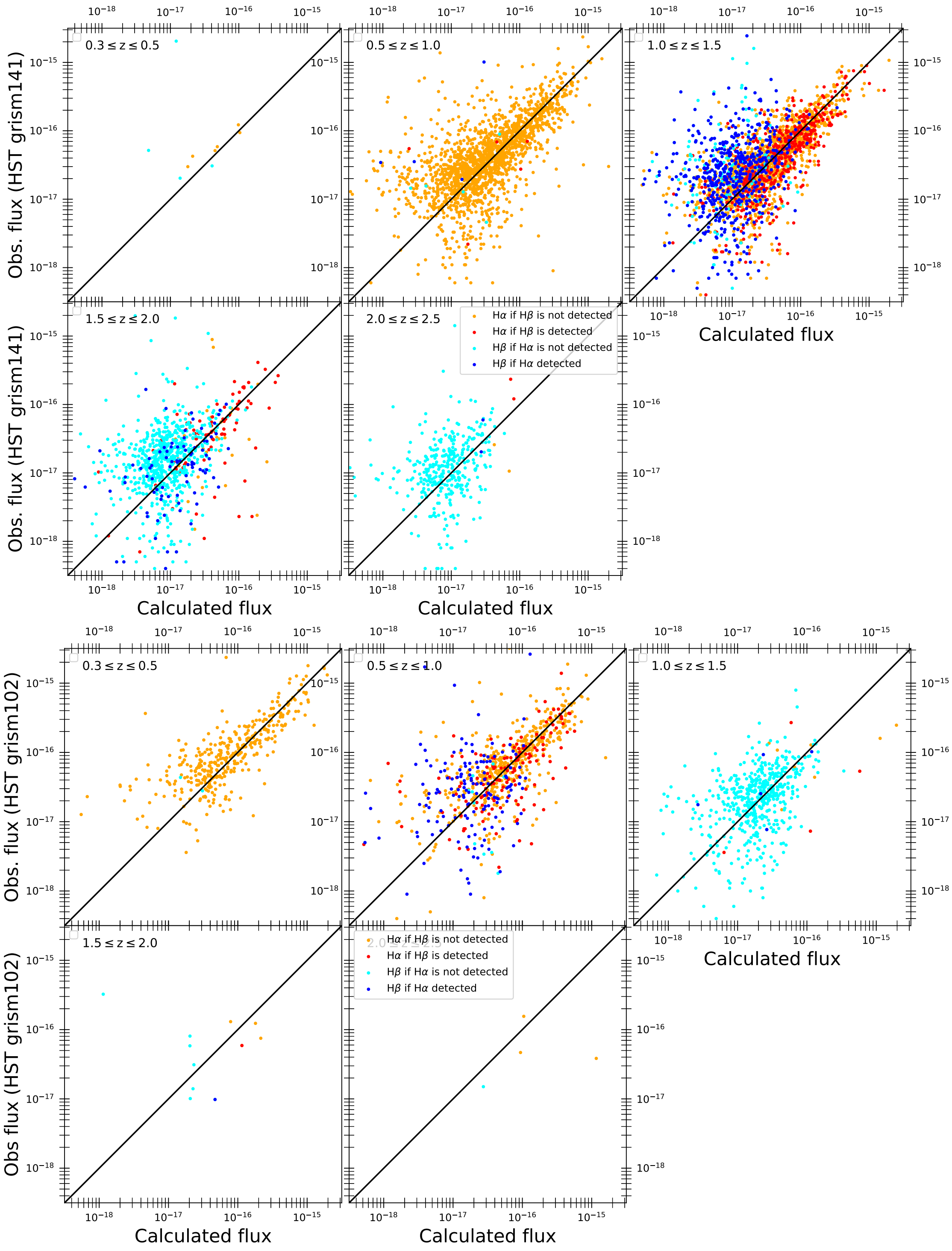

Figure 5.1 Comparison of our calculated fluxes for the Hα-[NII]$\lambda\lambda$6584,6549 and Hβ lines with publicly released data from the near infrared spectroscopic survey (3D-Hst) for sources of the B19 catalog. We show a comparison with data measured with the HST grism102 (top) and with the grism141 (below) on five different redshifts bins.

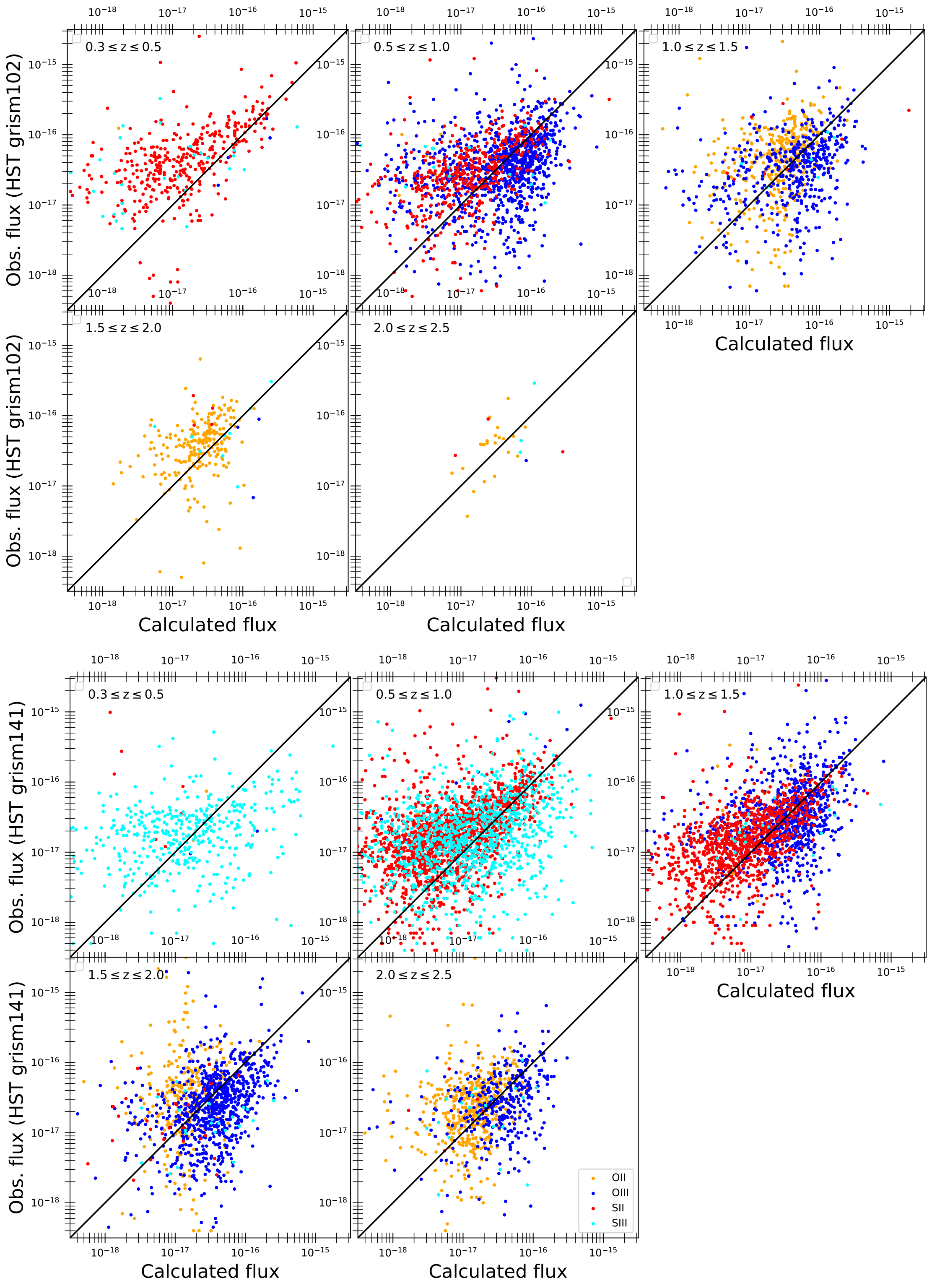

Figure 5.2 Comparison of our calculated fluxes for the [OII]$\lambda\lambda$3727,3729, [OIII]$\lambda\lambda$4959,5008, [SII]$\lambda\lambda$6717,6731, and [SIII]$\lambda\lambda$9069,9531 lines with publicly released data from the near infrared spectroscopic survey (3D-Hst) for sources of the B19 catalog. We show a comparison with data measured with the HST grism102 (top) and with the grism141 (below) on five different redshifts bins.

We note that the 3D-HST WFC3 grisms do not have enough resolution to deblend Hα and [NII]$\lambda\lambda$6584,6549[1], neither the [OIII] doublet. So, we also sum our calculated fluxes of the blended lines accordingly, for a proper comparison with the results of this survey.

We found a really satisfying agreement between our calculated Hα-[NII]$\lambda\lambda$6584,6549 fluxes with observation.

In order to make our calculated fluxes be as close as possible to reality, we applied a factor 1.5 to our estimations for the Hβ line fluxes in order to match with observations.

In section 4.2.5 we have presented two methods to convert the N_2-to-(O/H) linear calibration in the one used in our calibrations used to calculate the flux of the doublet [SII]$\lambda\lambda 6717, 6731$. While comparing our calculated fluxes from the two methods with observational data, results obtained from the second method are more in agreement with the observation. Again, our purpose being to be as realistic as possible using the strength of observational data, we decide to use the method 2 to infer the total flux of the doublet [SII]$\lambda\lambda 6717, 6731$. We present in figure 5.1 and 5.2 an overview of the comparison after calibration.

5.1.2 COSMOS field: comparison with 3D-HST, FMOS and LEGA-C

As for the GOODS-N field, the 3D-HST survey also covers a part of the COSMOS field. Moreover, other spectroscopic surveys, detecting rest-frame optical emission lines at intermediate and high-redshift are available in COSMOS. The largest public surveys covering our redshift range are the Subaru/FMOS-COSMOS (z=1-2), and the Large Early Galaxy Astrophysics Census, LEGA-C. The latter utilizes the VIMOS multi-object spectrograph at the ESO Very Large Telescope, and covers 1.3 square degrees within COSMOS field, obtaining deep continuum spectroscopy of several thousand of galaxies at redshifts 0.6 to 1. Like previously mentioned for the sources of the B19 catalog, we applied a factor 1.5 to our

---

[1] Written Hα-[NII]$\lambda\lambda$6584,6549 in this Thesis.

calculated Hβ line fluxes. We present the comparison in appendix figure 5.

5.2 Selection of galaxies to be simulated

As mentioned above, the PILOT RUN for the NISP-S simulations was conceived to avoid contamination from overlapping spectra on the detector. This requires a maximum number of 1248 galaxies at a time (i.e. per pointing). In the preliminary phase study, as covered in this work, we perform a simulation for one pointing using the GOODS-N library.

We describe in the following the source selection procedure applied for this pointing. In order to have the largest possible number of emission lines detected in a deep field-like configuration, we select the strongest line emitters in our sample. The emission lines potentially detected by the NISP Red-Grism change with the redshift of the sources. So, for each redshift bin we set a flux lower limit of 4.5×10^{-17} erg s^{-1} cm^{-2} Å^{-1} to the emission lines falling in the NISP Red-Grism wavelength range [12,220Å–18,770Å] (see figure 5.3). We list in table 5.1 the redshift windows for the strongest emission lines of interest.

We also applied a last morphological selection criterion, before obtaining the 1248 galaxies for the first *pointing* of the PILOT RUN. We remove galaxies that remain unclassified (i.e. flag=5) in the morphological catalog by Dimauro et al. (2018), while being bright emitters with $H_{AB} \leq 21$ and $F_{H\alpha} \geq 1 \times 10^{-16}$ erg s^{-1} cm^{-2} Å^{-1}. The analysis of the simulated spectra from this first pointing will be presented in Chapter 6.

We present in figure 5.4 an overview of the *Main Sequence* of the 1248 galaxies taken from the B19 catalog to be simulated by the PILOT RUN. We present in table 5.2 a quick overview of parameters of the sources contained in the pointing of the PILOT RUN.

Emission lines	Redshift window for observation
Hα	[0.9;1.8]
Hβ	[1.6;2.8]
[NII]λ6584	[0.9;1.8]
[SII]λ6731	[0.85,1.75]
[OIII]λ5008	[1.5;2.7]
[OII]	[2.35;4.9]
[SIII]λ9531	[0.3;0.9]

Table 5.1 Redshift window for observation through the NISP spectrometer (red grism). The redshift window is obtained using the relation $\lambda_{obs} = \lambda_{rest} * (1 + z)$ *and considering the range covered by the NISP red grism [12,220Å–18,770Å].*

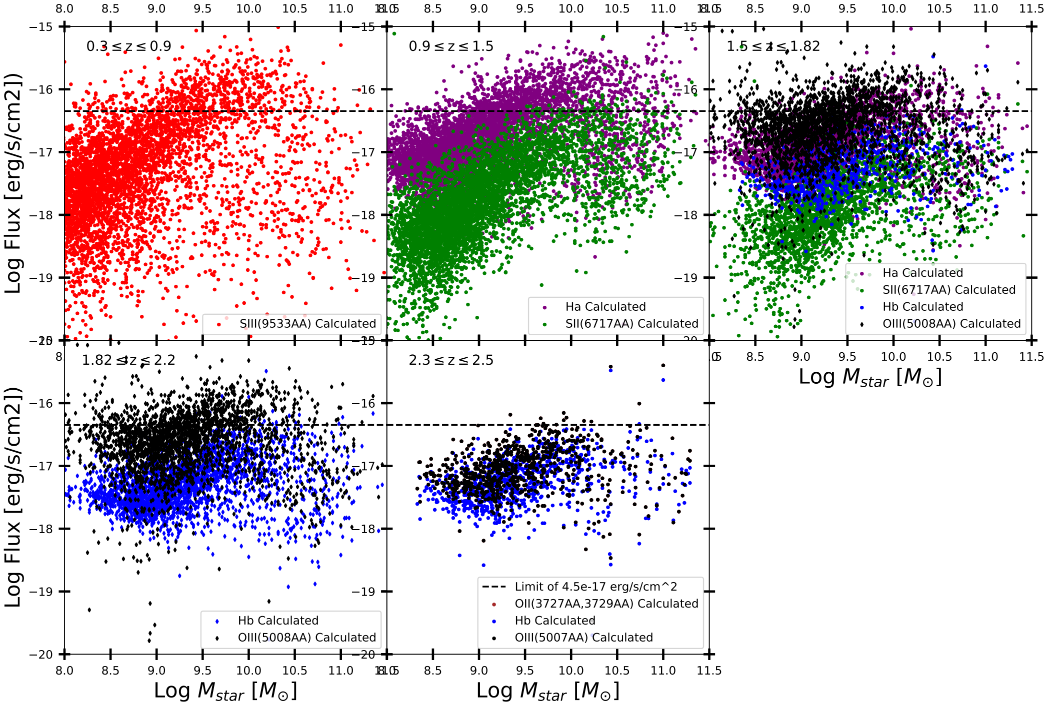

Figure 5.3 Calculated fluxes for sources of the B19 catalog showing emission lines in their respectice redshift window of observation with the NISP-S red grism. For each redshift bins, sources with emission line flux above the limit set at 4.5 erg s^{-1} cm^{-2} Å^{-1} (dashed black line) are kept in our selection to be simulated.

Redshift	Number sources	H(AB)	$\log(M_{star}/M_{\odot})$	$\log(\mathrm{SFR}[M_{\odot}/\mathrm{yr})$	Av
0.3≤z≤0.5	126	18.06-23.95	7.69-11.08	-2.62-2.11	0.0-3.4
$0.5<z\leq1.0$	454	18.40-24.20	8.09-11.22	-1.32-2.63	0.0-3.7
$1.0<z\leq1.5$	334	19.74-23.95	8.89-11.31	0.11- 2.81	0.0-2.8
$1.5<z\leq2.0$	184	20.65-24.39	8.73-11.31	0.37-2.88	0.0-2.8
$2.0<z\leq2.5$	96	18.51-24.38	8.93-12.03	0.5-3.46	0.0-2.7

Table 5.2 Description of some parameters of the 1248 sources selected from the B19 catalog (GOODS-N field). All these spectra of galaxies will go through the NISP simulator.

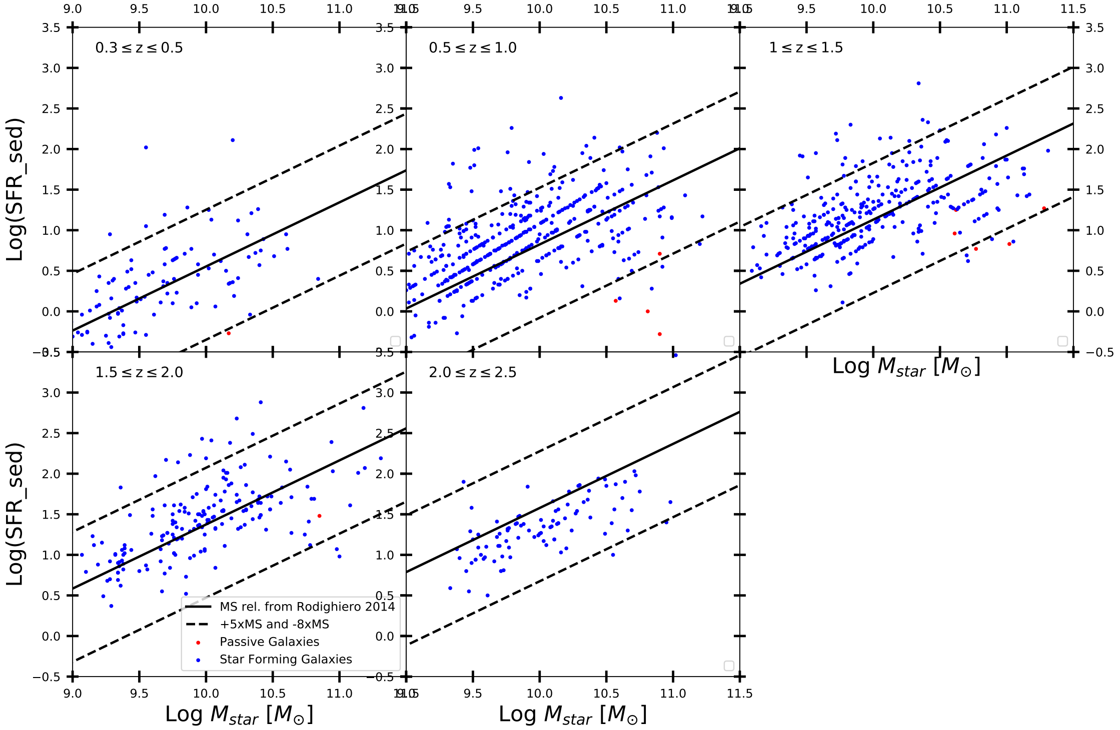

Figure 5.4 The Main Sequence of the sample of 1248 galaxies taken from the B19 catalog to be simulated by one pointing of the PILOT RUN. The SFR is in [$M_{\odot}$/yr]. We see that just a few galaxies identified through the UVJ-diagram (Williams et al., 2009) as Passive galaxies remain in our selection. The black line is the normalization of the Main Sequence from Rodighiero et al. (2014). The black dashed lines represent a reference for sources that can be identified as Starburst galaxies (+5xMS) and Passive galaxies (-8xMS) based on the MS normalization.

5.3 Photometric evaluation of the incident spectra

In this section, we compare the incident spectra built along this Thesis with photometric data found in the literature and in particular data from the SHARDS and *HST* surveys. We eventually provide predictions of fluxes and magnitudes measured convolving our incident spectra with the Euclid filters.

The Survey for High-z Absorption Red and Dead Sources (SHARDS), part of the CANDELS survey (Grogin et al., 2011; Koekemoer et al., 2011), observed all the GOODS-N field in 25 medium-band different filters with GTC/OSIRIS covering the wavelength range between 5,000Å and 9,500Å with contiguous passbands. We also make use of data provided by the *HST* and its WFC3 and ACS (see appendix table 1 for the effective wavelengths of the filters). This final check is very useful to validate our incident spectra validating the consistency between the best-fit parameters derived by B19 used to generate the continuum and the SHARDS and HST photometry. We show on the figure 5.5 the results from the photometric check. We have converted the values available in the catalogs from Jansky into CGS (i.e. erg s^{-1} cm^{-2} Å^{-1}) as follows:

$$F[erg\ s^{-1}cm^{-2}\text{Å}^{-1}] = \frac{F[Jy] * 10^{-6}}{33400 * \lambda_{Eff}^{2}[\text{Å}]} \tag{5.1}$$

For completeness, we convolve the templates with the Euclid filters VIS, Y,H and H (see section 2.3) to obtain magnitudes as expected to be measured by the Euclid telescope. We describe here the approach to obtain the AB magnitudes and integrated fluxes in CGS:

1. We resample the filters' wavelengths with the standardized array $Wave_{Unif}$
2. We calculate the flux $f\nu$ (in $erg\ s^{-1}cm^{-2}Hz^{-1}$) integrating the filters' response with our spectra using the function SIMPS (Simpson's rule for integration) from the Python package *scipy.integrate* applied to the quotient of the filter's response with the wavelength array (giving $Simps_1$), and to the product of the filter's response by our incident

spectra divided by the wavelength array (giving $Simps_2$). We then obtain $f\nu$ as follows:

$$f\nu = \frac{Simps_1}{Simps_2 * c[\mathring{A}/s]} \tag{5.2}$$

where c[Å/s] is the speed of light in vacuum.

3. We then convert $f\nu$ into AB magnitude with the relation:

$$m_{AB} = -2.5 * log_{10}(f\nu) - 48.6 \tag{5.3}$$

4. We finally convert the flux $f\nu$ into CGS as presented in equation 5.1.

We present in figure 5.5 an example of this evaluation with SHARDS and HST data as well as the predictions in flux measurement with the Euclid filters.

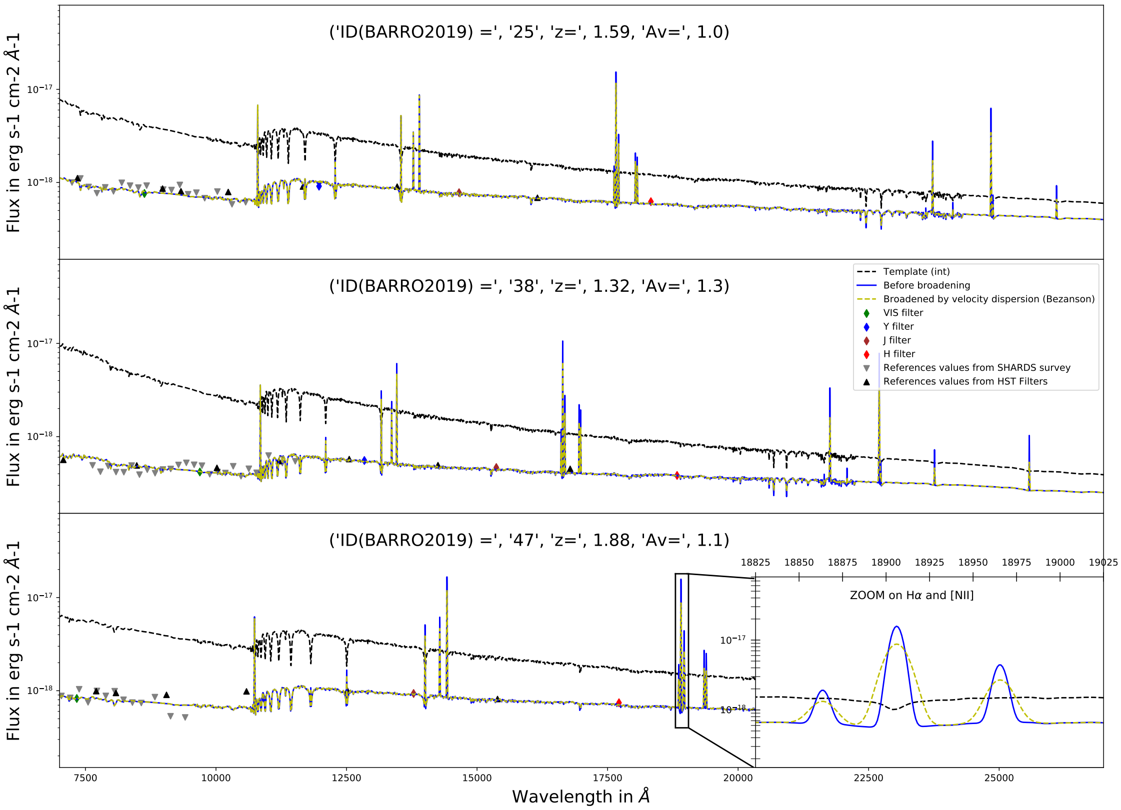

Figure 5.5 Examples of spectra from the spectral library created in this Thesis. The sources are extracted from the B19 catalog. The continuum is obtained from SED-fitting parameters using the library of evolutionary stellar population synthesis models GALAXEV (Bruzual and Charlot, 2003). The emission lines are calculated following calibration from observation and photoionization models. The black line represents the spectra without absorption, the blue line is the spectra after correction. The yellow line is the spectra broadened for velocity dispersion calculated using the relation proposed by Bezanson et al., 2018. We show on the bottom right a zoom on the Hα, and the doublet [NII]$\lambda\lambda$6584,6549 line that enables to see how the broadening is modifying the lines. The black and grey triangles are respectively data retrieved from the HST and SHARDS surveys. For completeness, we also indicate with the colored diamonds the integrated flux expected to be measured with the Euclid filters. The spectral library created in this way will go through the Euclid NISP-S simulator, aiming at providing the pipeline to evaluate the NISP capabilities.

Chapter Six

Analysis of the spectra produced by the NISP-S simulator

In the previous chapters we have gone through the construction of spectral libraries (referred to as the incident spectra) starting from SED-fitting parameters of real galaxies from the CANDELS/GOODS-N and COSMOS fields. These spectra have been created to go through the pipeline, which simulates the actual NISP-S observations, under both the Wide and Deep survey configurations. This run of simulation (the so-called PILOT RUN) has been carried out in the IASF/INAF at Milan, and in collaboration with INFN-Genova.

In this chapter, section 6.1 describes the PILOT RUN. Then, in section 6.2 we describe the procedure to extract 1D spectra from simulated NISP-S simulated data. Sections 6.3 and 6.4 go through the analysis of the simulated 1D spectra, in particular continuum and emission lines measurements, respectively. Finally, in section 6.5 we present a preliminary stacking analysis.

The PILOT RUN prepared in this thesis will be a crucial starting point for the Euclid community, not only to test and validate the performance of the current version of the pipeline for data reduction[1], but also to prepare some advanced data processing procedures for data analysis (e.g., for stacking, see section 6.5). In the following, we will go through the

---

[1] SIR Pipeline, version August 2020

analysis of the simulated spectra of galaxies from the CANDELS/GOODS-N field.

6.1 The PILOT RUN simulation

This master Thesis has been conceived in synergy with the Euclid Legacy Science Working Groups (SWGs), as part of the preliminary evaluation of the expected spectroscopic survey performances of the Euclid mission. The Thesis, therefore, aims at confirming that under the Wide and Deep survey configuration, the telescope and its slitless NISP-S spectrometer behave as expected, and reach the detection limit requirements for both the continuum and nebular emission detection. The PILOT RUN also aims at testing and validating the data processing pipeline for the Euclid spectroscopic survey.

The PILOT RUN is organized starting with the study of two pointings: one will simulate the Wide field configuration while the other will simulate the Deep field configuration, in terms of exposure time[2]. The former consists in 2,212 s exposures splitted into of 4-dithered frames (each of which is 553.0 s), to cope with pixel systematics. The latter consists in 5 sets of exposures, with 4-dithered frames each (i.e. 20 frames in total). This corresponds to an exposure time equivalent to 11,060 sec.

In practice, the pipeline places each simulated galaxy in a certain position of a simulated sky and then recreates the output of the observations of the instrument. In order to avoid the overlap of the 2D spectra on the detector, we reduce the amount of galaxies per pointing, and we locate them on the FoV following an ordered pattern. This leads to an upper limit of 1248 galaxies per pointing (see section 5.2 for the selection procedure). The analysis of the contamination problem that will be presented in the future observations is beyond the scope of this thesis. The pipeline performs the reduction and extraction of the 1D spectra as well

---

[2] It is worth to note that the Euclid Deep Survey configuration, will also require the Blue-Grism mounted on the NISP spectrograph. However, the Blue-Grism is not used in this work, since the related pipeline is still undergoing fundamental validation tests.

as the wavelength and flux calibrations. The 1D spectra are created using a fixed aperture around each galaxy. We will discuss the aperture effect in section 6.3. The simulator also generates the variance, by considering all the different sources of noise, e.g., the zodiacal light, the readout noise, and the Dark current.

We present in this chapter a preliminary analysis of the simulated spectra from the library containing sources from the GOODS-N field. We therefore prepared a sample of 1248 sources from the CANDELS/GOODS-N field, as detailed in the previous chapter and shown in table 5.2, initially constructed for the Euclid Deep field simulations. To date, as previously mentioned in section 3.2, only one out of the planned 5 sets of simulations required for the Deep field configuration has been completed, e.g., corresponding to a total of 4 dithered frames, as in the Wide field configuration. Further simulations are in preparation. The PILOT RUN based on the GOODS-N catalog, is still on-going and will be completed to reach the total integration time of the Deep field. Then, the library with sources from the COSMOS field will be used to select the brightest and most massive galaxies for the Wide Field simulation PILOT RUN.

6.2 1D spectra

The simulator provides files in the Hierarchical Data Format (HDF) from which we retrieve the 1D spectral fluxes, variance and root mean square (rms). The spectra obtained are defined on the NISP-S wavelength range [12,220Å–18,770Å] with a pixel scale of 13.4Å/px. The Wide field configuration consists in 4-dithered frames that are combined calculating the weighted mean and its corresponding variance. This step is also provided by the pipeline. We present here the detail of the combining procedure performed by the pipeline. This procedure has been validated in this thesis, starting from the 4-dithered frames and comparing our final results with the combined spectra. We derive the combined spectrum ($\bar{f}$) as the weighted mean of the 1D spectra from the 4-dithered frames as follows:

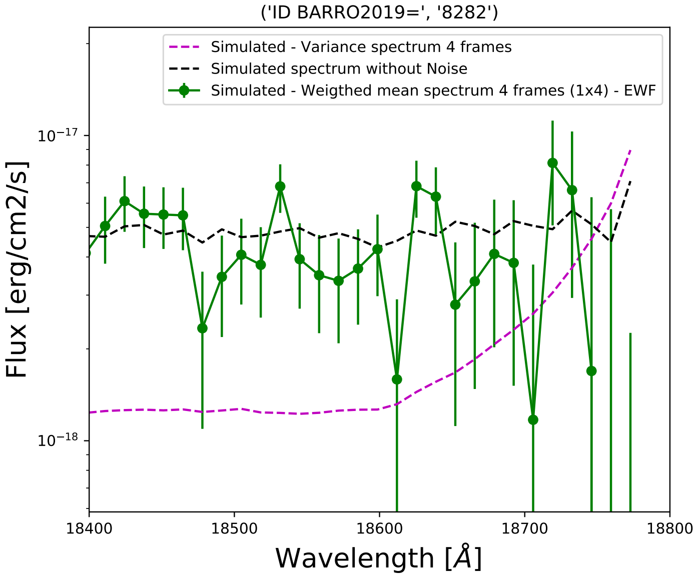

Figure 6.1 Example of a simulated spectrum illustrating the behaviour of the variance spectrum at the red edge of the NISP red grism. We can see an increase in the variance for wavelengths above 18,600Å. This behavior is observed for all the sources.

$$\bar{f} = \sum_{i=1}^{n} w_i . f_i \tag{6.1}$$

Where n is the amount of frames, f_i are the observed fluxes and w_i are the corresponding weights. The weight is defined as the inverse of the variance $w_i = \frac{1}{\sigma_i^2}$ where ${\sigma_i}^2$ is the variance. We make this calculation for all the pixels.

We then propagate the error assuming a Gaussian behaviour to obtain the standard error of the weighted mean for each pixel as follows:

$$\sigma = \left(\sqrt{\sum_{i=1}^{n} w_i} \right)^{-1} \tag{6.2}$$

The error is then inversely proportional to the amount of frames decreasing like $\sqrt{n}$. We recall here that the Deep field configuration consists in 20 frames (5 exposures x 4-dithered frames), making the noise $\sqrt{5}$ times lower than a the Wide field configuration.

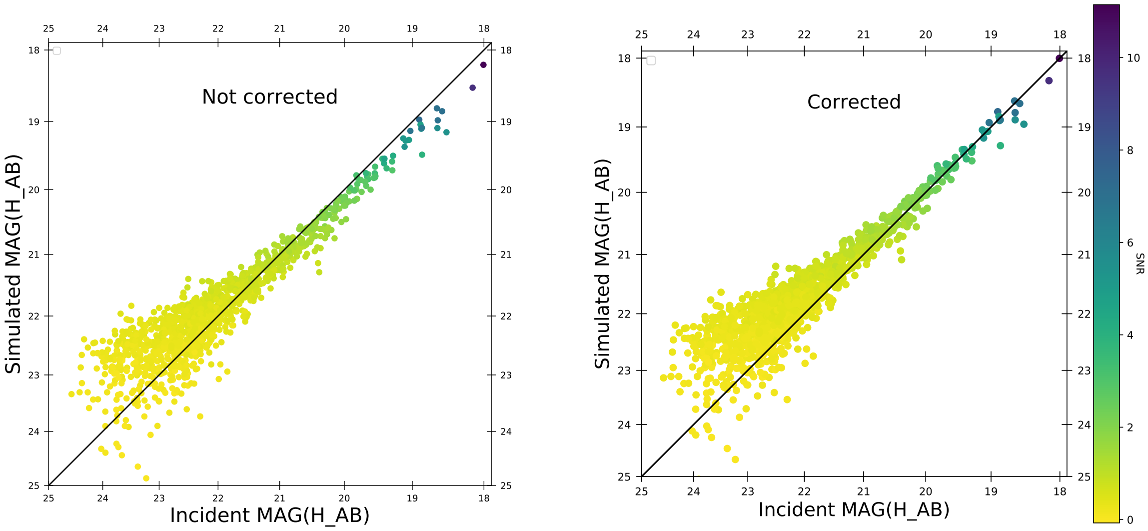

Figure 6.2 Comparison of the simulated H magnitudes in the AB system with the incident magnitude. To obtain the magnitude, we convolve the simulated and incident spectra with the Euclid NISP-H filter. We present the comparison with the simulated magnitudes uncorrected on the left, corrected on the right for aperture loss. Using the least square method for sources with H(AB) leq *20.5 with a detection at* 3σ*, we find a best fitting corresponding to a 20% loss due to the aperture. The results after applying the aperture correction is shown on the right panel. In both the panels the sources are color coded according to their S/N ratio (SNR), as shown by the right-side color bar.*

6.3 Continuum measurements

We present here the evaluation of the continuum detection by the NISP spectrometer. We convolve the simulated spectra with the Euclid NISP-H filter. We compare the magnitude of the incident spectra with the magnitude obtained from the convolution of the simulated spectra with the filter. We consider the difference in the limit wavelength towards the red between the red grism [12,220Å–18,770Å and the H-filter [15,440Å-20,000Å], by cutting the response filter for wavelengths above 18,600Å. The limit 18,600Å enables to avoid the red edge of the simulated spectra, where the variance starts to increase (see figure 6.1).

We calculate the magnitudes as presented in section 5.3, convolving the Euclid NISP-

H filter with the simulated and incident spectra. We present in figure 6.2 the comparison between the values calculated from the incident spectra and the values calculated from the simulated spectra. In order to account for the aperture loss, we fit the data with a linear function and subsequently derive the multiplicative factor needed to correct the fluxes. We find an estimate for the aperture correction of 20% for the sources with an incident magnitude H(AB) $\leq$ 20.5. We present in figure 6.2 the results before and after aperture correction.

Regarding the calculation of the SNR, we defined the signal as the mean flux value of the simulated spectra on the wavelength range covered by the NISP-H filter. The noise is then calculated summing in quadrature the rms spectra in the wavelength range of interest and dividing it by the amount of pixels within that wavelength range, in order to obtain both signal and noise in erg s^{-1} cm^{-2}/px.

We can observe in figure 6.2 that the match of the magnitudes measured convolving NISP-H filter's response with the incident and simulated spectra is very satisfying all the way up to magnitude H(AB) $\approx$ 22. The detection limit expected for the magnitude H(AB) of 19.5 with the NISP-S is reached and even overcame in this first analysis, providing us with detection limit for H(AB) magnitude $\geq$ 20.5 with a detection at 3σ. This very positive results is to be confirmed in future studies and in particular completing the PILOT RUN.

6.4 Emission lines measurement

6.4.1 Emission lines fitting

In the this section we will estimate from the Euclid detection limit for emission lines with a SNR $\geq$ 3.5 and compare our values with the NISP specifications (see table 2.1) in terms of spectroscopic limits for emission line detection, set at 2×10^{-16} erg s^{-1} cm^{-2} for the Euclid Wide survey (Racca et al., 2016).

We describe here the procedure used to detect the emission lines from the simulated

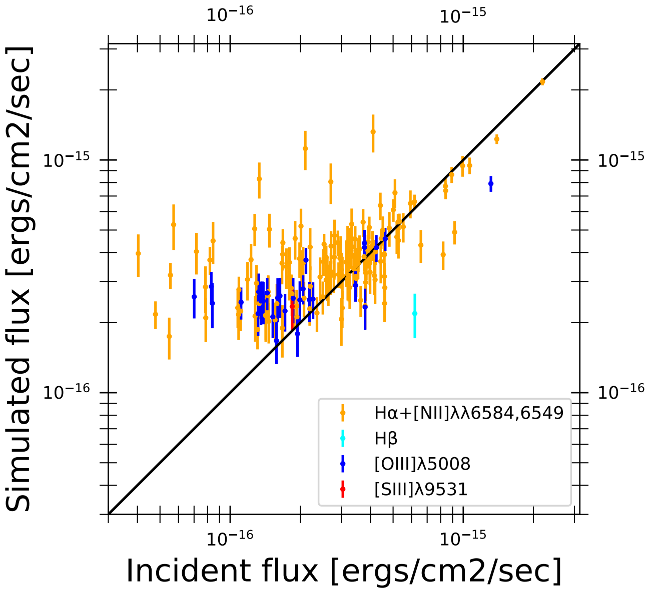

Figure 6.3 The measured fluxes of the simulated spectra versus the incident fluxes for the lines Hα+N[II], Hβ, [SIII] and [OIII]. The aperture correction of 20% derived with the continuum in section 6.3 has been applied to the measured fluxes. As expected we predominantly detect Hα lines. We can see a clear improvement in the fit above the limit 1×10^{-16} erg s^{-1} cm^{-2} to obtain a satisfying match above the expected NISP limit for emission lines' detection set at 2×10^{-16} erg s^{-1} cm^{-2}. All the emission lines presented here have a SNR $\geq$ 3.5.

spectra and measure emission lines fluxes with their corresponding FWHM and SNR.

For the detection and measurement of the emission lines, we make use of the Python package SPECUTILS. First of all, we fit the continuum with a linear interpolation using the function *Linear1D* and the function *fit.generic.continuum* that will be subtracted from the simulated spectra.

We assume Gaussian distributions for the emission lines. To identify and fit the lines with a Gaussian curve, from which we infer the flux and the FWHM. We indicate the central wavelength[3] of the Gaussian curve for each of the lines of interest and leave the FWHM and amplitude as free parameters.

We obtain the total flux of the emission lines using the function *line.flux*. In section 6.3, we found an estimation of 20 for the aperture correction. We mention here that we apply this correction to the measured fluxes of the emission lines.

---

[3] The central wavelength is calculated considering the lines' wavelength at rest-frame and the redshift of the source.

6.4.2 Calculation of the Signal to Noise Ratio (SNR)

For the calculation of the SNR, the signal is calculated integrating the Gaussian fit on a wavelength range $[\lambda_{mean} - 2\sigma; \lambda_{mean} + 2\sigma]$ where λ_{mean} is the central wavelength of the Gaussian fit and σ is obtained using the function ***stddev.value***. The signal is then obtained integrating using the function ***line.flux***[4]. The Signal is therefore obtained from:

$$Signal = \int_{\lambda_{mean}-2\sigma}^{\lambda_{mean}+2\sigma} Spec_{fit} d\lambda \tag{6.3}$$

Where $Spec_{fit}$ is the fit to the spectrum obtained with the procedure presented above and σ is the standard deviation of the line. We here obtain a signal in erg s^{-1} cm^{-2}.

The Noise is then obtained by summing in quadrature the rms of the pixels included in the interval $[\lambda_{mean} - 2\sigma, \lambda_{mean} + 2\sigma]$. We therefore also obtain the Noise in erg s^{-1} cm^{-2}.We then consider the detection being successful for emission line fluxes presenting a SNR ≥ 3.5.

Emission lines	Number detected with SNR ≥ 3.5
Hα-[NII]$\lambda\lambda$6584,6549	145
Hβ	1
[OIII]λ5008	29
[OII]λ3729	0
[SIII]$\lambda\lambda$6717,6731	5

Table 6.1 Quantitative description of the first results from fitting the emission lines with a Gaussian function. We see that the $H\beta$ lines has been detected with a SNR>3.5 for only one source, and none for [OII]. Most of the detected emission lines are Hα and [OIII]λ5008.

We present in figure 6.3 the results obtained for the emission lines with a SNR>3.5 Hα-[NII]$\lambda\lambda$6584,6549, Hβ, [OIII]λ5008 and [SIII]λ9531.

The selection of the sources presented in figure 6.3 is made in two steps. First we select the sources with an SNR > 3.5, and then we make a check on the individual spectra to discard wrong identifications. For example, we obtain three sources with Hβ emission line fluxes detected with a SNR > 3.5, among which we kept only one. We show on figure 6.4 the Hβ emitter recognized as coherent and indicated on figure 6.3. On figure 6.6, we present a candidate Hβ emitter recognized as a wrong identification and is therefore discarded.

---

[4] All functions here are from the Python package SPECUTILS

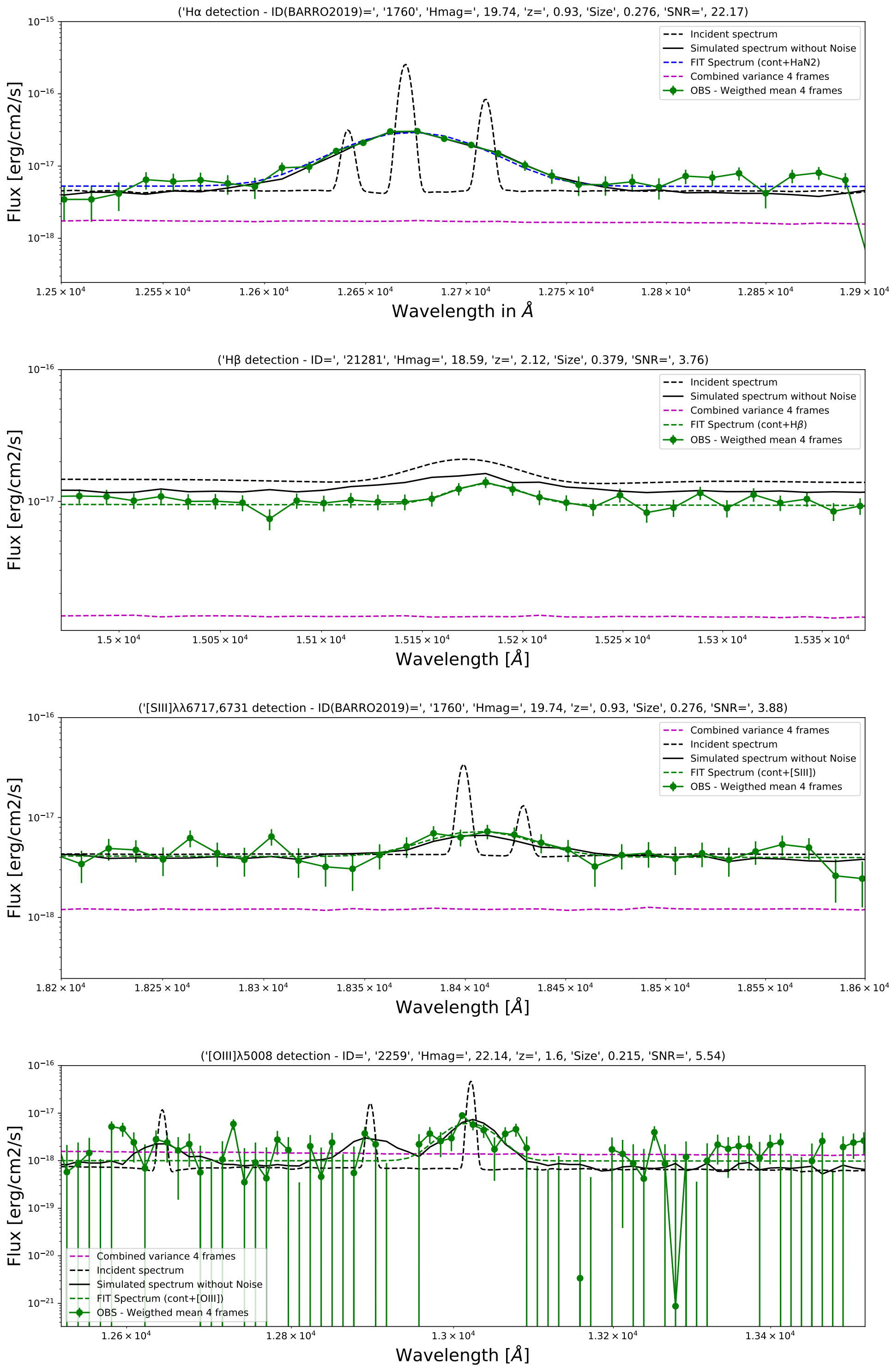

Figure 6.4 Examples of simulated spectra displaying the Hα, Hβ, [SIII]λλ6717,6731 and [OIII]λ5008 from top to bottom. On top of each graph, we indicate information relative to the source.

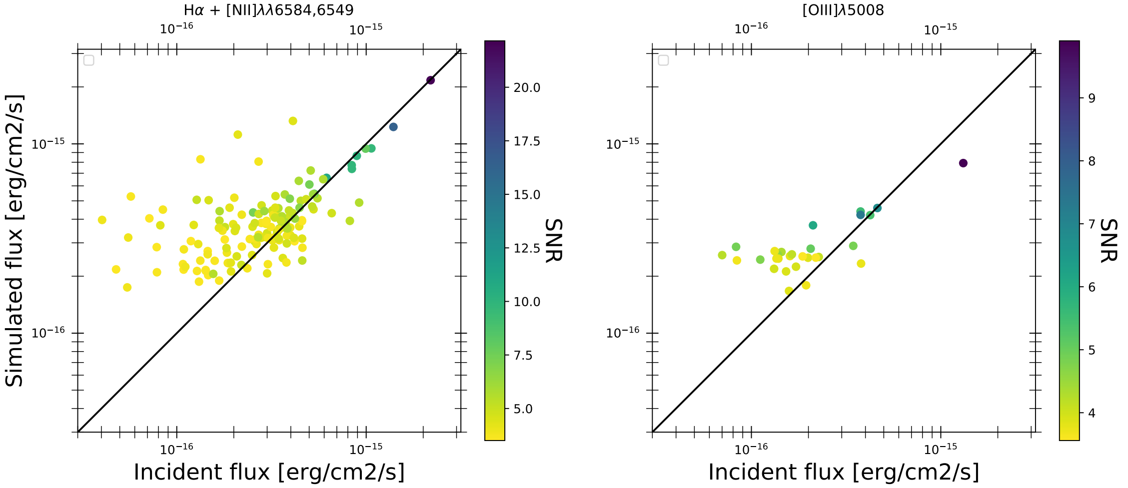

Figure 6.5 The simulated versus incident fluxes of Hα-[NII]$\lambda\lambda$6584,6549 and [OIII]λ5008, color coded by the SNR of the lines. The aperture correction of 20% derived with the continuum in section 6.3 has been applied to the measured fluxes. We can see that the match between simulated and incident fluxes becomes satisfying between 1×10^{-16} and 2×10^{-16} erg s^{-1} cm^{-2}. This result potentially confirms the detection limit for the Wide field configuration set in 2×10^{-16} erg s^{-1} cm^{-2}. A further analysis will enable to validate this result.

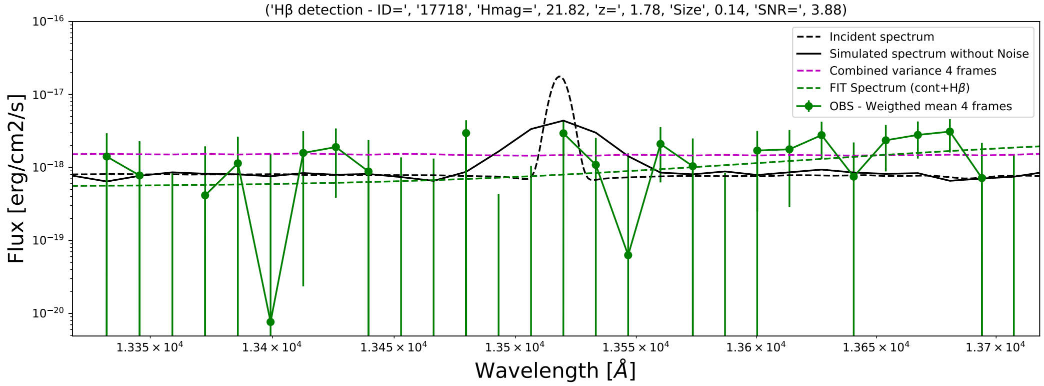

Figure 6.6 Example of a spectrum of a measured Hβ line with SNR>3.5 and discarded from the list of detected lines. We can see that the detected emission behaves in a way that cannot be attributed to the detection of the Hβ line.

We mostly detect the blended Hα-[NII]$\lambda\lambda$6584,6549 lines. We only detect one Hβ line, probably due to the absorption from the HII region and broadening of the line due velocity dispersion that make the line under the NISP detection capabilities. Hα-[NII]$\lambda\lambda$6584,6549 is also affected by these two parameters but is intrinsically more luminous (see section 4.2.2). A further analysis would be required on this particularly important aspect relative to the Hβ line in the upcoming simulations. The line [OIII]λ5008 has been detected for 29 sources. We mention that the line [OII]3729 is not detected in this first analysis due to the low signal at redshift $z \geq 2.35$ (i.e. when [OII] enters the red grism wavelength range). A summary of the detection performed is presented in table 6.1 where we indicate the number of emission lines detected, i.e., with SNR $\geq$ 3.5.

We can see in figure 6.3 presented above and in figure 6.5, showing the same comparison between the incident and simulated fluxes but color coding with the SNR the measured fluxes for the Hα-[NII]$\lambda\lambda$6584,6549 and [OIII]λ5008 lines, that the detection limit expected from the NISP spectrometer of 2×10^{-16} erg s^{-1} cm^{-2} (see table 2.1) seems to be reached for the spectra generated by the NISP-S simulator. Indeed, on both figures we can see a clear improvement in detection above 1×10^{-16} erg s^{-1} cm^{-2} to become very satisfying above 2×10^{-16} erg s^{-1} cm^{-2} to become very accurate above 3×10^{-16} erg s^{-1} cm^{-2}. This result is very promising, validating the simulated spectra as well as confirming the spectroscopic detection limit of the NISP. This result will need to be confirmed completing the PILOT RUN.

6.4.3 The spectral resolution of the simulated spectra

Since the spectroscopy performed by the NISP-S is slitless, the nominal dispersion of the spectra gets convolved with the object size along the dispersion axis (see section 2.2.3). To quantify the effect of the size on the dispersion, we plot the FWHM of the instrument as a function of the size along the dispersion axis. For simplicity, and due to the lack of mutual contamination among the spectra, in the PILOT RUN the dispersion direction has been set horizontally in the field of view for all the simulated spectra, corresponding to 0 or 180 degrees grism orientations, so neglecting the tilted grism configuration. Hence, to obtain the

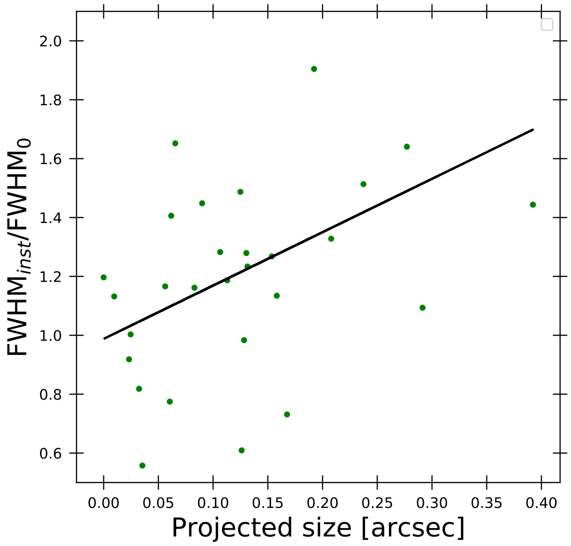

Figure 6.7 The spectral resolution of the NISP-S simulator as a function of the object size for detected [OIII]$\lambda 5008$ emission lines in sources extracted from the B19 catalog. The detection has been done for a simulation in the Wide field configuration. Following the normalization presented by Pasquali et al. (2006a), the object radius along the dispersion axis is plotted in abscissa in arcsecs. The FWHM of the line (FWHM$_{inst}$) is represented in the ordinate axis as a multiple of the FWHM of a 0".5 source diameter (FWHM$_0$). The resolution seems in agreement with the specification set at $R = \lambda/\Delta\lambda = 380$ for a 0".5 diameter source.

size along the dispersion axis, we project the Disk Length along the dispersion axis using the Disk Angle, both parameters are available in the B19 catalog.

We then obtain the projection such that $Size_{proj} = cos(\theta + 90) * Size$ where θ is the Disk Angle in the East of North convention, extracted from the B19 catalog and 90 accounts for the conversion in the horizontal convention i.e. the dispersion axis. $Size$ is the Disk Length in arcsec. The assumed FWHM of the instrument (FWHM$_{inst}$) is obtained by subtracting in quadrature the FWHM measured from the FWHM of the incident spectra, which is the FWHM due to velocity dispersion (see section 4.3.2). To avoid confusion from blending and considering the amount of detected emission lines from the simulated spectra, we evaluate the spectral resolution on the [OIII]$\lambda 5008$ line which is, unlike Hα-[NII], not blended in the simulations.

Following the normalization presented in Pasquali et al. (2006a), we present in figure 6.7 the comparison of the object radius along the dispersion axis in arcsec, with the line's FWHM$_{inst}$ normalized by the FWHM of a source with 0".5 diameter (FWHM$_0$)[5]. The

---

[5] FWHM$_0$=$\Delta\lambda$ with $R = \lambda/\Delta\lambda = 380$ for a 0".5 diameter source. and $\lambda = 5008(1 + z)$.

resolution R and the pixel scale have been taken from Racca et al. (2016) and Gillard (2020). We can see, as expected, that the grism spectral dispersion degrades as the object size increases. A more significant distribution fed by additional sources is expected from the completion of the PILOT RUN.

6.5 Stacking analysis of the simulated spectra

Stacking spectra has been shown to be an effective method, binning in redshift, stellar mass, SFR and color excess, to perform statistical detections at high redshift (Delhaize, Meyer, and Boyle, 2013; Rodighiero et al., 2014).

We present here the stacking analysis that has been performed around the doublet [OIII]$\lambda\lambda$5008,4959, selecting [OIII]λ5008 bright emitters located at a redshift 1.6$\leq$z$\leq$2.0 and with a total Mass 9.43$\leq M_\star \leq$10.13. We finally obtain 9 sources whose parameters are indicated in table 6.2. We notice that all these galaxies present a flux for [OIII]λ4959 below the NISP-S detection limit (i.e. F([OIII]λ4959)=F([OIII]λ5008/2.98) $< 2 \times 10^{-16}$ erg s^{-1} cm^{-2}) with a mean [OIII]λ4959 line flux of the incident (input) spectra of 0.9×10^{-16} erg s^{-1} cm^{-2} (see table 6.2).

In order to stack the spectra of the different sources, we transform the spectra from the observed frame to the rest-frame, resampling each rest-frame spectra on a common wavelength array with a linear dispersion of 5.2Å/px. This corresponds to the rest-frame linear dispersion of the galaxy at the lowest redshift (i.e. z_{min}=1.60), and so with the "worst spectral sampling" among the nine stacked objects, obtained by the observed-to-rest-frame conversion of the linear dispersion of the simulated spectra (i.e., 13.4 [Å]/(1+z)).

The flux and wavelengths are converted with the same procedure described in section 4.1 where we transformed the spectra from rest-frame to observed frame.

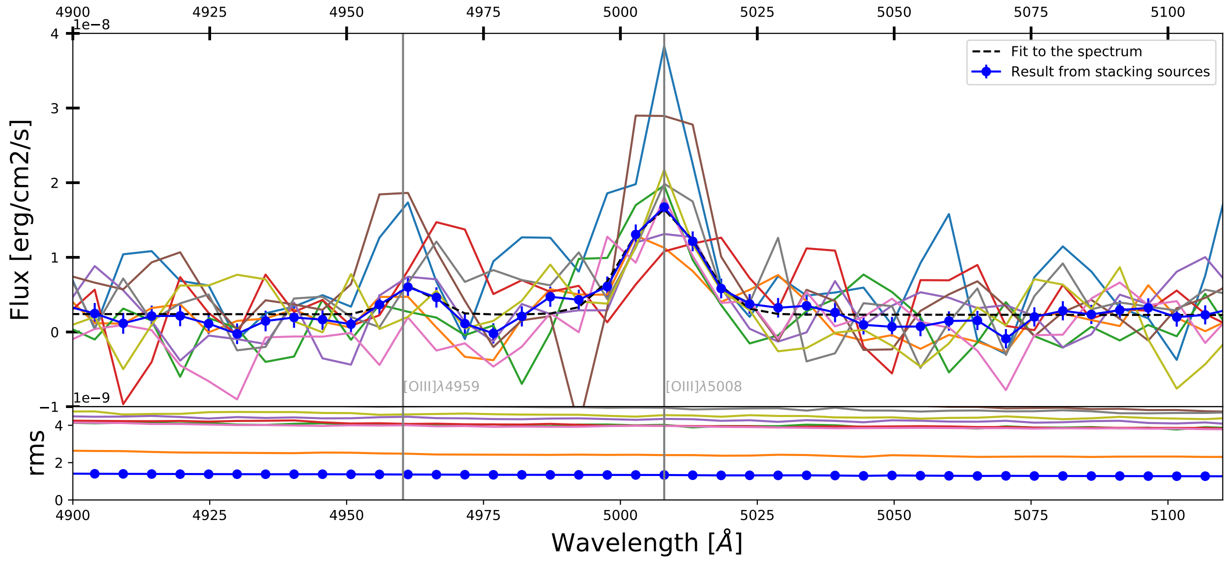

Figure 6.8 Top: Result from stacking 9 sources being [OIII]$\lambda 5008$ bright emitters and extracted from the B19 catalog. The sources have been selected such that 9.4 $\leq M_{\star} \leq$ 10.2 and 1.6 $\leq z \leq$ 2.0. We can detect from this stacking the two lines of the doublet [OIII]$\lambda\lambda$5008,4959 with SNR$_{\lambda 5008}$ $=$ 22.5 and SNR$_{\lambda 4959}$ $=$ 4.2. The SNR scales as $\sqrt{\text{amount of sources}}$, enabling to obtain a noise comparable to a source observed in 9 exposures of 4-dithered frames each (i.e. 36 frames). The [OIII]λ4959 fluxes for each of the co-added spectra are under the NISP detection limit such that this emission line shouldn't be detected in the Wide field configuration. Stacking therefore provides a great potential in increasing the detection capability without increasing the exposure time. Bottom: The rms spectrum for all the co-added spectra are plotted in multicolors and the blue line represents the rms spectrum obtained from stacking.

The stacking is performed with a similar procedure (taking the weighted mean of the fluxes) as that used to combine 1D spectra from the 4-dithered frames (see section 6.2). We assume a Gaussian behaviour for the Noise, such that stacking spectra makes the noise to decrease with the square root of the number of co-added spectra, resulting in a $\sqrt{9}$ times reduction in noise compared to the single Wide field exposure.

The SNRs measured for the two detected lines (see figure 6.8) are $\mathrm{SNR}_{\lambda 5008} = 22.5$ and $\mathrm{SNR}_{\lambda 4959} = 4.2$ such that stacking spectra obtained from Wide field exposures enables to detect the [OIII]λ4959 emission line while it was under the NISP-S capabilities in the Wide field configuration. The stacking performed as expected, improving the SNR by a factor of about $\sqrt{9}$. Indeed we can see on figure 6.8 that the rms goes from ≈ 4.3 to ≈ 1.5. Stacking therefore provides a great potential to obtain complementary information, such as confirming redshift determination, a crucial aspect to fulfill Euclid requirements for the cosmological probes and in particular for the Galaxy Clustering probe (see section 2.2.2).

ID BARRO2019	z	$\log(M_{star}/M_{\odot})$	$\log(\mathrm{SFR}/(M_{\odot}yr^{-1}))$	Av	Incident flux [OIII]λ5008	Incident H(AB)
2089	1.97	10.0	2.19	0.9	3.6×10^{-16}	21.7
2259	1.60	9.69	1.61	0.6	3.8×10^{-16}	22.1
9475	1.91	9.43	1.49	0.4	4.3×10^{-16}	22.8
11751	1.88	10.13	1.54	0.7	1.6×10^{-16}	22.2
15158	1.97	9.99	1.25	0.6	1.5×10^{-16}	22.8
17718	1.78	9.7	2.17	0.9	4.7×10^{-16}	21.8
19085	1.92	9.99	1.05	0.6	1.4×10^{-16}	23.2
20057	1.67	10.07	1.74	1.1	1.3×10^{-16}	22.1
21410	1.98	9.77	1.4	0.6	1.2×10^{-16}	22.9

Table 6.2 Parameters of the co-added spectra selected for stacking. We can see that considering the mean Incident flux of the [OIII]λ5008 line (indicated in CGS in the table) the line [OIII]λ4959 would not be detected according to the expected Euclid NISP detection limit with a mean flux of $2.6 \times 10^{-16}/2.98 = 0.9 < 2 \times 10^{-16}$ *CGS. However, after stacking spectra this line can be detected, illustrating the potential of the approach in increasing the sensitivity.*

Chapter Seven

Conclusion

We have presented in this Thesis the construction of spectral libraries using publicly released photometric and spectroscopic data from the COSMOS and CANDELS/GOODS-N fields. We have created two libraries aiming at providing a realistic sample of sources to be simulated by the NISP-S simulator. One library has been created to perform analysis on the Euclid Wide field configuration, while the other has been prepared to simulate the Euclid Deep field configuration.

We have separately generated the continuum, using the Software GALAXEV, and calculated nebular emission line fluxes using calibrations made from observations and photoionization models. We have calibrated our calculated fluxes with observation referring to publicly released spectroscopic data.

The two libraries have been constructed as part of the PILOT RUN that aims at providing confirmations of the NISP-S capabilities in terms of detection limit of nebular emission lines.

The PILOT RUN simulations are still ongoing. To date only part of the simulated spectra have been constructed, limited to the galaxies from the CANDELS/GOODS-N catalog, corresponding to one out of the 5 pointings required for the Deep Survey configuration. However, this pointing exactly matches the exposure time required for the Wide Survey configuration. Thus, we have presented in this Thesis a first analysis of the available simulated data, and provide a confirmation of the detection limit specifications for the continuum (i.e.

H(AB) $\leq$ 19.5 mag) and emission lines (i.e. Flux $\geq 2 \times 10^{-16}$ erg cm^{-2} s^{-1} Å^{-1}) of the Euclid Wide Survey. We have derived promising results regarding the fulfilment of the detection limit requirements for both the continuum and emission lines that are reached and even overcame in this analysis.

Beyond these positive results on the detection limits inferred in this Thesis, the almost perfect agreement between simulated and incident fluxes for values $\geq 3 \times 10^{-16}$ erg cm^{-2} s^{-1} Å^{-1} is also a powerful indicator to validate the performance of the simulator, and of the reduction pipeline, including the 1D spectra extraction and the calibration processes.

In the near future, a confirmation will be provided by completing the PILOT RUN that will extensively complete this preliminary picture with larger samples.

We have also shown an estimation of the variation of the spectral resolution as a function of the size of the galaxy projected on the dispersion axis, which should be taken into to account when dealing with slitless spectroscopy.

We eventually presented a first stacking analysis on a wavelength range around the doublet [OIII]$\lambda\lambda 4959, 5008$, that led to the detection of the [OIII]$\lambda 4959$ lines with a SNR = 4.2. This is a very positive result since [OIII]$\lambda 4959$ was under the NISP detection capabilities on every co-added spectra. This result gives a first idea of the great potential of the stacking analysis in confirming the redshift determination, a crucial aspect for the scope of the Euclid mission. Further stacking analysis will be performed for different redshift bins and different nebular emission lines by completing the PILOT RUN.

To complete the PILOT RUN, further simulations will be realized on these two incident spectral libraries. In particular, the simulations will be performed in the Deep field configuration for the library created from the GOODS-N/BARRO2019 catalog as well as in the Wide field configuration for the library created from the COSMOS2015 catalog.

By validating the expected spectroscopic detection limits of the NISP as well as validating the simulator pipeline, this Thesis highlights a great success for the Euclid Consortium.

REFERENCES

Abazajian, Kevork N et al. (2009). “The seventh data release of the sloan digital sky survey ”. In: The Astrophysical Journal 182, pp. 543–558. arXiv: arXiv:0812.0649v2.

Acker, A. et al. (Dec. 1989). “On the theoretical ratio of some nebular lines.” In: The Messenger 58, pp. 44–46.

Albrecht, Andreas et al. (2009). Findings of the Joint Dark Energy Mission Figure of Merit Science Working Group. arXiv: 0901.0721 `[astro-ph.IM]`.

Arnouts, S. and O. Ilbert (2011). LePHARE: Photometric Analysis for Redshift Estimate. ascl: 1108.009.

Arnouts, S. et al. (Jan. 2002). “Measuring the redshift evolution of clustering: the Hubble Deep Field South”. In: Monthly Notices of the Royal Astronomical Society 329.2, pp. 355–366. issn: 0035-8711. doi: 10.1046/j.1365-8711.2002.04988.x. eprint: https://academic.oup.com/mnras/article-pdf/329/2/355/18644861/329-2-355.pdf.

Asplund, M. et al. (Mar. 2004). “Line formation in solar granulation”. In: Astronomy and Astrophysics 417.2, pp. 751–768. issn: 1432-0746. doi: 10.1051/0004-6361:20034328.

Baldwin, A., M. M. Phillips, and R. Terlevich (1981). “Erratum - Classification Parameters for the Emission-Line Spectra of Extragalactic Objects”. In: Publications of the Astronomical Society of the Pacific 93.February, p. 817. issn: 0004-6280. doi: 10.1086/130930.

Barro, Guillermo et al. (2019). “The CANDELS/SHARDS Multiwavelength Catalog in GOODS-N: Photometry, Photometric Redshifts, Stellar Masses, Emission-line Fluxes, and Star Formation Rates”. In: The Astrophysical Journal Supplement Series 243.2, p. 22. issn: 1538-4365. doi: 10.3847/1538-4365/ab23f2. arXiv: 1908.00569.

Bernardis, P. de et al. (Apr. 2000). “A flat Universe from high-resolution maps of the cosmic microwave background radiation”. In: Nature 404.6781, pp. 955–959. issn: 1476-4687. doi: 10.1038/35010035.

Bezanson, Rachel et al. (2018). “ 1D Kinematics from Stars and Ionized Gas at z 0.8 from the LEGA-C Spectroscopic Survey of Massive Galaxies ”. In: The Astrophysical Journal 868.2, p. L36. issn: 2041-8213. doi: 10.3847/2041-8213/aaf16b. eprint: arXiv: 1811.07900v1.

Brammer, Gabriel B. et al. (2012). “3D-HST: A wide-field grism spectroscopic survey with the hubble space telescope”. In: Astrophysical Journal, Supplement Series 200.2. issn: 00670049. doi: 10.1088/0067-0049/200/2/13. arXiv: 1204.2829.

Bruzual, G. and S. Charlot (Oct. 2003). “Stellar population synthesis at the resolution of 2003”. In: Monthly Notices of the Royal Astronomical Society 344.4, pp. 1000–1028. issn: 0035-8711. doi: 10.1046/j.1365-8711.2003.06897.x. eprint: https://academic.oup.com/mnras/article-pdf/344/4/1000/2908334/344-4-1000.pdf.

Calzetti, Daniela and Anne L. Kinney (1994). “Dust extinction of the stellar continua in starburst galaxies: The ultraviolet and optical extinction law”. In: The Astrophysical Journal 429, pp. 582–601.

Calzetti, Daniela et al. (2000). “The Dust Content and Opacity of Actively Star-forming Galaxies”. In: The Astrophysical Journal 533.2, pp. 682–695. issn: 0004-637X. doi: 10.1086/308692. arXiv: 9911459.

Cappellari, Michele (2017). “Improving the full spectrum fitting method: Accurate convolution with Gauss-Hermite functions”. In: Monthly Notices of the Royal Astronomical Society 466.1, pp. 798–811. issn: 13652966. doi: 10.1093/mnras/stw3020. arXiv: 1607.08538.

Chabrier, Gilles (2003). “Galactic Stellar and Substellar Initial Mass Function”. In: Publications of the Astronomical Society of the Pacific 115.809, pp. 763–795. issn: 0004-6280. doi: 10.1086/376392. arXiv: 0304382.

Daddi, E. et al. (2004). “ A New Photometric Technique for the Joint Selection of Star-forming and Passive Galaxies at 1.4 z 2.5 ”. In: The Astrophysical Journal 617.2, pp. 746–764. issn: 0004-637X. doi: 10.1086/425569. arXiv: 0409041v1.

Daddi, E et al. (2007). “Multiwavelength Study of Massive Galaxies at z≈2.1. Star Formation and Galaxy Growth”. In: The Astrophysical Journal 670.1, pp. 156–172. issn: 0004-637X. doi: 10.1086/521818. eprint: arXiv:0705.2831v2.

Delhaize, J, M J Meyer, and B J Boyle (2013). “Detection of H I in distant galaxies using spectral stacking 1 I N T RO D U C T I O N”. In: Royal astronomical society 1410.2013, pp. 1398–1410. doi: 10.1093/mnras/stt810.

Denicolo, Glenda, Roberto Terlevich, and Elena Terlevich (2002). “New light on the search for low-metallicity galaxies – I . The N2 calibrator”. In: the Royal Astronomical Society 330, pp. 69–74.

Dimauro, Paola et al. (May 2018). “A catalog of polychromatic bulge-disc decompositions of 17.600 galaxies in CANDELS”. In: Monthly Notices of the Royal Astronomical Society 478.4, pp. 5410–5426. issn: 1365-2966. doi: 10.1093/mnras/sty1379.

Dimitrijević, M. S. et al. (Dec. 2006). “The flux ratio of the [O iii] λλ5007, 4959 lines in AGN: comparison with theoretical calculations”. In: Monthly Notices of the Royal Astronomical Society 374.3, pp. 1181–1184. issn: 0035-8711. doi: 10.1111/j.1365-2966.2006.11238.x. eprint: https://academic.oup.com/mnras/article-pdf/374/3/1181/3549555/mnras0374-1181.pdf.

Donas, J and J.M Deharveng (1984). “Ultraviolet luminosities and colors of spiral and irregular galaxies. The present-day star formation rate.” In: Astronomy and Astrophysics 140.325-333.

Dopita, Michael A. et al. (2016). “Chemical abundances in high-redshift galaxies: A powerful new emission line diagnostic”. In: Astrophysics and Space Science, p. 4. doi: 10.1007/s10509-016-2657-8. arXiv: 1601.01337.

Einsenstein, Daniel J. et al. (2005). “Detection of the baryon acoustic peak in the large-scale correlation function of sdss luminous red galaxies”. In: Astrophysical Journal 633, pp. 560–574. eprint: 0501171v1.

Erb, Dawn K. et al. (June 2006). “The Mass-Metallicity Relation atz2”. In: The Astrophysical Journal 644.2, pp. 813–828. issn: 1538-4357. doi: 10.1086/503623.

Fõrster Schreiber, N. et al. (2009). “The sins survey: sinfoni integral field spectroscopy of z 2 star-forming galaxies 1”. In: The Astrophysical Journal. arXiv: arXiv:0903.1872v2.

Fõrster Schreiber, N. et al. (Oct. 2018). “The SINS/zC-SINF Survey of z 2 Galaxy Kinematics: SINFONI Adaptive Optics–assisted Data and Kiloparsec-scale Emission-line Properties”. In: The Astrophysical Journal Supplement Series 238.2, p. 21. issn: 1538-4365. doi: 10.3847/1538-4365/aadd49.

Freudling, W. et al. (2008). “The Hubble Legacy Archive NICMOS grism data”. In: Astronomy Astrophysics 490.3, pp. 1165–1179. issn: 1432-0746. doi: 10.1051/0004-6361:200810282.

Garilli, B. et al. (2010). “EZ : A Tool For Automatic Redshift Measurement”. In: The Astronomical Society of the Paciic 122, pp. 827–838.

Gillard, W (2020). “Status of NISP ground testing”. In: Euclid Annual conference.

Grieb, Jan Niklas et al. (Jan. 2017). “The clustering of galaxies in the completed SDSS-III Baryon Oscillation Spectroscopic Survey: Cosmological implications of the Fourier space wedges of the final sample”. In: Monthly Notices of the Royal Astronomical Society, stw3384. issn: 1365-2966. doi: 10.1093/mnras/stw3384.

Grogin, Norman A. et al. (2011). “Candels: The Cosmic Assembly Near-infrared Deep Extragalactic Legacy Survey”. In: The Astrophysical Journal, Supplement Series 197.2. issn: 00670049. doi: 10.1088/0067-0049/197/2/35. arXiv: 1105.3753.

Haussel, Hervé (2020). “RGS270 Update”. In: Euclid Annual conference.

Henry, R. B. C., M. G. Edmunds, and J. Koppen (2001). “On the Cosmic Origins of Carbon and Nitrogen”. In: Astrophysics and Space Science 277, pp. 169–172.

Hinshaw, G et al. (2003). “First Year Wilkinson Microwave Anisotropy Probe (WMAP 1) Observations: The Angular Power Spectrum”. In: Astrophysical Journal, pp. 1–44. arXiv: 0302217v1.

Hogg, David W et al. (2002). “The K correction”. In: pp. 1–5. arXiv: 0210394v1.

Hummer, D. G. and P. J. Storey (Feb. 1987). “Recombination-line intensities for hydrogenic ions - I. Case B calculations for H I and He II”. In: Monthly Notices of the Royal Astronomical Society 224.3, pp. 801–820. issn: 0035-8711. doi: 10.1093/mnras/224.3.801.

Iani, E. et al. (2019). “Inquiring into the nature of the Abell 2667 brightest cluster galaxy: physical properties from MUSE”. In: Monthly Notices of the Royal Astronomical Society 487.4, pp. 5593–5609. issn: 13652966. doi: 10.1093/mnras/stz1631. arXiv: 1906.04744.

Kartaltepe, Jeyhan S. et al. (June 2015). “Rest-frame Optical Emission Lines in Far-infrared-selected Galaxies at $z < 1.7$ from the FMOS-COSMOS Survey”. In: Astrophysical Journal Letters 806.2, L35, p. L35. doi: 10.1088/2041-8205/806/2/L35. arXiv: 1505.03527.

Kashino, D. et al. (2013). “The fmos-cosmos survey of star-forming galaxies at z 1.6. I. Hα-based star formation rates and dust extinction”. In: Astrophysical Journal Letters 777.1, pp. 4–10. issn: 20418205. doi: 10.1088/2041-8205/777/1/L8.

Kashino, D. et al. (2017). “The FMOS-COSMOS Survey of Star-forming Galaxies at $z \approx 1.6$. IV. Excitation State and Chemical Enrichment of the Interstellar Medium”. In: The Astrophysical Journal Letters 835.1, 88, p. 88. doi: 10.3847/1538-4357/835/1/88. arXiv: 1604.06802.

Kashino, Daichi and Akio K. Inoue (2018). “Disentangling the physical parameters of gaseous nebulae and galaxies”. In: Monthly Notices of the Royal Astronomical Society 486.1, pp. 1053–1069. issn: 13652966. doi: 10.1093/mnras/stz881. arXiv: 1812.06939.

Kashino, Daichi et al. (2019). “ The FMOS-COSMOS Survey of Star-forming Galaxies at z 1.6. VI. Redshift and Emission-line Catalog and Basic Properties of Star-forming Galaxies ”. In: The Astrophysical Journal Supplement Series 241.1, p. 10. issn: 0067-0049. doi: 10.3847/1538-4365/ab06c4.

Kennicut, Robert C. Jr., Peter Tamblyn, and Charles W. Congdon (1994). “Past and future star formation in disk galaxies”. In: Astrophysical Journal 435, pp. 22–36. doi: 10.1086/174790.

Kennicutt, Robert C. (1998). “Star Formation in Galaxies Along the Hubble Sequence”. In: Annual Review of Astronomy and Astrophysics 36.1, pp. 189–231. issn: 0066-4146. doi: 10.1146/annurev.astro.36.1.189. arXiv: 9807187.

Kewley, L J et al. (2001). “Theoretical Modeling of Starburst Galaxies”. In: The Astrophysical Journal 556.1, pp. 1–36. arXiv: 0106324v1.

Kewley, L. J. and M. A. Dopita (Sept. 2002). “Using Strong Lines to Estimate Abundances in Extragalactic H ii Regions and Starburst Galaxies”. In: The Astrophysical Journal Supplement Series 142.1, pp. 35–52. issn: 1538-4365. doi: 10.1086/341326.

Kewley, Lisa J. and Sara L. Ellison (2008). “Metallicity Calibrations and the Mass-Metallicity Relation for Star-forming Galaxies”. In: The Astrophysical Journal 681.2, pp. 1183–1204. issn: 0004-637X. doi: 10.1086/587500. arXiv: 0801.1849.

Kewley, Lisa J., Margaret J. Geller, and Rolf A. Jansen (2004). “ [O ii] as a Star Formation Rate Indicator ”. In: The Astronomical Journal 127.4, pp. 2002–2030. issn: 0004-6256. doi: 10.1086/382723. arXiv: 0401172v1.

Kewley, Lisa J., David C. Nicholls, and Ralph S. Sutherland (2019). “Understanding Galaxy Evolution Through Emission Lines”. In: Annual Review of Astronomy and Astrophysics 57.1, pp. 511–570. issn: 0066-4146. doi: 10.1146/annurev-astro-081817-051832. arXiv: 1910.09730.

Kewley, Lisa J. et al. (2006). “The host galaxies and classification of active galactic nuclei”. In: Monthly Notices of the Royal Astronomical Society 372.3, pp. 961–976. issn: 00358711. doi: 10.1111/j.1365-2966.2006.10859.x. arXiv: 0605681.

Kewley, Lisa J. et al. (2013a). “THE cosmic BPT diagram: Confronting theory with observations”. In: Astrophysical Journal Letters 774.1, pp. 6–11. issn: 20418205. doi: 10.1088/2041-8205/774/1/L10. arXiv: 1307.0514.

Kewley, Lisa J. et al. (2013b). “Theoretical evolution of optical strong lines across cosmic time”. In: Astrophysical Journal 774.2. issn: 15384357. doi: 10.1088/0004-637X/774/2/100. arXiv: 1307.0508.

Kimura, Masahiko et al. (Oct. 2010). “Fibre Multi-Object Spectrograph (FMOS) for the Subaru Telescope”. In: Publications of the Astronomical Society of Japan 62.5, pp. 1135–1147. issn: 0004-6264. doi: 10.1093/pasj/62.5.1135. eprint: https://academic.oup.com/pasj/article-pdf/62/5/1135/9715472/pasj62-1135.pdf.

Koekemoer, Anton M. et al. (2011). “Candels: The cosmic assembly near-infrared deep extragalactic legacy survey - The hubble space telescope observations, imaging data products, and mosaics”. In: Astrophysical Journal, Supplement Series 197.2. issn: 00670049. doi: 10.1088/0067-0049/197/2/36. arXiv: arXiv:1105.3754v2.

Kümmel, M. et al. (Jan. 2009). “The Slitless Spectroscopy Data Extraction Software aXe”. In: Publications of the Astronomical Society of the Pacific 121.875, pp. 59–72. issn: 1538-3873. doi: 10.1086/596715.

Laigle, C. et al. (June 2016). “The COSMOS2015 catalog: exploring the $1<z<6$ Universe with half a million galaxies”. In: The Astrophysical Journal Supplement Series 224.2, p. 24. issn: 1538-4365. doi: 10.3847/0067-0049/224/2/24.

Larson, Richard B. and Beatrice M. Tinsley (1977). “Star formation rates in normal and peculiar galaxies”. In: The Astrophysical Journal 219, pp. 46–59.

Laureijs, R. et al. (2009). Euclid Assessment Study Report for the ESA Cosmic Visions. arXiv: 0912.0914.

Le Fèvre, Oliver et al. (2015). “The VIMOS Ultra-Deep Survey : 10 000 galaxies with spectroscopic redshifts to study galaxy assembly at early epochs $2 < z$ approx 6 ”. In: Astronomy and Astrophysics. doi: 10.1051/0004-6361/201423829.

Le Fèvre, Olivier et al. (2003). “Commissioning and performances of the VLT-VIMOS”. In: Instrument Design and Performance for Optical/Infrared Ground-based Telescopes. Ed. by Masanori Iye and Alan F. M. Moorwood. Vol. 4841. International Society for Optics and Photonics. SPIE, pp. 1670–1681. doi: 10.1117/12.460959.

LeBorgne, J.-F. et al. (2003). “STELIB : a library of stellar spectra at R 2000”. In: Astronomy and Astrophysics. arXiv: 0302334v1.

Levesque, Emily M., Lisa J. Kewley, and Kirsten L. Larson (Jan. 2010). “Theoretical Modeling of Star-Forming Galaxies I. Emission Line Diagnostic Grids for Local and Low-Metallicity Galaxies”. In: The Astronomical Journal 139.2, pp. 712–727. issn: 1538-3881. doi: 10.1088/0004-6256/139/2/712.

Maciaszek, Thierry et al. (2016). “Euclid Near Infrared Spectrometer and Photometer instrument concept and first test results obtained for different breadboards models at the end of phase C”. In: Space Telescopes and Instrumentation 2016: Optical, Infrared, and Millimeter Wave. Ed. by Howard A. MacEwen et al. Vol. 9904. International Society for Optics and Photonics. SPIE, pp. 298–315. doi: 10.1117/12.2232941.

Madau, Piero and Mark Dickinson (2014). “Cosmic Star-Formation History”. In: Annual Review of Astronomy and Astrophysics 52.1, pp. 415–486. issn: 1545-4282. doi: 10.1146/annurev-astro-081811-125615.

Madau, Piero, Lucia Pozzetti, and Mark Dickinson (May 1998). “The Star Formation History of Field Galaxies”. In: The Astrophysical Journal 498.1, pp. 106–116. issn: 1538-4357. doi: 10.1086/305523.

Maiolino, R. et al. (2008). “AMAZE: I. The evolution of the mass-metallicity relation at $z > 3$”. In: Astronomy and Astrophysics 488.2, pp. 463–479. issn: 00046361. doi: 10.1051/0004-6361:200809678. arXiv: 0806.2410.

Momcheva, Ivelina G. et al. (2015). “The 3D-HST Survey: Hubble Space Telescope WFC3/G141 grism spectra, redshifts, and emission line measurements for $\sim 100,000$ galaxies”. In: The

Astrophysical Journal Supplement Series 225.2, p. 27. issn: 1538-4365. doi: 10.3847/0067-0049/225/2/27.

Moresco, Michele (2020). “Euclid: a space mission to study the origin of the accelerating Universe”. In: Euclid Annual conference.

Morisset, C. et al. (2016). “Photoionization models of the CALIFA H II regions: I. Hybrid models”. In: Astronomy and Astrophysics 594.1987. issn: 14320746. doi: 10.1051/0004-6361/201628559. arXiv: 1606.01146.

Morton, Donald C. (2000). “Atomic Data for Resonance Absorption Lines. II. Wavelengths Longward of the Lyman Limit for Heavy Elements”. In: The Astrophysical Journal Supplement Series 130.2, pp. 403–436. doi: 10.1086/317349.

Moustakas, John, Robert C. Kennicutt Jr., and Christy A. Tremonti (May 2006). “Optical Star Formation Rate Indicators”. In: The Astrophysical Journal 642.2, pp. 775–796. issn: 1538-4357. doi: 10.1086/500964.

Noeske, K. G. et al. (2007). “ Star Formation in AEGIS Field Galaxies since z = 1.1: The Dominance of Gradually Declining Star Formation, and the Main Sequence of Star-forming Galaxies ”. In: The Astrophysical Journal 660.1, pp. L43–L46. issn: 0004-637X. doi: 10.1086/517926. arXiv: 0701924.

Osterbrock, Donald E. (1989). “Astrophysics of gaseous nebulae and active galactic nuclei”. In: University Science Books, 408pp. doi: ISBN0-935702-22-9.

Osterbrock, Donald E. and Gary J. Ferland (2006). Astrophysics of gaseous nebulae and active galactic nuclei, (CA: Sausalito: University Science Books).

Osterbrock, Donald E. and Richard W. Podge (1985). “The spectra of narrow-line Seyfert 1 galaxies”. In: Astrophysical Journal 297.1010, pp. 166–176.

Pasquali, A. et al. (2006a). “Slitless Grism Spectroscopy with theHubble Space TelescopeAdvanced Camera for Surveys”. In: Publications of the Astronomical Society of the Pacific 118.840, pp. 270–287. issn: 1538-3873. doi: 10.1086/498731.

Pasquali, A et al. (2006b). “Slitless Grism Spectroscopy with the Hubble Space Telescope Advanced Camera”. In: The Astronomical Society of the Paciic 118, pp. 270–287.

Peng, Chien Y et al. (2010). “Detailed decomposition of galaxy images. ii. beyond axisymmetric models”. In: The Astronomical Journal. arXiv: arXiv:0912.0731v2.

Pettini, Max and Bernard E.J. Pagel (2004). “[O III]/[N II] as an abundance indicator at high redshift”. In: Monthly Notices of the Royal Astronomical Society 348.3, pp. 0–4. issn: 00358711. doi: 10.1111/j.1365-2966.2004.07591.x. arXiv: 0401128.

Proxauf, B, S Öttl, and S Kimeswenger (2014). "Upgrading electron temperature and electron density diagnostic diagrams of forbidden line emission (Research Note)". In: Astronomy and Astrophysics 10, pp. 1–4. doi: 10.1051/0004-6361/201322581.

Puglisi, A et al. (2016). "Astrophysics Dust attenuation in z 1 galaxies from Herschel and 3D-HST H α measurements". In: Astronomy and Astrophysics 83, pp. 1–17. doi: 10.1051/0004-6361/201526782.

Racca, Giuseppe D. et al. (2016). "The Euclid mission design". In: Space Telescopes and Instrumentation 2016: Optical, Infrared, and Millimeter Wave. Ed. by Howard A. MacEwen et al. doi: 10.1117/12.2230762.

Rieke, G.h. and M.J. Lobofsky (1979). "Infrared emission of extragalactic sources". In: Astronomy and Astrophysics 14, pp. 477–511.

Roberts, W. W. (1969). "Large-Scale Shock Formation in Spiral Galaxies and its Implications on Star Formation". In: The Astrophysical Journal 158, p. 123. doi: 10.1086/150177.

Rodighiero, G. et al. (2011). "The lesser role of starbursts for star formation at z= 2". In: The Astrophysical Journal 739.2, p. L40. doi: 10.1088/2041-8205/739/2/l40.

Rodighiero, G et al. (2014). "A multiwavelength consensus on the main sequence of star-forming galaxies at z ˜ 2". In: Monthly Notices of the Royal Astronomical Society 443.1, pp. 19–30. issn: 13652966. doi: 10.1093/mnras/stu1110. arXiv: arXiv:1406.1189v1.

Ryan, R E, S Casertano, and N Pirzkal (2018). "Linear : A Novel Algorithm for Reconstructing Slitless Spectroscopy from HST / WFC3". In: Publications of the Astronomical Society of the Pacific 130.985, p. 34501. issn: 1538-3873. doi: 10.1088/1538-3873/aaa53e.

Salpeter, Edwin E. (1955). "The Luminosity Function and Stellar Evolution." In: 121, p. 161. doi: 10.1086/145971.

Sánchez, Ariel G. et al. (2016). "The clustering of galaxies in the completed SDSS-III Baryon Oscillation Spectroscopic Survey: combining correlated Gaussian posterior distributions". In: Monthly Notices of the Royal Astronomical Society 464.2, pp. 1493–1501. issn: 1365-2966. doi: 10.1093/mnras/stw2495.

Sanders, Ryan L. et al. (2019). "The MOSDEF Survey: [S iii] as a New Probe of Evolving Interstellar Medium Conditions". In: The Astrophysical Journal 888.1, p. L11. doi: 10.3847/2041-8213/ab5d40. arXiv: arXiv:1910.13594v2.

Sargent, M. T. et al. (Aug. 2014). "Regularity underlying complexity: a redshift-independent description of the continuous variation of galaxy-scale molecular gas properties in the mass-star formation rate plane". In: The Astrophysical Journal 793.1, p. 19. issn: 1538-4357. doi: 10.1088/0004-637x/793/1/19.

Schneider, P., C. Kochanek, and J. Wambsganss (2006). Gravitational lensing: Strong, Weak and Micro. Ed. by Springer. Swiss Soiety for Astrophysics and Astronomy.

Scoville, N et al. (2007). "The Cosmic Evolution Survey (COSMOS): Overview 1". In: The Astrophysical Journal 172, pp. 1–8.

Silverman, J. D. et al. (2015). "The FMOS-COSMOS survey of star-forming galaxies at z 1.6. III. Survey design, performance, and sample characteristics". In: Astrophysical Journal, Supplement Series 220.1, p. 12. issn: 00670049. doi: 10.1088/0067-0049/220/1/12. arXiv: 1409.0447.

Steidel, Charles C. et al. (2014). "Strong Nebular Line Ratios in the Spectra of z 2-3 Star-forming Galaxies: First Results from KBSS-MOSFIRE". In: The Astrophysical Journal 795.2, p. 165. issn: 1538-4357. doi: 10.1088/0004-637x/795/2/165.

Tereno, Ismael (2020). "Euclid survey". In: Euclid Annual conference.

Tremonti, Christy A. et al. (2004). "The Origin of the Mass-Metallicity Relation: Insights from 53,000 Star-forming Galaxies in the Sloan Digital Sky Survey". In: The Astrophysical Journal 613.2, pp. 898–913. issn: 0004-637X. doi: 10.1086/423264. arXiv: 0405537v1.

Valentino, F. et al. (2017). "Predicting emission line fluxes and number counts of distant galaxies for cosmological surveys". In: Monthly Notices of the Royal Astronomical Society 472.4, pp. 4878–4899. issn: 13652966. doi: 10.1093/MNRAS/STX2305. arXiv: 1709.01936.

Van Der Wel, A. et al. (2012). "Structural parameters of galaxies in candels". In: Astrophysical Journal, Supplement Series 203.2. issn: 00670049. doi: 10.1088/0067-0049/203/2/24. arXiv: arXiv:1211.6954v2.

Van Der Wel, A. et al. (2014). "3D-HST+CANDELS: The evolution of the galaxy size-mass distribution since z = 3". In: Astrophysical Journal 788.1, p. 2014. issn: 15384357. doi: 10.1088/0004-637X/788/1/28.

Veilleux, S. and D.E. Osterbrock (1987). "Spectral classification of emission-line galaxies". In: The Astrophysical Journal Supplement Series 63, pp. 295–310.

Walsh, D., R. F. Carswell, and R. J. Weymann (1979). "0957 + 561 A, B: twin quasistellar objects or gravitational lens?" In: Nature 279, pp. 381–384. doi: 10.1038/279381a0.

Walsh, J. R., M. Kummel, and H. Kuntschner (2010). "Slitless Spectroscopy with HST Instruments". In: Space Telescope Science Insitute 3.2006, pp. 77–85.

Wel, A. van der et al. (2016). "The VLT Lega-C spectroscopic survey: the physics of galaxies at a lookback time of 7 Gyr". In: The Astrophysical Journal Supplement Series 223.2, p. 29. doi: 10.3847/0067-0049/223/2/29.

Williams, Rik J. et al. (2009). "Detection of quiescent galaxies in a bicolor sequence from Z = 0-2". In: Astrophysical Journal 691.2, pp. 1879–1895. issn: 15384357. doi: 10.1088/0004-637X/691/2/1879. arXiv: 0806.0625.

Williams, Robert E et al. (1996). “The Hubble deep field: observations, data reduction, and Galaxy photometry”. In: Astrophysical Journal 112.4, pp. 1335–1384.

Wuyts, Eva et al. (2014). “A consistent study of metallicity evolution at 0.8 < z < 2.6”. In: Astrophysical Journal Letters 789.2. issn: 20418213. doi: 10.1088/2041-8205/789/2/L40. arXiv: 1405.6590.

Wuyts, Stijn et al. (2011). “On star formation rates and star formation histories of galaxies out to z 3”. In: Astrophysical Journal 738.1, pp. 1–19. issn: 15384357. doi: 10.1088/0004-637X/738/1/106. arXiv: arXiv:1106.5502v1.

Zahid, H. Jabran et al. (2014). “The universal relation of galactic chemical evolution: The origin of the mass-metallicity relation”. In: Astrophysical Journal 791.2. issn: 15384357. doi: 10.1088/0004-637X/791/2/130. arXiv: 1404.7526.

APPENDIX

	Filter	λ_{Eff} [Å]
SHARDS filters	F500W17	5000.03
	F517W17	5170.18
	F534W17	5340.15
	F551W17	5510.04
	F568W17	5680.05
	F585W17	5849.79
	F602W17	6020.08
	F619W17	6190.00
	F636W17	6360.00
	F653W17	6530.09
	F670W17	6700.01
	F687W17	6870.02
	F704W17	7040.00
	F721W17	7210.05
	F738W17	7379.95
	F755W17	7550.05
	F772W17	7720.04
	F789W17	7890.03
	F806W17	8059.98
	F823W17	8230.00
	F840W17	8400.02
	F857W17	8569.98
	F883W35	8829.97
	F913W25	9130.03
	F941W33	9410.00
HST filters	ACS/F435W"	4363.25
	ACS/F606W	5961.14
	ACS/F775W	7705.95
	ACS/F814W	8083.67
	ACS/F850LP	9052.58
	WFC3/F105W	10584.74
	WFC3/F125W	12516.15
	WFC3/F140W	13968.64
	WFC3/F160W	15392.37
Euclid filters	VIS	7334.4
	Nisp/Y	10914.2
	Nisp/J	13785.1
	Nisp/H	17718.7

Table 1 The effective wavelengths of the the HST and SHARDS filters (Available on https://archive.stsci.edu/prepds/candels/. These filters and relative publicly released photometric data enable to evaluate the incident spectra created in this thesis. We also present the effective wavelengths of the Euclid filters (Available on http://euclid.esac.esa.int/epdb/db/SC3/. This data is used in this work to convert AB magnitude into flux and vice versa.

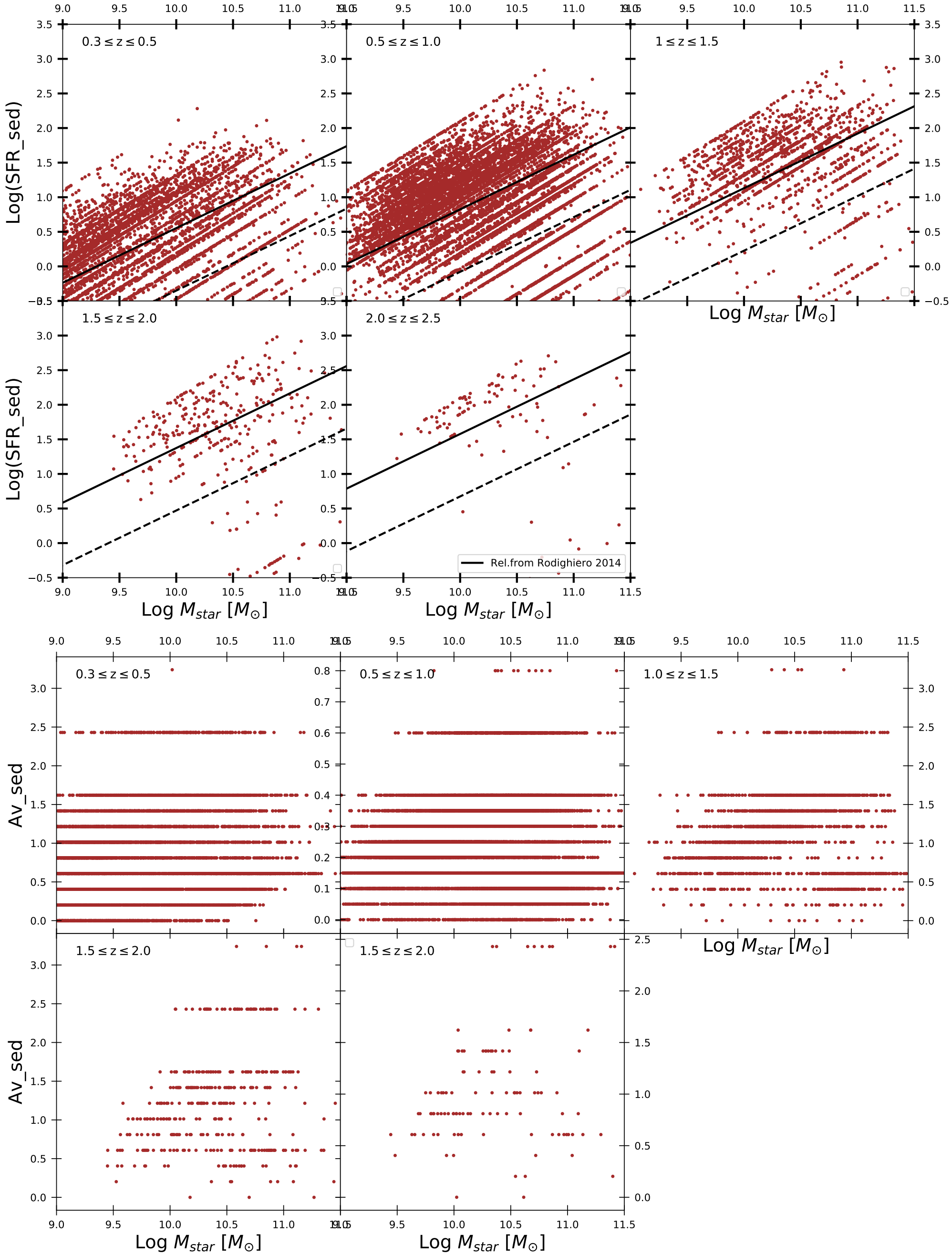

Figure 1 The main sequence (top) and absorption (bottom) as a function of mass. The black line is the normalization of the Main Sequence from Rodighiero et al. (2011) and the dashed line indicates a SFR 8x lower than the normalization, indicating potential Passive galaxies. The SFR(SED) indicated in this plot has been retrieved from SED-fitting. The sources belong to the L16 catalog.

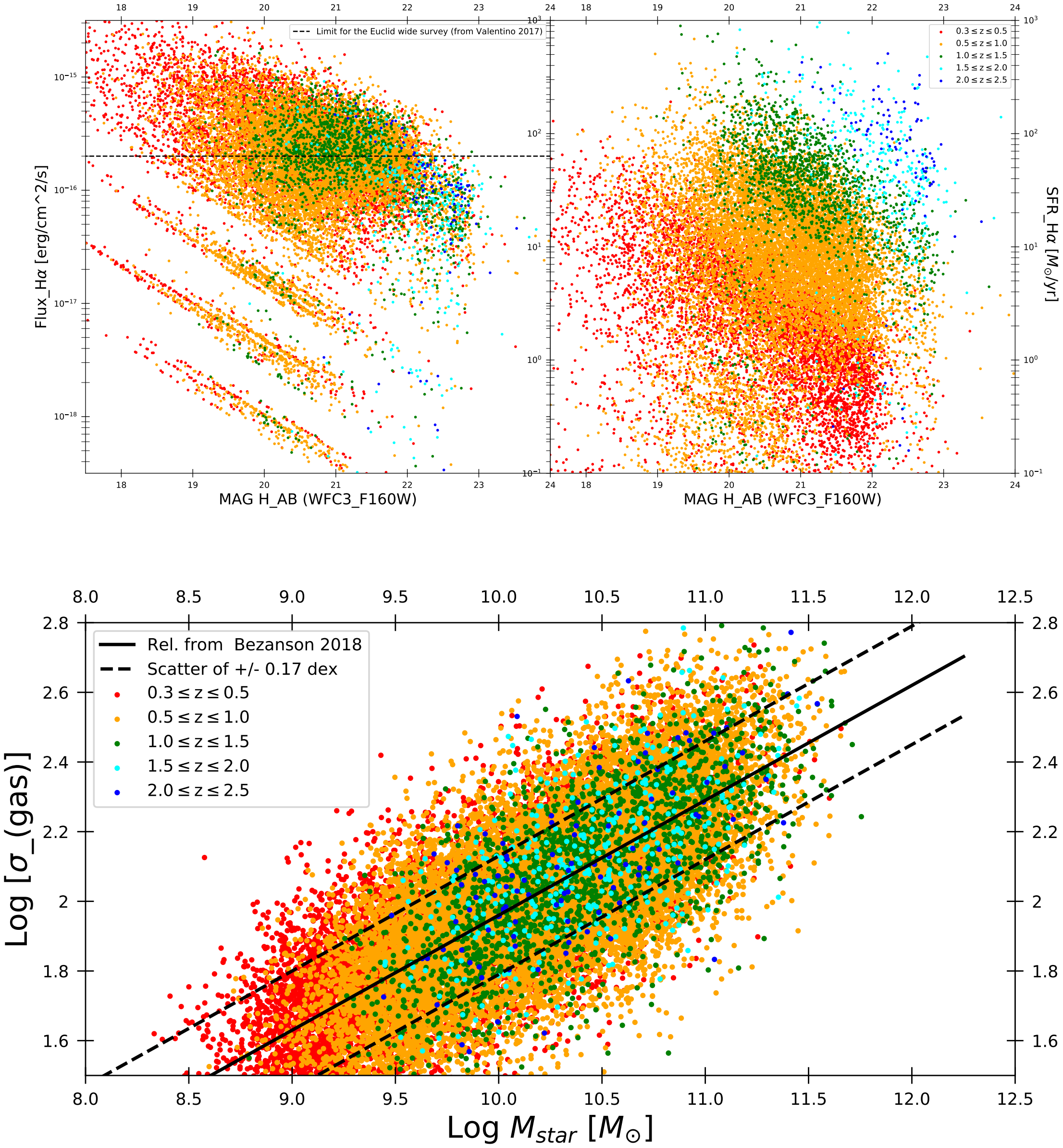

Figure 2 Top: The flux F(H_α) and the SFR(SED) as a function of the magnitude H in the AB system; The dashed line on the left represents the NISP-S detection limit for emission lines fluxes in the Euclid Wide field configuration (i.e. 2×10^{-16} in erg cm^{-2} s^{-1}). Bottom: The velocity dispersion calculated following the calibration presented in Bezanson et al. (2018). The sources belong to the L16 catalog.

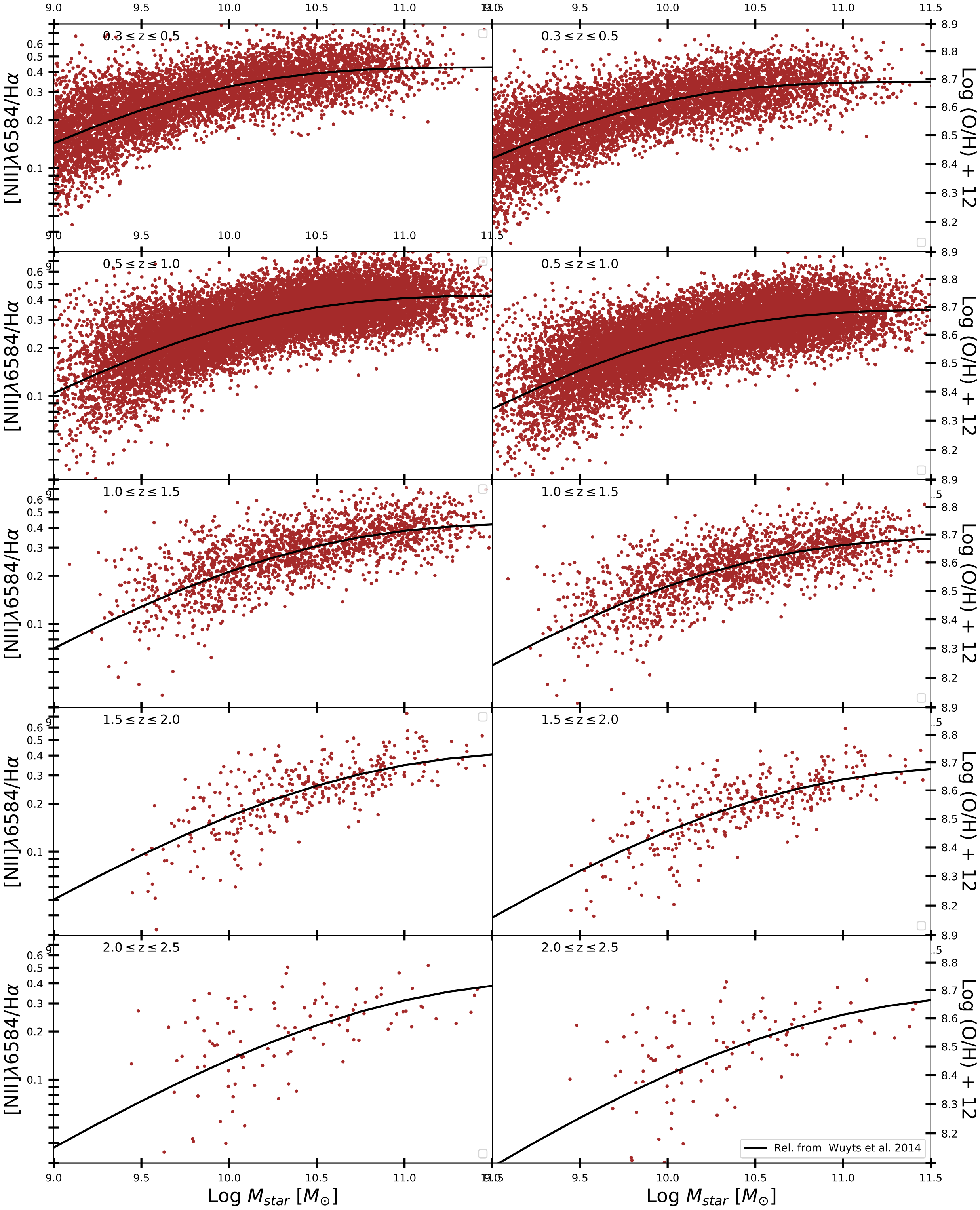

Figure 3 Calculated mass-metallicity relation for galaxies extracted from the L16 catalog following the calibrations provided by Wuyts et al. (2014) and adding a normally distributed scatter proposed by Kashino and Inoue (2018).

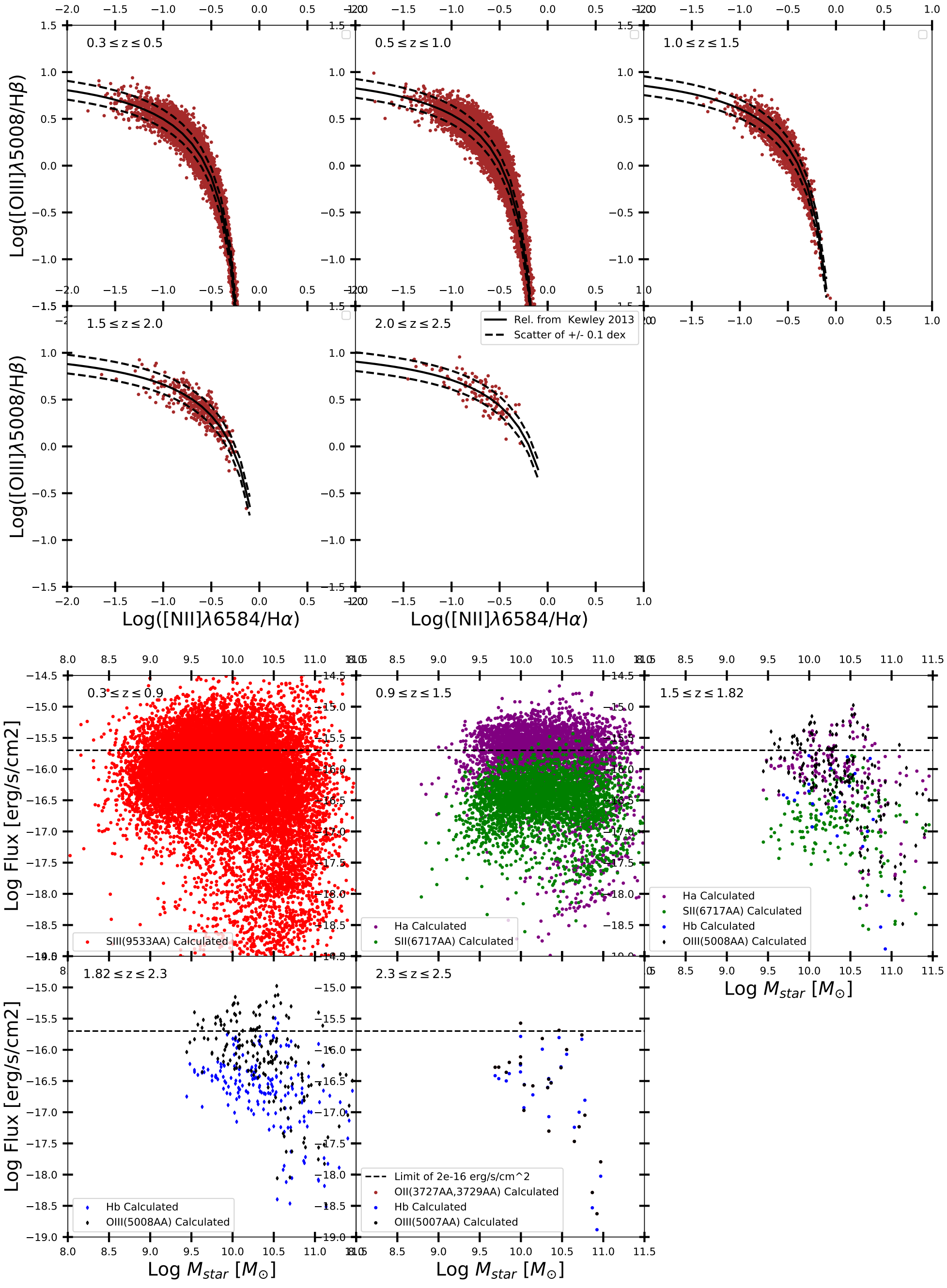

Figure 4 Top: The O_3-BPT diagram. The black line is the relation from Kewley et al. (2013b) with the scatter of 0.1 dex on the O_3 axis. Bottom: Emission lines' fluxes versus the total mass. The fluxes are indicated in their redshift window for observation through the NISP-S. For clarity, we only indicated the strongest lines in each redshift bins. The sources belong to the L16 catalog.

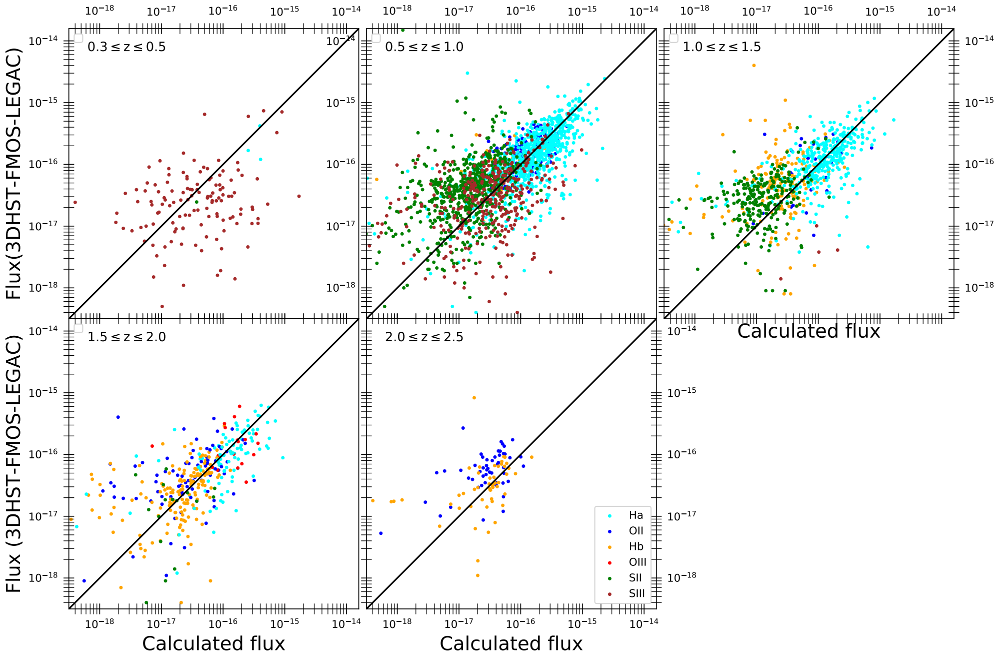

Figure 5 Comparison of our calculated fluxes for the Hα, Hβ, [NII]$\lambda\lambda$6584,6549, [OII]$\lambda\lambda$3727,3729, [OIII]$\lambda\lambda 4959, 5008$, [SII]$\lambda\lambda$6731,6717 and [SIII]$\lambda\lambda$9069,9531 lines with publicly released data from the near infrared spectroscopic survey with the HST (3D-HST), the Fiber Multi-Object Spectrograph (FMOS) and the Large Early Galaxy Astrophysics Census (LEGA-C) surveys. The Hα line fluxes retrieved from 3D-HST is blended with the [NII]$\lambda\lambda$6584,6549 lines. We therefore sum the corresponding calculated fluxes and is indicated by the Hα color code on the plot. The sources belong to the L16 catalog.